

# BULLETIN OF THE RESEARCH COUNCIL OF ISRAEL

## Section C TECHNOLOGY

*Bull. Res. Council of Israel. C. Techn.*

Incorporating the Scientific Publications of the  
Technion—Israel Institute of Technology, Haifa

THIRD ANNUAL CONFERENCE ON AVIATION AND ASTRONAUTICS  
FEBRUARY 21 AND 22, 1961

### Page

- 1 An analysis of the landing maneuver of winged aircraft *M. Arens*
- 11 Methods of flight testing abroad and in Israel *H. Marom*
- 29 The effect of nitromethane additions on the combustion of various  
fuels under spheroidal conditions *L. Gross-Gronomski*
- 39 Structure, variations and measurements of the earth's ionosphere and  
exosphere *C. Altman*
- 49 Buckling of thin circular conical shells subjected to axisymmetrical  
temperature distributions *J. Singer*
- 51 On the physical Riemann-Christoffel tensor in orthogonal  
coordinates *Z. Karni*
- 57 Hydrodynamical applications of a theorem on spherical means  
*E. Jabotinsky*
- 61 The mechanical properties and structure of some high tensile  
alloy steels *S. Becker and M. G. Bader*
- 79 Preliminary development of an annual jet injector  
*A. Kogan and M. Victor*
- 107 Aerodynamic research facilities at the Department of Aeronau-  
tical Engineering, Technion-Israel Institute of Technology *J. Rom*
- 119 An approximate method of solid propellant internal star grain  
calculation *A. Yaron and R. Corett*
- 120 On extragalactic cosmic rays *H. Kasha*
- 121 Strain gauge balance for wind tunnels  
*A. Kogan, J. Schwartz and A. Saginer*



Digitized by the Internet Archive  
in 2023

# **BULLETIN OF THE RESEARCH COUNCIL OF ISRAEL**

## **Section C TECHNOLOGY**

*Bull. Res. Coun. of Israel. C. Techn.*

Incorporating the Scientific Publications of the  
Technion — Israel Institute of Technology, Haifa



# BULLETIN OF THE RESEARCH COUNCIL OF ISRAEL

—  
MIRIAM BALABAN

Editor

## EDITORIAL BOARDS

### SECTION A CHEMISTRY

Y. AVIDOR  
E. D. BERGMANN  
M. R. BLOCH  
H. BERNSTEIN,  
E. KATCHALSKI  
A. KATZIR (KATCHALSKY)  
G. STEIN  
(Chairman,  
Israel Chemical Society)

### SECTION B ZOOLOGY

H. MENDELSON  
K. REICH  
L. SACHS  
A. YASHOUV

### SECTION C TECHNOLOGY

A. DANIEL  
J. BRAVERMAN  
A. DE LEEUW  
M. LEWIN  
M. REINER  
A. TALMI  
E. GOLDBERG, *Technion*  
Publications Language Editor

### SECTION D BOTANY

N. FEINBRUN  
N. LANDAU  
H. OPPENHEIMER  
T. RAYSS  
I. REICHERT  
M. ZOHARY

### SECTION E EXPERIMENTAL MEDICINE

S. ADLER  
A. DE VRIES  
A. FEIGENBAUM  
M. RACHMILEWITZ  
B. ZONDEK

### SECTION F MATHEMATICS AND PHYSICS

A. DVORETZKY  
J. GILLIS  
F. OLLENDORFF  
G. RACAH

### SECTION G GEO-SCIENCES

G. DESSAU  
J. NEUMANN  
L. PICARD

## NOTICE TO CONTRIBUTORS

Contributors to the *Bulletin of the Research Council of Israel* should conform to the following recommendations of the editors of this journal in preparing manuscripts for the press.

Contributions must be original and should not have been published previously. When a paper has been accepted for publication, the author(s) may not publish it elsewhere unless permission is received from the Editor of this journal.

Papers may be submitted in English and in French.

### MANUSCRIPT General

Papers should be written as concisely as possible. MSS should be typewritten on one side only and double-spaced, with side margins not less than 2.5 cm wide. Pages, including those containing illustrations, references or tables, should be numbered.

The Editor reserves the right to return a MS to the author for retyping or any alterations. Authors should retain copies of their MS.

### Spelling

Spelling should be based on the Oxford Dictionary and should be consistent throughout the paper. Geographic and proper names in particular should be checked for approved forms of spelling or transliteration.

### Indications

Greek letters should be indicated in a legend preceding the MS, as well as by a pencil note in the margin on first appearance in the text.

When there is any room for confusion of symbols, they should be carefully differentiated, e.g. the letter "I" and the figure "1"; "O" and "0".

### Abbreviations

Titles of journals should be abbreviated according to the *World List of Scientific Periodicals*.

### Abstract

Every paper must be accompanied by a brief but comprehensive abstract. Although the length of the abstract is left to the discretion of the author, 3% of the total length of the paper is suggested.

### References

In Sections A and C, and in Letters to the Editor in all Sections, references are to be cited in the text by number, e.g. ... Taylor<sup>3</sup> ..., and are to be arranged in the order of appearance.

In Sections B, D, E, and G, the references are to be cited in the text by the author's name and date of publication in parentheses, e.g. .... (Taylor 1932)... If the author's name is already mentioned in the text, then the year only appears in the parenthesis, e.g. ... found by Taylor (1932).... The references in these Sections are to be arranged in alphabetical order.

In Section F, references are to be cited in the text by number in square brackets, e.g. ... Taylor[3] ..., and are to be arranged in alphabetical order.

The following form should be used:

3. TAYLOR, G. I., 1932, *Proc. roy. Soc.*, A138, 41.
- Book references should be prepared according to the following form:
4. JACKSON, F., 1930, *Thermodynamics*, 4th ed., Wiley, New York.

### TYPOGRAPHY

In all matters of typography the form adopted in this issue should be followed. Particular attention should be given to position (of symbols, headings, etc. and type specification.

### ILLUSTRATIONS

Illustrations should be sent in a state suitable for direct photographic reproduction. Line drawings should be drawn in large scale with India ink on white drawing paper, bristol board, tracing paper, blue linen, or blue-lined graph paper. If the lettering cannot be drawn neatly by the author, he should indicate it in pencil for the guidance of the draftsman. Possible photographic reduction should be carefully considered when lettering and in other details.

Half-tone photographs should be on glossy contrast paper.

Illustrations should be mounted on separate sheets of paper on which the caption and figure number is typed. Each drawing and photograph should be identified on the back with the author's name and figure number.

The place in which the figure is to appear should be indicated in the margin of the MS.

### PROOFS

Authors making revisions in proofs will be required to bear the costs thereof. Proofs should be returned to the Editor within 24 hours, otherwise no responsibility is assumed for the corrections of the author.

### REPRINTS

Reprints may be ordered at the time the proof is returned. A table designating the cost of reprints may be obtained on request.

Orders in America should be addressed to the Weizmann Science Press, P.O.B. 801 Jerusalem or through booksellers, and in England and Europe to Wm. Dawson and Sons, Ltd. Cannon House, Macklin Street London W.C. 2, directly or through booksellers. Annual subscription per section (four issues): IL. 6,000 (\$6.00, £2.02). Single copy: IL. 1,500 (\$1.50, 12s.) — Manuscripts should be addressed: The Editor, The Weizmann Science Press of Israel P.O.B. 801 Jerusalem 33 King George Ave. Telephone 26345.

# **THIRD ANNUAL CONFERENCE ON AVIATION AND ASTRONAUTICS**

*Sponsored by the*

**ISRAEL SOCIETY OF AERONAUTICAL SCIENCES**

**ISRAEL ASTRONAUTICAL SOCIETY**

**DEPARTMENT OF AERONAUTICAL ENGINEERING, TECHNION-ISRAEL INSTITUTE OF TECHNOLOGY**

**DEPARTMENT OF CIVIL AVIATION, MINISTRY OF TRANSPORT AND COMMUNICATIONS**

*Under the patronage of the*

**NATIONAL COUNCIL FOR AVIATION**

**February 21, 1961: Sokolov House, Tel-Aviv**

**February 22, 1961: Technion City, Haifa**



PROGRAMME OF THE THIRD ANNUAL CONFERENCE ON  
AVIATION AND ASTRONAUTICS

Tuesday, 21 February, 1961, Sokolov House, Tel-Aviv

0.800-09.00: Registration

09.00-09.30: OPENING: U. MICHAELI, *National Council for Civil Aviation*

ADDRESS: Y. BEN-AHARON, *Minister of Transport and Communications*

09.30-11.00: *FIRST SESSION—PERFORMANCE AND OPERATIONS*

*Chairman: DAVID ABIR, Technion-Israel Institute of Technology*

An Analysis of the Landing Maneuver of  
Winged Aircraft

M. ARENS, *Dept. of Aeronautical  
Engineering, Technion-Israel In-  
stitute of Technology*

Methods of Flight Testing Abroad and in  
Israel

H. MAROM, *Flight Test Dept., Israel  
Aircraft Industries Ltd.*

Introduction of the "Boeing 707-420" Air-  
craft in El-Al

S. ESHEL, *Engineering Dept., El-Al  
Airlines Ltd.*

11.45-13.45: *SECOND SESSION—PERFORMANCE AND OPERATIONS* (continued)

*Chairman: B. ARAD, Dept. of Civil Aviation*

Artificial Rain in Israel

S. YAFFE, *Research Council of Israel*

Z. VERBA, *Israel Air Force*

Water Injection in Jet and Turbo-prop Engines

A. ROTTEM, *Dept. of Civil Aviation,  
Ministry of Transport*

Studies of Efficiency in Aircraft Maintenance

Z. SEGAL, *Israel Electric Co.*

15.15-18.00: *THIRD SESSION — AVIATION MEDICINE*

*Chairman: Y. PALGI, Department of Civil Aviation*

Medical Requirements and Flight Safety

M. LAVI, *Israel Air Force*

Airline Medical Problems

I. GLAZER, *Tel-Hashomer Hospital;  
El-Al Israel Airlines Ltd.*

The Behaviour of the Heart and Circulatory  
System in Flight

D. BARUCH, *Israel Air Force*

Problems of Oxygen and Gas Relief at High  
Altitudes

D. BORNSTEIN, *Israel Air Force*

The Auditory System in Flight

P. YARDEN, *Israel Air Force*

Problems of Vision in Flight

A. POLISHUK, *Israel Air Force*

Psychological Problems in Flight

D. BUSTAN, *Israel Air Force*

20.30: *DINNER*

*Toastmaster: A. REMEZ, Chairman, National Council for Civil Aviation*

Wednesday, 22 February, 1961

Technion City, Haifa

10.00–11.45: *FOURTH SESSION—ROCKETS AND PHYSICS OF OUTER SPACE*

*Chairman: E. D. BERGMANN, Dept. of Research and Development,  
Ministry of Defence*

An Approximate Method of Solid Propellant Internal Star Grain Calculation

A. YARON AND R. CORETT, *Dept. of Research and Development, Ministry of Defence*

The Effect of Nitromethane Additions on the Combustion of Drops of Various Fuels under Spheroidal Conditions

L. GROSS-GRONOMSKI, *Dept. of Mechanical Engineering, Technion-Israel Institute of Technology*

Investigations of the Meteorological Conditions in the Upper Atmosphere by Means of Rockets

G. STEINITZ, *Meteorological Service, Ministry of Transport*

12.00–13.10: *FIFTH SESSION—ROCKETS AND PHYSICS OF OUTER SPACE* (continued)

*Chairman: J. NEUMANN, Dept. of Meteorology, Hebrew University of Jerusalem*

Structure, Variations and Measurements of the Earth's Ionosphere and Exosphere

C. ALTMAN, *Dept. of Physics, Technion-Israel Institute of Technology*

On Extragalactic Cosmic Rays

H. KASHA, *Dept. of Physics, Technion-Israel Institute of Technology*

14.15–16.00: *SIXTH SESSION—MECHANICS AND APPLIED MATHEMATICS*

*Chairman: M. REINER, Division of Mechanics, Technion-Israel Institute of Technology*

Buckling of Thin Circular Conical Shells Subjected to Axisymmetrical Temperature Distributions

J. SINGER, *Dept. of Aeronautical Engineering, Technion-Israel Institute of Technology*

On the Physical Riemann-Christoffel Tensor in Orthogonal Coordinates

Z. KARNI, *Division of Mechanics, Technion-Israel Institute of Technology*

Hydrodynamical Applications of a Theorem on Spherical Means

E. JABOTINSKY, *Dept. of Mathematics, Technion-Israel Institute of Technology*

16.15–18.30: *SEVENTH SESSION—EXPERIMENTAL RESEARCH*

*Chairman: M. HANIN, Dept. of Aeronautical Engineering, Technion-Israel Institute of Technology*

The Mechanical Properties and Structure of Some High Tensile Alloy Steels

S. BECKER, *Israel Atomic Energy Commission*

M. G. BADER, *Battersea College of Technology, London*



Aerodynamic Research Facilities at the  
Department of Aeronautical Engineering,  
Technion-Israel Institute of Technology

Preliminary Development of an Annular  
Jet Ejector

Strain Gauge Balance for Wind Tunnels

J. ROM, *Dept. of Aeronautical Engineering, Technion-Israel Institute of Technology*

A. KOGAN AND M. VICTOR, *Dept. of Aeronautical Engineering, Technion-Israel Institute of Technology*

A. KOGAN, E. SCHWARTZ AND  
A. SEGNER, *Dept. of Aeronautical Engineering, Technion-Israel Institute of Technology*

18.45: *ANNUAL MEETING OF THE ISRAEL ASTRONAUTICAL SOCIETY*



# AN ANALYSIS OF THE LANDING MANEUVER OF WINGED AIRCRAFT

M. ARENS

*Department of Aeronautical Engineering, Technion-Israel Institute of Technology, Haifa*

## ABSTRACT

The landing maneuver as defined by FAA regulations is analyzed without regard to the ground effect. It is shown that if the flare segment is neglected the optimum maneuver prior to touch-down consists of a glide segment and one or at most two level deceleration segments. If the flare segment is considered, it is shown that for most aircraft the optimum landing maneuver consists of a glide segment, a flare flown at maximum  $C_L$ , and a level deceleration segment.

## 1. INTRODUCTION

Considering the degree of importance currently attached to aircraft landing and take-off distance, it seems desirable to analyze the aircraft landing maneuver in order to determine the flight path giving the minimum landing distance. Based on the requirements of reference 1, the origin of the landing maneuver is defined by an altitude of 50 feet, a speed of 1.3 times the stalling speed in the landing configuration, and an aircraft attitude with respect to the horizontal as determined by the steady glide angle at that speed. The landing distance is the horizontal distance required to land and come to a complete stop.

Since the speed at which the aircraft contacts the runway will generally be limited by safety and/or structural considerations, the landing path may be conveniently broken down into the following two independent segments.

1. Descent from an altitude  $h_1$ , velocity  $V_1$ , and attitude  $\theta_1$  to ground level, velocity  $V_2$ , and zero attitude.
2. Deceleration from velocity  $V_2$  to zero velocity at zero altitude (on the runway). Needless to say, minimum landing lengths are obtained when maximum permissible touch-down speeds are used, due to the large deceleration provided by wheel brakes, drag brakes, and thrust reversers.

Minimizing the first segment requires finding the function  $\theta(h)$  that minimizes the integral

$$\int_{h_1}^{h_2} \frac{dh}{\tan \theta}$$

subject to the equations of motion of the aircraft and the aircraft's aerodynamic and structural limitations. This is a straightforward problem in the calculus of variations. The differential equations defining various types of optimum flight paths in the vertical plane have been derived by Miele<sup>2</sup>, however, except for a few restricted cases, no general solution can be obtained. However, if the aircraft is restricted to small deviations from the glide path, as would generally be the case due to safety, aerodynamic, and structural limitations, the optimum flight path may be deduced on the basis of relatively simple considerations.

The minimizing condition for the second segment is easily found by determining the angle of attack at which the maximum braking force is obtained.

It might be noted that books dealing with aircraft performance generally restrict their analysis of the descent segment to rectilinear paths<sup>3,4</sup>.

## 2. RECTILINEAR DESCENT

If the flare distance is neglected and the descent is restricted to rectilinear flight paths, the distance to touch down is given by

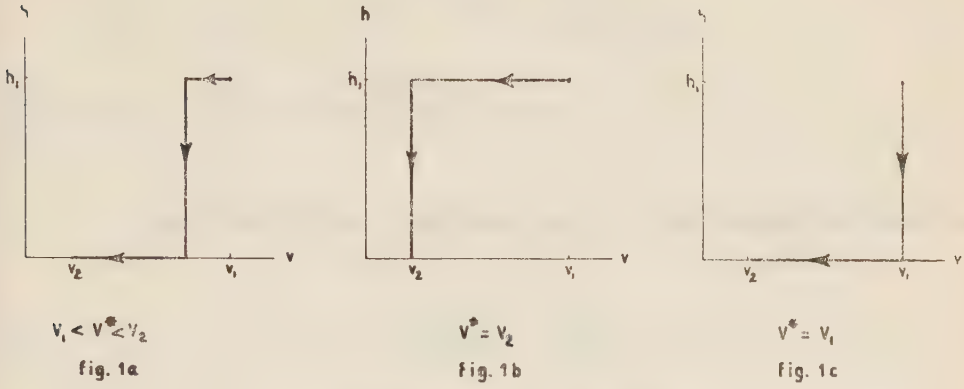
$$l = -W \left[ \int_{h_1}^{h_2} \frac{dh}{D - T} + \frac{1}{g} \int_{V_1}^{V_2} \frac{V dV}{D - T} \right] \quad (1)$$

If only flight paths of small inclination are considered, so that the lift can be considered equal to the aircraft weight, then neglecting ground effects  $D = D(V)$ , since the change in altitude is extremely small. Considering a constant throttle setting (idle) as required by reference 1, the denominator of both integrals is a function of  $V$  only. Moreover, the second integral depends only on the limits of integration, irregardless of the flight path considered. Obviously then, minimizing 1 requires that the drag minus thrust be maximum during that portion of the flight path involving a change in altitude. Thus the optimum descent must be composed of a constant velocity glide segment between altitudes  $h_1$  and zero, plus one or at most two constant altitude decelerations, at  $h_1$  and/or zero altitude, Figure 1. For jet aircraft using flaps the maximum  $D - T$  will usually occur at  $V_1$  and the optimum descent will consist of a glide to ground level at  $V_1$  and a deceleration at ground level from  $V_1$  to  $V_2$ , Figure 1c.

## 3. FLARE DISTANCE

For a more accurate estimate of the landing length the necessary change in flight attitude should also be considered, even though the "flare" length will generally

be a small fraction of the total landing length. Lifting the restriction of rectilinear paths to the descent will also change the optimum descent maneuver.



OPTIMUM DESCENT (RECTILINEAR)

FIG. 1

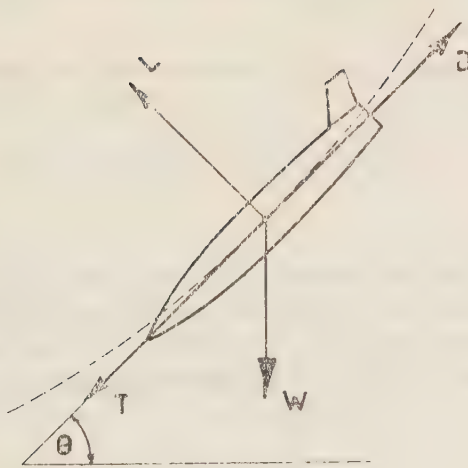


Figure 2  
Landing flare



Using the notation of Figure 2, the equations of motion of the aircraft are

$$T + W\theta - D = \frac{W}{g} \frac{dV}{dt} \quad (2)$$

$$L - W = -\frac{W}{g} V \frac{d\theta}{dt} \quad (3)$$

for aircraft attitudes of small  $\theta$ . From equations (1) and (2) one obtains

$$\frac{dV}{dl} = \frac{T + W\theta - D}{W/g V} \quad (4)$$

$$-\frac{d\theta}{dl} = \frac{c_L \rho g}{2W/S} - \frac{g}{V^2} \quad (5)$$

where the lift has been expressed in terms of the lift coefficient in equation (5).

Equation (5) shows that for minimum pull-up lengths changes in attitude should be accomplished at maximum permissible lift coefficients and velocities. As will be shown later the change in velocity that can be anticipated during the flare is small. If the change in velocity is neglected, the shortest flare is one carried out at highest permissible  $C_L$ .

By introducing the drag coefficient equation (4) can be transformed to

$$\frac{dV^2}{dl} + \frac{c_D \rho g}{W/S} V^2 = 2g T/W + 2g\theta \quad (6)$$

The aircraft trajectory, and therefore the horizontal length required for a given maneuver, is determined by the simultaneous solution of equations (5) and (6). Noting that the term involving  $\theta$  in equation (6) is small and that the velocity change during the turn is small, a good approximation can be obtained by substituting

$$\theta \cong \theta_1 - 2g \int_0^l \left( \frac{c_L \rho g}{2W/S} - \frac{g}{V_1^2} \right) dl \quad (7)$$

into equation (6). If attention is restricted to maneuvers flown with  $C_L$  equal to the maximum permissible  $C_L$  throughout, equation (6) takes the form

$$\frac{dV^2}{dl} + \frac{c_L \rho g}{W/S} V^2 = 2g(T/W + \theta_1) - 2g \left( \frac{c_L \rho g}{2W/S} - \frac{g}{V_1^2} \right) l \quad (8)$$

The solution to this equation is

$$V^2 = e^{-\frac{c_D \rho g}{W/S} l} \left\{ V_1^2 - \frac{1}{c_D \rho} \left[ 2T/S + W/S \left( 2\theta_1 + \frac{c_L - c_{L1}}{c_D} \right) \right] \right\} + \frac{1}{c_D \rho} \left[ 2T/S + W/S \left( 2\theta_1 + \frac{c_L - c_{L1}}{c_D} \right) \right] - gl \left( \frac{c_L - c_{L1}}{c_D} \right) \quad (9)$$

where the subscript 1 indicates conditions prior to the initiation of the pull-out.

Substitution of equation (9) into equation (5) gives the differential equation of the trajectory.

$$-\frac{d\theta}{dl} = \frac{c_L \rho g}{2W/S} - \frac{g}{a - bl + ce^{-pl}} \quad (10)$$

where

$$a \equiv \frac{1}{c_D \rho} \left[ 2T/S + W/S \left( 2\theta_1 + \frac{c_L - c_{L1}}{c_D} \right) \right]$$

$$b \equiv g \left( \frac{c_L - c_{L1}}{c_D} \right)$$

$$c \equiv V_1^2 - a$$

$$p \equiv \frac{c_D \rho g}{W/S}$$

Equation (10) cannot be integrated in closed form. Noting, however, that  $p \ll 1$  for conventional aircraft, equation (10) can be written as

$$-\frac{d\theta}{dl} = \frac{c_L \rho g}{2W/S} - \frac{g}{(a + c) - (\gamma p + b)l} \quad (11)$$

The solution of equation (11) is

$$\theta_1 - \theta = \frac{c_L \rho g l}{2W/S} + \frac{1}{2\left(\frac{c_D}{c_{L1}} - T/W - \theta_1\right)} \ln \left[ 1 - \frac{2gl}{V_1^2} \left( \frac{c_D}{c_{L1}} - T/W - \theta_1 \right) \right] \quad (12)$$

Computation of some sample cases indicates that equation (12) gives an excellent approximation for the "flare" segment of conventional winged aircraft. In fact, in many cases the accuracy obtained by using equation (7) is sufficient. The results of a sample calculation are shown in Table I.

TABLE I

*Sample calculation of horizontal distance, change in velocity and height during flare executed at sea level*

$W/S$ lb/ft <sup>2</sup>	$T/W$	$\theta_1$ rad	$c_{L1}$	$V_1$ ft/sec	$c_L$	$c_D$	length ft.	$\Delta V$ ft/sec	$\Delta h$ ft.
50	0.02	0.112	1.183	188	2	0.288	186	3	10

The change in altitude during the pull-up is given by

$$\Delta h = - \int \tan \theta dl \quad (13)$$

Integrating equation (13) one obtains

$$h = h_1 - \theta_1 l + \frac{c_L \rho g}{2W/S} \frac{l^2}{2} - \frac{V_1^2}{4g \left( \frac{c_D}{c_{L1}} - T/W - \theta_1 \right)^2} \left\{ \left[ 1 - \frac{2gl}{V_1^2} \left( \frac{c_D}{c_{L1}} - T/W - \theta_1 \right) \right] \cdot \right. \\ \left. \ln \left[ 1 - \frac{2gl}{V_1^2} \left( \frac{c_D}{c_{L1}} - T/W - \theta_1 \right) \right] + \frac{2gl}{V_1^2} \left( \frac{c_D}{c_{L1}} - T/W - \theta_1 \right) \right\} \quad (14)$$

If the time to effect changes in angle of attack are neglected, ( $I \approx 0$ ), the total descent distance is given by the summation of the glide, flare, and deceleration distances.

#### 4. OPTIMUM DESCENT

For an aircraft for which the maximum  $D - T$  in level flight occurs at the speed  $V_1$ , the glide and flare should obviously be executed prior to deceleration. However, the question arises whether a glide to the height required by the flare, followed by



a minimum distance flare and subsequent deceleration represents the optimum descent maneuver. Two alternatives may be considered:

1. Extending the flare portion at the expense of the glide, by flaring at a  $C_L$  less than the maximum permissible value.
2. Depressing the nose during some portion of the descent so as to accomplish a change in altitude at little expense in horizontal distance.

As for the first alternative, its utility hinges primarily on whether decreasing the lift coefficient during the flare will lead to a lower aircraft velocity at the end of the flare.

If for small  $\theta_1$ 's the velocity at the completion of flare is approximated by

$$V^2 \cong V_1^2 e^{-\frac{c_D \rho g}{W/S} l_f} \quad (15)$$

and the flare plus glide distance by

$$l \cong \frac{\theta_1}{\frac{c_L \rho g}{2W/S} - \frac{g}{V_1^2}} - \frac{\Delta h_\theta}{\left(\frac{D-T}{W}\right)_{gl}} \quad (16)$$

where

$$\Delta h_{gl} \cong \frac{\theta_1^2}{2 \left[ \frac{c_L \rho g}{2W/S} - \frac{g}{V_1^2} \right]} - h_1 \quad (17)$$

It is seen that  $\frac{dl}{dc_L} < 0$ , and  $\frac{dV}{dc_L} < 0$  except for

$$c_L < \frac{1}{4k W/S} \quad (18)$$

Since the lift coefficient required during the landing maneuver exceeds  $\frac{1}{4k W/S}$  for conventional aircraft, this approximate analysis indicates that the flare should be flown at the maximum permissible  $c_L$ .

The utility of the second alternative, depends on whether the horizontal distance required for the dive and subsequent pull-out is smaller than the horizontal distance required to glide through the same altitude change.

Neglecting the velocity changes during the maneuvers involving changes in attitude, and assuming each maneuver flown at a constant  $c_L$  the horizontal length required for a maneuver involving a change of attitude  $\Delta\theta$  is

$$l = - \frac{\Delta\theta}{\frac{c_L \rho g}{2W/S} - \frac{g}{V_1^2}} \quad (19)$$

The change in height during the maneuver is then

$$\Delta h = -l \frac{\Delta\theta}{2} \quad (20)$$

For best results the dive should be executed at minimum  $c_L$ , the pull-ups at maximum  $c_L$ . For the purpose of this analysis the diving  $c_L$  will be taken as zero.

The descent to ground level is thus composed of the following segments, Figure 3:

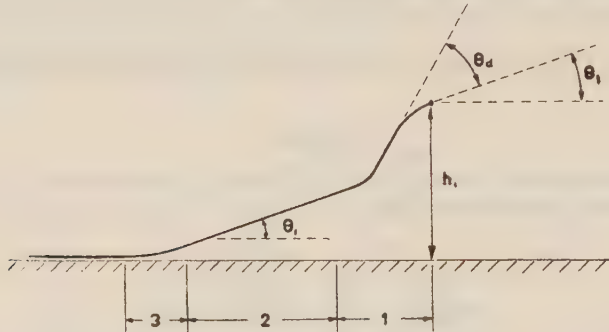


FIG. 3  
DESCENT INCLUDING DIVE

1. A diving maneuver at zero  $c_L$  through the angle  $\Delta\theta_d$  followed by a recovery at maximum permissible  $c_L$  through the angle  $-\Delta\theta_d$ .
2. A glide at the glide angle  $\theta_1$
3. A flare at maximum permissible  $c_L$  to  $\theta = 0$

The total distance covered neglecting the aircraft's moment of inertia, will be

$$l = \frac{\Delta\theta_d V_1^2}{g} + \frac{\Delta\theta_d}{\frac{c_L \rho g}{2W/S} - \frac{g}{V_1^2}} - \frac{\Delta h_{gl}}{\left(\frac{c_D \rho V^2}{2W/S} - T/W\right)_{gl}} + \frac{\theta_1}{\frac{c_L \rho g}{2W/S} - \frac{g}{V_1^2}} \quad (21)$$

It is desired to find a stationary condition on  $l$ , subject to the requirement that the total altitude covered ( $h_1$ ) is constant:

$$h_1 = -(\Delta h)_{gl} + \frac{(\Delta\theta_d)^2}{2} \left[ \frac{V_1^2}{g} + \frac{1}{\frac{c_L \rho g}{2W/S} - \frac{g}{V_1^2}} \right] + \frac{\theta_1^2}{2 \left[ \frac{c_L \rho g}{2W/S} - \frac{g}{V_1^2} \right]} \quad (22)$$

Differentiating eq. (21) we find that a maximum on  $l$  is obtained at

$$\Delta\theta_d = \theta_1 \quad (23)$$

Therefore, if the nose is depressed through an angle equal to the glide angle the landing distance will be a maximum. In fact, any improvement over the conventional landing maneuver requires that

$$\Delta\theta_d > 2\theta_1 \quad (24)$$

Since such a maneuver will generally violate safety requirements, and since for smaller angle dives the landing distance is increased, it is concluded that the nose should not be depressed if minimum landing length is desired.

#### GROUND EFFECT

The analysis of this paper has disregarded the ground effect on the aircraft aerodynamic characteristics. This effect may lead to a significant reduction in the induced drag of the aircraft in proximity to the ground. Since the height at which this effect becomes significant depends on the wing aspect ratio, wing location, and aircraft size, no general conclusions regarding the influence of the ground effect on the optimum maneuver can be stated.

#### CONCLUSION

For aircraft for which the ground effect can be neglected, and for which the level flight drag minus idle thrust is larger at 1.3 times the stalling speed than at the touch down speed, the optimum landing maneuver consists of the following sequence:

1. Glide at 1.3 times the stalling speed down to the height required for the flare.
2. Flare at maximum permissible  $c_L$ .
3. Level deceleration at ground level to touch-down speed..

#### NOMENCLATURE

$c_D$ — drag coefficient	$S$ — wing area
$c_L$ — lift coefficient	$T$ — engine thrust
$D$ — aircraft drag	$t$ — time
$g$ — acceleration of gravity	$V$ — aircraft velocity
$h$ — height of aircraft center of gravity	$V^*$ — velocity for maximum drag minus thrust in level flight
$k = \partial c_D / \partial c_L^2$	$W$ — aircraft weight
$I$ — aircraft moment of inertia	$\theta$ — attitude with respect to the horizontal
$L$ — aircraft lift	$\rho$ — air density
$l$ — horizontal distance	

#### Subscripts

1 — origin of landing maneuver	$f$ — flare
2 — touchdown	$gl$ — glide
$d$ — diving maneuver	



## REFERENCES

1. Civil Aeronautics Manual 4b, "Airplane Airworthiness; Transport Categories", Federal Aviation Agency, May 1, 1960, p. 38.
2. MIELE, ANGELO, 1959, Minimal Maneuvers of High Performance Aircraft in a Vertical Plane, NASA TN D-155, September.
3. PERKINS, C. D. AND HAGE, R. E., 1957, *Airplane performance stability and control*, John Wiley, New York, p. 198.
4. CORNING, G., 1953, *Supersonic and Subsonic Airplane Design*, College Park, Md., p. 2: 13.

# METHODS OF FLIGHT TESTING ABROAD AND IN ISRAEL

H. MAROM

*Flight Test Department, Israel Aircraft Industries*

## OBJECT

The object of this lecture is to summarize briefly methods of flight testing up to date, underlining the importance of standardisation and complexity encountered in meeting modern engineering requirements and to what extent have we in Israel succeeded in keeping up to date.

In this limited lecture I'd like to bring to the reader's notice certain of our instrumentation improvements, and the possibilities of applying local know-how using already available standard test equipment.

## INTRODUCTION

On December 17th, 1903, at Kittyhawk, USA, Orville Wright flew for 12 seconds in a powered aeroplane. Orville and Wilbur Wright utilised just these principles of lift stability and control which Leonardo da Vinci had understood 400 years before. These men were pioneers in every field—they designed and built their own aeroplane, engine and propellers. They even designed their own wind tunnel, they were their own stressmen and calculated the loads to which the aeroplane would be subjected and perhaps most interesting of all—they were their own test pilots.

They were the world's first test team and as such are the finest example for all aspiring test teams to learn about and to follow, for they understood their aeroplane in every detail.

There were three main periods of development in flight testing: First when every pilot was his own test pilot, then when systematic testing was being introduced and finally, when all test flying has been geared to a carefully devised plan.

It is interesting to note that even with whole batteries of automatic recording instruments with telemetering and film monitoring, the test pilot's humble kneepad with its two attached pencils is still as essential as ever, but no longer in the same concept as it was understood only a very short time ago when these few scribbled down words constituted the feelings, impressions, views, opinions, ideas, hallucinations and even scares of many a test pilot. And even if more than one test pilot had the chance to add his own version of the aircraft's qualities it would again be

expressed in a collection of some kind of the above mentioned impressions, which when fed back to the design teams brought forth varying results in the final product, very much dependent on that individual which up to this time was the main flight test instrument, — an instrument of variable reliability, in a science which as the number of variable parameters grew was fighting hard to reduce the great number of these variables to enable the designer's equations to have results written out as figures and not impressions and feelings.

It became obvious that the test pilot would have to be eliminated as a reading and recording instrument and that not only would he have to be replaced by instrumentation he alone could no longer handle the task of preparing, executing and exploiting each flight.

As in a number of other fields it was the French who soon after World War II set up the first Flight Test Personnel School which differed from all existing British and U.S. Schools in the fact that not only were test pilots turned out, but the first complete test teams trained. Each such team consisted of a Test Pilot, Flight Test Engineer, Flight Test Observer and Flight Test Mechanic.

In practice, to-day it is not the aircraft or the engine which are the subject of a specific test program but each quality and quantity of even the smallest modification become the subject of project which once submitted for testing by the designers, becomes a project of such a complete Flight Test Team. The measurement of qualities and quantities which face all those that venture into aircraft design modification and even maintenance to-day are common and although in most countries they are still called by different names they are more or less derived from the same basic exercise of metal moving through the atmosphere. This atmosphere is the same for the American Boeing, F-104 and Polaris as it is for the British Comet Lightning and Blue Streak and for the French Caravelle, Mirage and Veronique, but in each one of these countries, which to-day represent the last word in aviation development, was each goal achieved at a different cost to the taxpayer.

Until recently, and even in many instances to-day, the American and British aviation industries have little standardisation in flight testing although every attempt is being made to standardise. It is most probably due mainly to France's limited budget that she has succeeded in catching up with the Western World since the war but in many a case surpassed their achievements especially in the field of flight test instrumentation standardisation. This French success can and is being put down, to standardisation and teamwork which are the two main mottos of flight testing in France.

Knowing well the many ways of the many U.S. and British aviation schools manufacturers and organisations, each with its own well proven method, it is important to appreciate that in France to-day there is one language in flight testing, one catalogue of standard flight test instruments and one manual of flight test methods.

When the Advisory Group for Aeronautical Research and Development of NATO was founded, Theodore Von Karman, its Chairman, wrote a preface which well



describes the situation existing, namely, "We found there was a great need for a flight test manual covering performance, stability and control, and instrumentation of aircraft that could be used by design, development or research engineers, test pilots and instrumentation personnel of the participating nations in order to expand their knowledge, improve their methods, *and standardise their techniques*. Although various members of NATO have their own separate publications covering the subjects contained therein, AGARD recognised the need for the compilation, revision, and enlargement of this material for the benefit of all NATO nations".

#### STANDARDISATION

To-day this manual is available to all, not only NATO nations, and with it not only the USA and Britain are trying to adopt the standard method as used by France but also others like Italy, Germany, Argentina, India and Spain.

It was not by chance that we in Israel turned for our flight test training to France but mainly because we realised that our way if any had to be the cheapest and best and most important of all, one which would enable us at all times to turn to someone else and compare results. Such comparison of flight test results is only possible economically if the two bodies comparing use standard methods and use standard recording and measuring equipment. It is at this point that I would like to explain what exactly standardisation of test methods and test equipment can do for the aviation industry.

Any potential customer, whether he be in the form of a Buyer, Subcontractor or Operator, interested in investigating, modifying or even redesigning his aeroplane, is confronted with having to satisfy the requirements spelled out in the language of the original airworthiness authority, when he comes to official certification tests.

It will now save time and expense to a great extent if he is able to carry out his tests in the same manner, using test equipment known to that original authority. Knowing which equipment the original designer used his task becomes easier and far more realistic if his results can be compared at every individual stage of testing to those of the designer and he can soon spot the point at which he is either erring or approaching any red line. If at this stage he is in doubt all he has to do is to advise the original designer which pick-ups he used send the standard recorder film in original to the designer and he can then await his comments without having to provide him with calibrations and reports full of details of the way he measured and trying to prove to the original designer that his own non-standard test equipment was not at fault in providing unexpected results.

Let us assume for the purpose of this discussion that some form of standardisation has been achieved by most serious concerns and authorities in the world, still leaving us sufficient elbow room to pick and choose of the various available standard schemes, that scheme, which suits the test data acquisition program best economically, time-wise and accuracy wise.

## INSTRUMENTATION

The basic function of any particular flight test data acquisition program can often be satisfied by any of several known schemes, some more widely known and used, others less. Each of these schemes, however, has certain short-comings and advantages. In order to insure that the basic limitations and capabilities of a particular instrumentation system are fully appreciated, it is important that initially the system be considered as a whole.

Instrumentation design under a systems concept requires extensive consideration of overall system and component performance, and must be based on a compromise of the best features of each subsystem. Rather than adding complexity it is usually a requirement to reduce complexity, reduce weight, and increase reliability. System approaches to component design often increased system flexibility. This point of flexibility will be raised later especially as it concerns our local requirements.

Through the careful application of these principles, significant advantages can be gained in instrumentation systems in terms of increased capability, performance, and reduced weight, space and power requirements and improved reliability.

Another part of flight test data acquisition systems planning is the desirability to consider the data reduction and computation process as part of the basic system in order to take full advantage of the automatic data reduction aids which have been developed. Certain measurement techniques lend themselves more easily to automatic analysis procedures than others. It is therefore desirable to establish the data analysis technique at the same time that an instrumentation system is planned.

There are eight significant factors which must be considered at the beginning of any flight test program before one can begin a detailed plan and design of the instrumentation system let alone the long and usually expensive purchasing and parts manufacturing period which cannot be overlooked at the outset.

Engineering-wise these factors concern both aerodynamic and instrumentation facets of the problem and can be summarised as follows:

- 1) Number of items to be measured.
- 2) The dynamic response required of the measuring system.
- 3) The form of the final record which is desirable.
- 4) System complexity which is intolerable.
- 5) The degree to which automatic data reduction and computation is both feasible and desirable.
- 6) The desirability of pre-recording computation.
- 7) Required accuracy for the aerodynamic data.
- 8) Availability of equipment, facilities and experience.

In order to indicate the significance of each of the above factors, a short discussion of each is presented here with an example out of our own short Israeli experience where possible.

In order to understand the following explanations it should be quite clear to the reader that the Flight Test Department receives the demand for flight test results in the form of a technical report stating full details of the theoretical work done up-to-date indicating which parameters have to be proven in flight, which are required for further theoretical work and finally the form and accuracy of the desired information.

The design and programming of the complete flight test system is now the responsibility of the Flight Test Team which will now consider the above eight factors to determine the best and most economical way of replying to the Engineering Department.

### *Number of information channels*

Engineering request demanded the measurement of fuel flows, pressures and temperatures, air pressures and temperatures in an existing fuel system in sections where modifications were anticipated with the intent of repositioning certain fuel system components to make space available for other aircraft equipment. The accuracy of the required results was indicated, and obviously, results were required for the entire flight domain of the aircraft. Drawings of the system were supplied indicating sections where each measurement had to be made.

It is easy in any test program to justify any aircraft environmental or meteorological measurement and interestingly enough all these flight variables offer some practical interest. There is clearly now, a necessity to determine an order or priority as regards the various parameters it would be desirable to measure. Not only priority with respect to sequence or order but certain parameters, will have to be measured at the same instant and so the characteristics of the recording systems available will have to be examined and due consideration given to the number of parameters required at a later stage of the test program. One part of the exercise would be to obtain these parameters in the same sections of the fuel system where changes would occur in addition to further measurements which have to be made for a new system anyhow.

The number of variables measured had a lot to do in determining the combination weight and size of the instrumentation system. Since the weight and size were somewhat fixed due to the aircraft structural limitations the only way we could accommodate the required number of measurements was by the use of time sharing instrumentation, to record on a single channel the large number of temperatures required. On one channel we succeeded in getting 16 temperature measurements. This of course saved the number of available channels but made the unscrambling more complicated and brought with it a risk of losing 16 parameters jointly due to the malfunctioning of that one channel.

During this test we used two large A13 Hussenot recorders (see figure 1), giving us only twelve traces on each recording instead of a possible sixty which is a theoretical possibility but a film assessors nightmare.



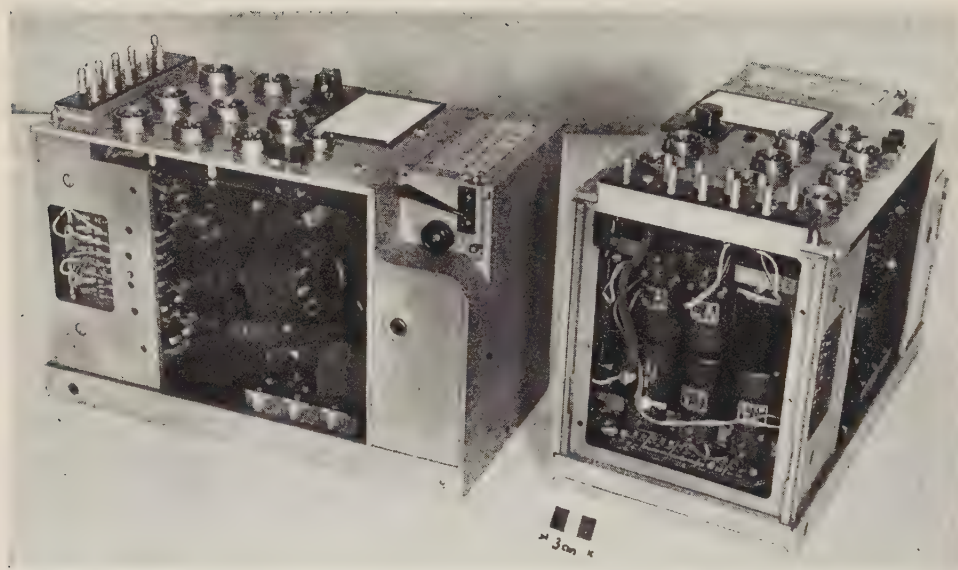


Figure 1  
A13 Hussenot Recorder

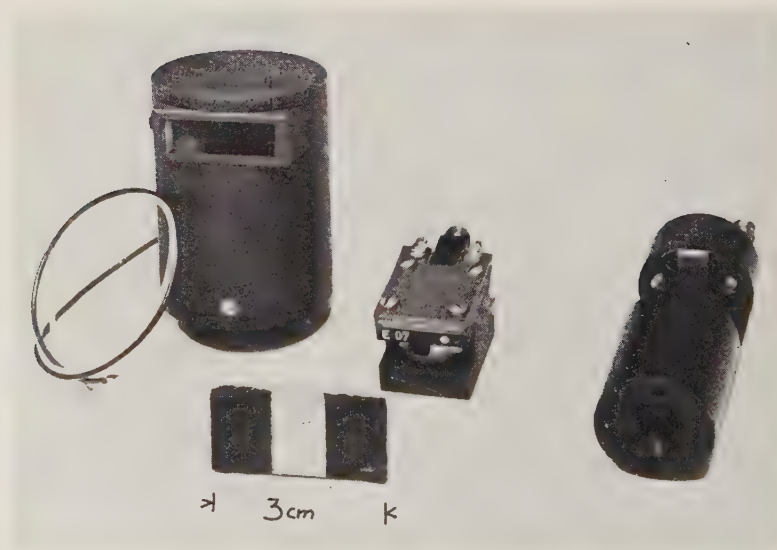


Figure 2  
Oscillographs, Quotimeters, Recorder

### *Dynamic response*

The dynamic response required of any measurement system is dictated solely by the nature of the experiment and can usually be determined in advance of any testing. The dynamic or frequency response of a measurement system is usually established by the response characteristics of the transducers and recording devices used in the systems. Those transducers and recorders (see Figure 2) which are capable of high dynamic responses are also capable of sensing and recording a large variety of extraneous noises. Any increase in the signal band width capacity increases the noise band width capabilities.

This is a factor which can cause a large deterioration in the quality of the measurement record.

In the particular test of our fuel system the parameters to be measured were divided into two groups. The first group consisted of those that varied slowly; temperatures and environmental conditions and the second group varied faster; pressures and those parameters which were used to establish the response of the flight vehicle itself. As it is impractical to incorporate in a single flight test instrumentation system a variety of recorder response characteristics two separate recorders (see Figure 3) were used containing recordings of parameters according to their dynamic response.

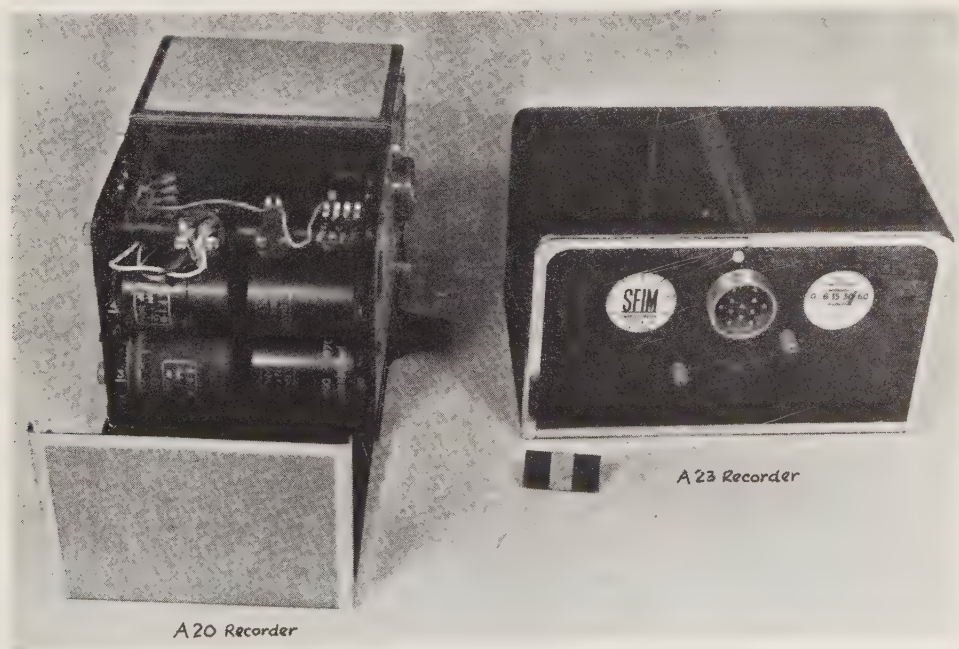


Figure 3  
A20 and A23 Recorders

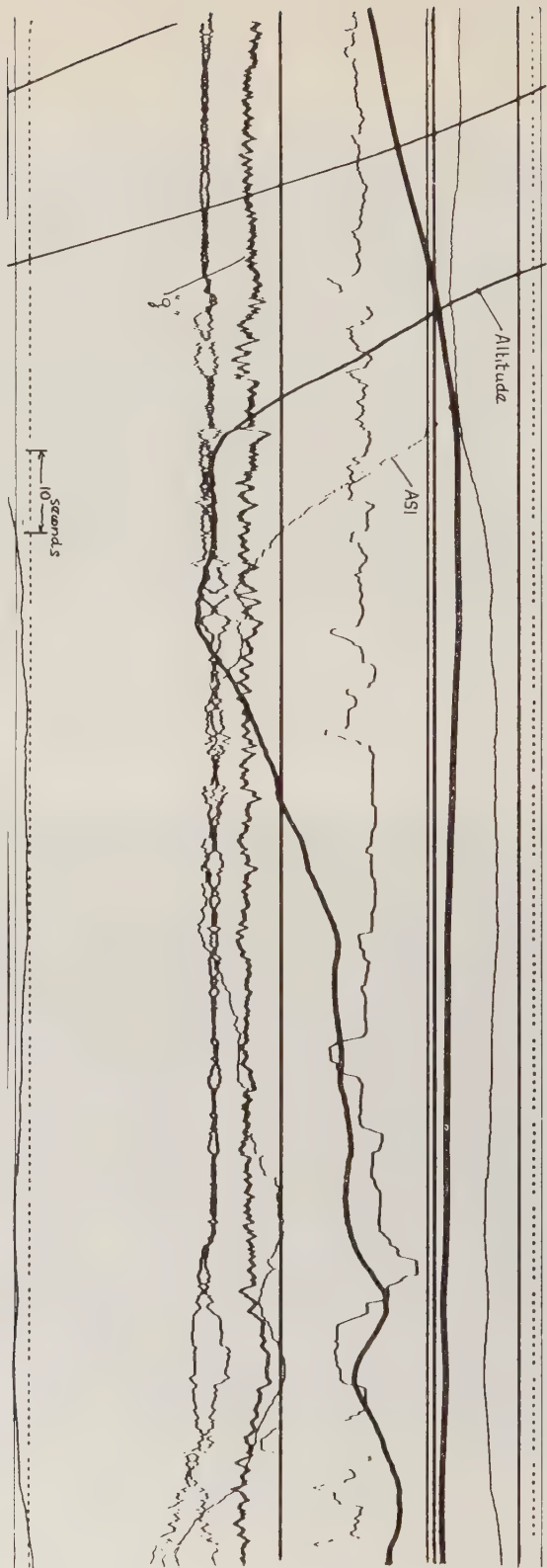


Figure 4  
Optical oscillograph recording of descent and levelling off in jet A/C. (89 mm. film)



### *Record form*

In the matter of the form of the record in which the measurements are to be stored, there are two major choices available, visual or electrical. The visual form of record can be illustrated by data storage which consists of notes put in a book form by a human observer or by lines on a photosensitive film or paper made by an optical recording oscillograph (see Figure 4) or by photographs of groups of instruments obtained in a photographic observer (see Figure 5).

Electrical data storage can be accomplished by the creation of a magnetic field which is proportional to the quantity being measured, and the storage of this magnetic field on a magnetic tape, wire or drum.

In tests comparing two types of artificial horizons we used a combination of both methods.

A photographic type A20 recorder (see Figure 3) was used to carry all environmental parameters as airspeed, altitude, acceleration in  $Z$  and  $X$  axis, outside air temperature

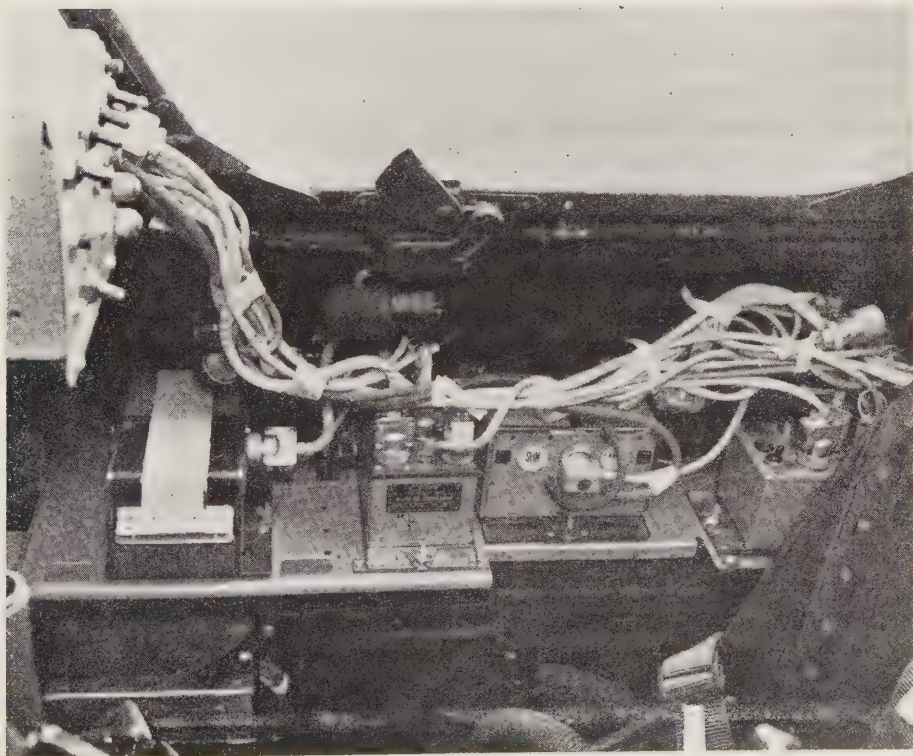


Figure 5

Photographic observer photograph of side of cockpit and position of switches

and a time base. A flight test observer was placed behind both instruments which were installed at eye level next to each other and he compared the indications against a common calibrated scale, noting down all final positions in both form and described the general behaviour of both on a magnetic tape.

Photography of the instruments was not used as in this sole test requiring a cockpit camera installation the method chosen was more economical than installing a cinecamera.

The chief difference between the visual and electrical forms of recording from the point of view of the overall system design, lies in the ease with which the data can be handled in computation process.

A visual record is simple and convenient, to determine trends. It must be read by a human operator before any further computation can be accomplished (see Figure 4).

An electrical record form is far from flexible and lends itself easily to computation, analysis, expansion and mass data consumption which in cases where very large aircraft are concerned becomes the solution of the problem.

### *System complexity*

An important factor in determining system complexity is the desired scope of the instrumentation system.

If an instrumentation system were planned to solve all of the possible measurement problems of the flight tester, there would be produced, no doubt, a system unworkable due to its complexity, size and weight.

To avoid the creation of such an unwieldy system, the complexity which is permissible should be clearly established after carefully weighing the advantages and disadvantages to be gained by each additional degree of complexity. The factor which quite frequently establishes the upper bounds on tolerable complexity is often the limitation imposed by the availability, time, funds and personnel in a flight test program.

In one particular test in which the normal position of the aircraft static could not be utilised complexity was reduced by applying a principle of comparative measurements. An accurate static measurement was made on a standard aircraft by a long boom static. Boom readings were recorded for the standard aircraft together with its normal static for the entire speed range. When the same boom fitted in the same position on the non-standard aircraft was made the comparative recording showed the actual difference between the two statics.

### *Automatic data reduction*

The choice between manual and automatic data reduction is usually determined by the nature of the data and by the amount of computation required, also by the volume of data which has to be processed.

Up to now most of our data reduction has been manual but with flight test work on a prototype in the future, it will become imperative to use automatic data reduction to keep up with a rapid test program, correcting flaws in between each flight. In some cases where the volume is not large but rather complex, such as in vibration measurements, the desired information will have to be extracted by harmonic or spectrum analysis techniques.

### *Prerecording computation*

We use three methods: mechanical, electromechanical and one that utilizes electronic means of performing the computation.

An airspeed indicator is an example of the first where instead of measuring and recording and then calculating from total and static pressures the airspeed, this is done by a mechanical computation. An altimeter also falls into this category. An illustration of an electro-mechanical type of computation was the use of a trigonometrical resolver to obtain the longitudinal and lateral components of a cyclic quantity in a helicopter flight test.

In this type of measurement, cyclicly varying quantities on each of the helicopter blades were multiplied by the sine or cosine of the angle between the blade and the lateral or longitudinal direction.

The above types of prerecording computation can increase the accuracy, reduce the number of channels and reduce materially the amount of data reduction required.

Prerecording computation has been especially important in Israel when cost considerations ruled out the use of automatic data reduction schemes at this stage.

### *Accuracy*

A major effort in missile and aircraft instrumentation development has been directed towards increased accuracy.

Cost of instrumentation is directly proportional to accuracy to a point where from then on accuracy increases in no measurable proportion to cost. Smoothing is one of the important methods of increasing accuracy capabilities of a given system.

The importance of a realistic estimate for required accuracy cannot be expressed too strongly. The overstating of the required accuracy leads to unnecessary extensive labours and needless system complexity. When the designer requests a degree of accuracy without a clear understanding of what this accuracy implies with regard to the measurement system, the instrumentation system designer often includes a host of nonessential stabilising devices such as power supply regulator, temperature compensators etc. which increase bulk and cost of the system.



The determination of experimental accuracy has been a source of controversy ever since the first measurement was made. The basic reason for this conflict lies in our inability to determine true values and the difficulty of one person estimating for others the accuracy of his data. Within anyone country, or between countries the meaning of accuracy terminology varies, and so here in Israel, where we have engineers trained in all four corners of the world the factors affecting accuracy vary as much as the different meanings of words like resolution, sensitivity, linearity etc.

### *Equipment facilities and experience available*

These factors have the greatest bearing on flight test instrumentation systems. Equipment available here in Israel is mainly French.

Facilities are of varied origin and our experience is mainly on the equipment available in Israel at the moment.

We have made extensive use of available non standard instrumentation but always in such a way as not to affect the final standard recording which is used for comparison.

When the choice of a particular instrumentation system is made by assessing each of the above factors in accordance with its logical influence on the overall plan, the result is a system which is as simple as it can be and yet which satisfies the basic aerodynamic requirements.

The proper balance between instrumentation capabilities and limitations and the desirable aerodynamic requirements results in a system which is likely to be reliable and compact.

### FLIGHT TECHNIQUE

Much has been said about instrumentation for the purpose of recording and little consideration has been given to the old recorder, the test pilot, and his flight instruments which have considerable bearing on the accuracy of the entire system.

Our aircraft have become a complex system requiring accurate handling where mechanical controls have been replaced by hydraulic and electric systems. The parameters operating them have much narrower margins of operation and require to be kept within these narrow ranges of pressures, temperatures and airspeeds to keep the entire system functioning properly.

The test pilot can no longer in addition to flying, keep a log, act as the flight test observer etc., but his main job is to fly the aircraft to the limits of human accuracy which are with proper training narrower in many cases than those that we are able to get from any other type of known flight operator whether remote or automatic.

Where an average pilot expects to fly within  $\pm 100$  ft at 40000 feet (see Figure 6a), the test pilot is expected, during stabilisation (see Figure 6b), to keep within  $\pm 5$  feet, a feat requiring deep concentration and in many cases unusually great effort.

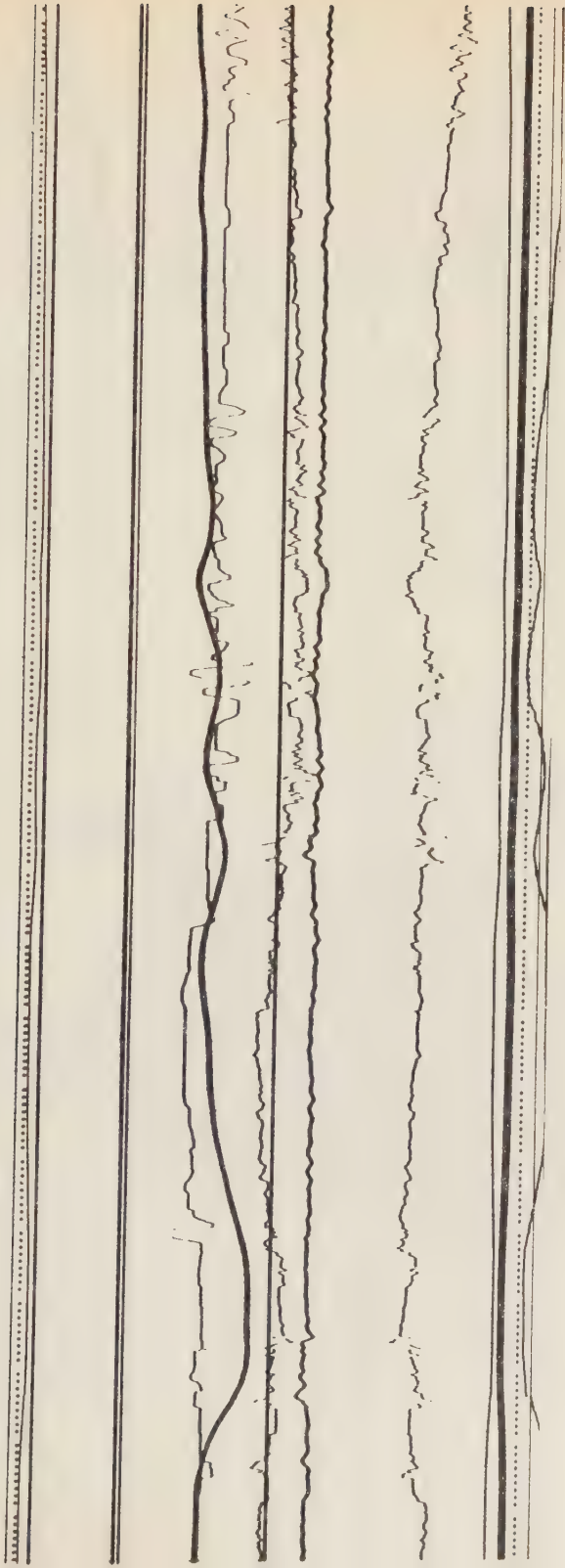


Figure 6a  
Recording from average pilot's accurate flight

$\Delta p_{sens}$   $\rightarrow$

$\Delta p_{\beta}$   $\rightarrow$

$J_{x,1}$

Top

D

$\Delta p_{duy}$

$R_{duy}$

Figure 6b

Recording from test pilot's stabilisation



There is very little point in designing extremely accurate instrumentation when the aircraft cannot be flown along predetermined lines to insure the least number of variables.

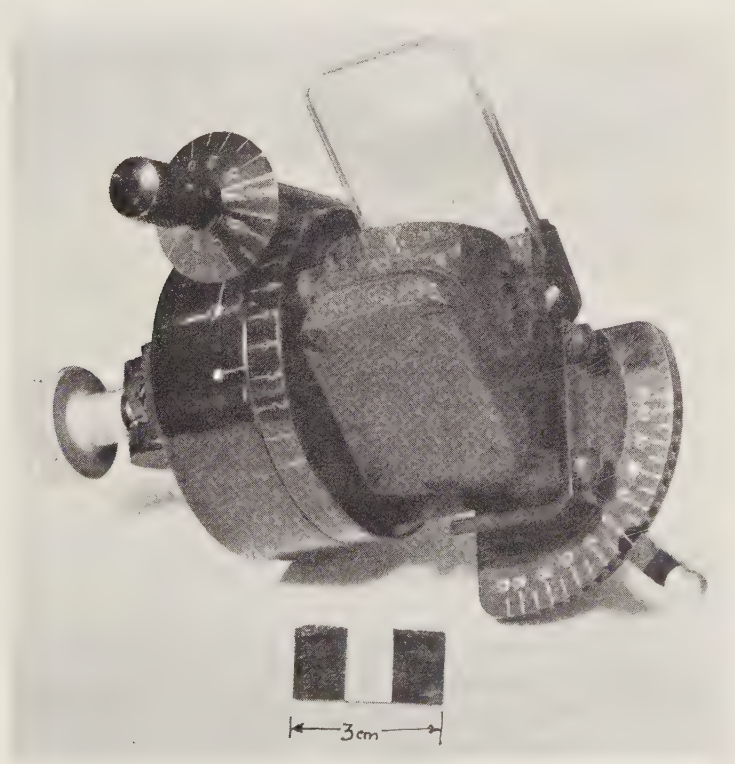
In the ideal system when flown in perfect stabilisation the only trace which should vary should be the one of the parameter under examination (see Figure 6b).

Apart from a "Collimateur" (see Figure 7) the normal instruments of the aircraft serve the test pilot in attaining his high degree of flight accuracy.

#### LOCAL INNOVATIONS

An outstanding achievement of local design has been the reduction in the weight and the simplification of instrumentation system junction boxes (see Figure 8).

By using IBM type blocks we have succeeded in reducing the weight and size of junction boxes by 90%, a factor in instrumentation of paramount importance, especially as the weight of junction boxes has nearly always been an interference factor both from the accessibility and adaptability points of view. Using IBM blocks, hours of soldering are saved and changes between flights can be made to



"Collimateur" sight enabling test pilot accurate flight in  $X$  and  $Y$  axis.

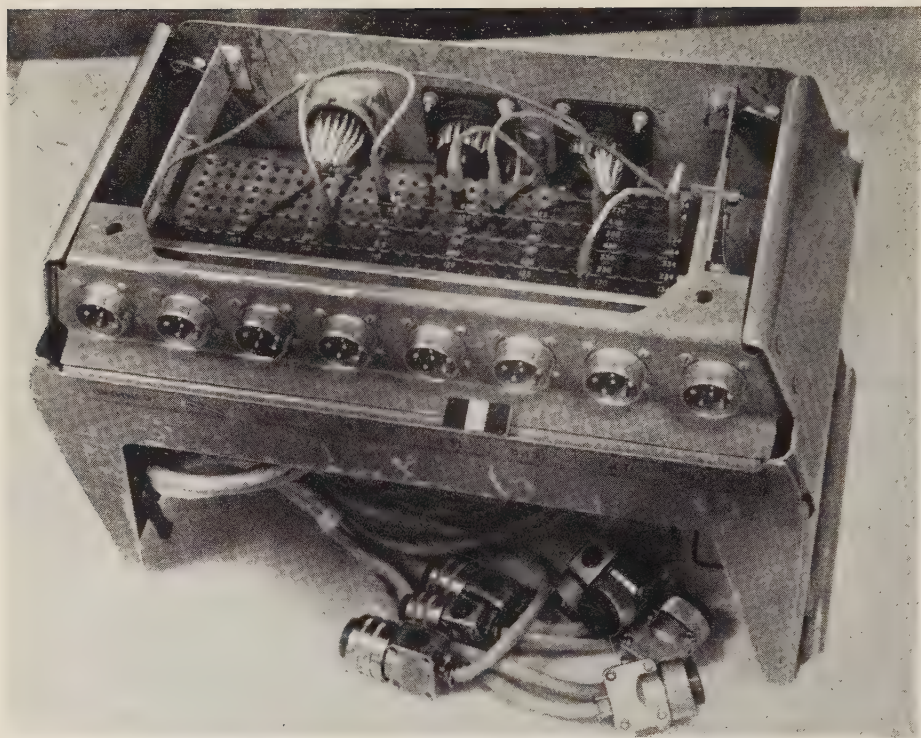


Figure 8  
Junction box using IBM block

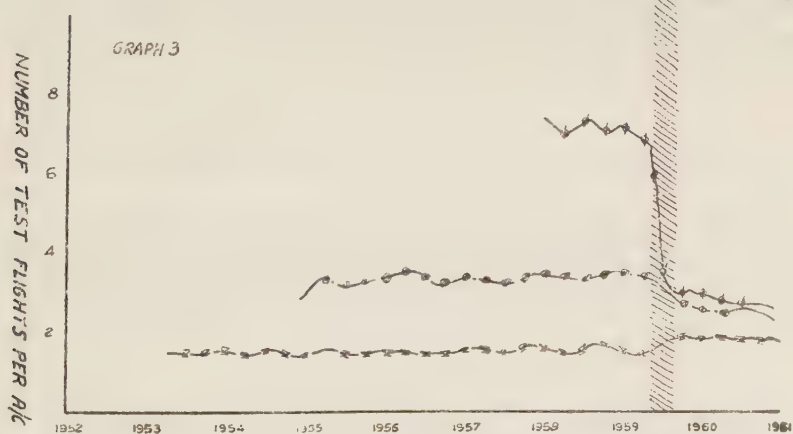
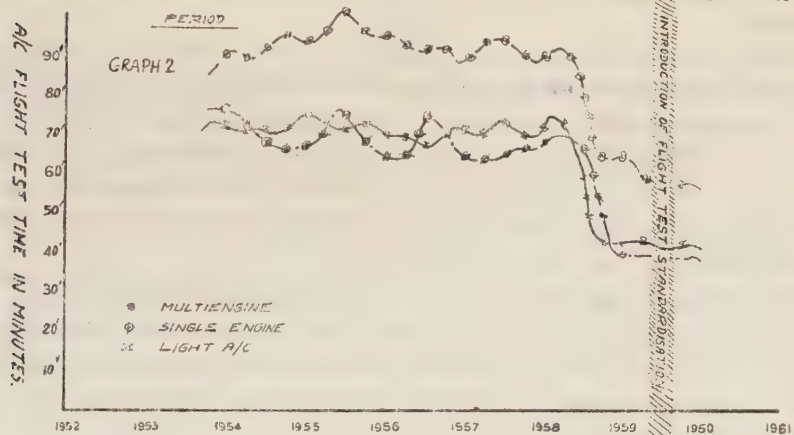
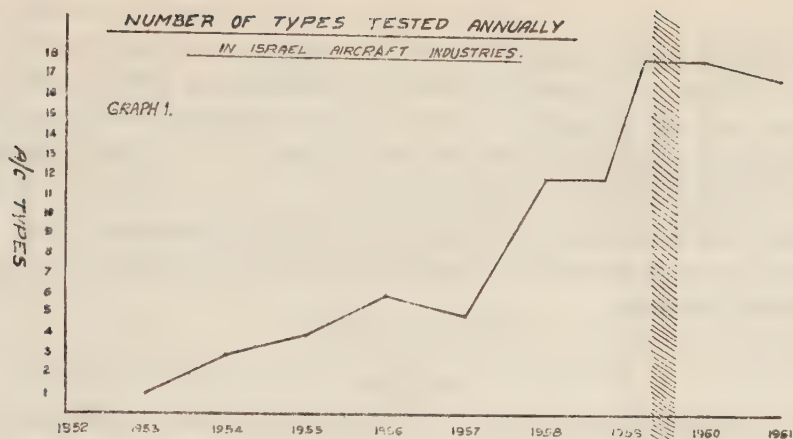
entire circuits within minutes without any changes to microohmic resistances which often are the cause of errors in recording. We expect this method to be adopted soon universally.

#### POSSIBILITIES IN ISRAEL

We have available in this country both the know-how and instrumentation to enable us to undertake a full flight test program of a medium-sized jet transport aircraft.

The instrumentation, recordings and results attained would be acceptable internationally and our results could at any time be compared and cross-checked by any authority as all our methods and equipment are standard.

In addition to basic aircraft design flight test work we can to-day efficiently carry out the testing of any modifications and changes to the laid down requirements of such authorities as the FAA (U.S.A.), ARB (Great Britain) and others.





We can also, by using our equipment and experience, examine existing aircraft and equipment in service with airlines and, after carrying out studies of performance and operational economy based on accurately measured data, advise in the purchasing of new equipment. Finally we can test any new equipment considered for purchase and consult the purchaser how this new equipment will perform in comparison to that which he is thinking of abandoning.

Finally we are available to the Department of Civil Aviation as an arm which can be used to determine the performance of any equipment in use for airworthiness determination purposes.

#### CONCLUSION

Graphs 1, 2 and 3 show the effect of new flight test methods on the efficiency of flight testing.

The Israel Aircraft Industries, the cradle of Israeli flight testing, have during the year 1959-60 test flown ■ types of aircraft and two types of helicopters, reduced by 60% the number of flying hours on most types of standard aircraft tested and have reduced by 30% the time required to carry out certain tests by introducing standard flight test instrumentation. All this with the accompanying reduction cost of flight testing where time in the air constitutes the largest single outlay in foreign currency.

Whatever success is claimed to-day by us, or anyone else for that matter, is only due to team-work. Team-work of the Flight Test Engineer, Test Pilot, Flight test Observer and last but not least the Mechanic, without whose conscientious preparation none of this would be possible since the entire flight would be wasted if the aircraft would have to return due to unserviceability of one of its systems or, for that matter, even any part of the recording system.

# THE EFFECT OF NITROMETHANE ADDITIONS ON THE COMBUSTION OF DROPS OF VARIOUS FUELS UNDER SPHEROIDAL CONDITIONS

L. GROSS-GRONOMSKI

*Faculty of Mechanical Engineering, Technion – Israel Institute of Technology,  
Haifa*

## ABSTRACT

The addition of nitromethane to various fuels can improve the combustion process. This applies, first and foremost, to the decrease of the ignition temperature, and to the reduction of the ignition time lag.

In our experiments, we tested single drops on a hot surface under spheroidal conditions. By means of a movie camera, we were able to determine the changes in the drops during the evaporation and during the combustion. We also measured the evaporation life of the drops at different temperatures.

In our tests, we used standard fuels which are in common use in engines of various types, namely aviation kerosene, diesel fuel, gasoline, and also methyl and ethyl alcohol. For the first three fuels mentioned, the nitromethane additions were small (in the range of about 2 to 5 per cent) because of low solubility. The solubility of nitromethane in alcohols is unlimited, and these mixtures could therefore be tested for all concentrations.

We also tested the effect of alcohol additions to nitromethane (under various concentrations) because of the practical importance of this problem, which, at the same time, is of theoretical interest.

Our results showed that small additions of nitromethane produce a great improvement on the ignition of fuels. A nitromethane addition of from 0.5 to 3 per cent reduced the ignition point and the ignition time lag appreciably under the prevailing experimental conditions. At high nitromethane concentrations in alcohol further additions of nitromethane can, in a certain range, have no further effect on the ignition, and can even produce a negative effect. For alcohol-nitromethane mixtures, the ignition point can be lower than for either constituent alone.

Measurements of the flashpoints (Martens-Pensky method) showed that the addition of nitromethane to fuels (at low concentrations) causes reductions that are not appreciable, although the flashpoints of the mixtures can be lower than those of their constituents alone.

The effect of small nitromethane additions to fuels on the evaporation time is not great, but such additions produce changes in the "kinematics of evaporation" in the sense that they change the evaporation rate of the given drop at certain stages of its evaporation life. This phenomenon seems to be connected with the effect on the ignition.

The results of the tests can be important from the practical point of view for different types of combustion engines using fuel injection.

## I. INTRODUCTION

Various investigators have, for some time, tested the physical and chemical properties of nitromethane<sup>1</sup>. As is well known, it is difficult to use nitromethane as a sole engine fuel, first and foremost because of the great danger of explosion. However,

Received February 1, 1961.

nitromethane can be utilized as one component dissolved in various other liquid fuels for either jet or piston engines. One can also use small quantities of nitromethane as additive to various liquid fuels in order to improve those properties of the fuels that are most important in actual engine operation. Although experiments along this direction have been carried out and a number of patents recorded<sup>1,2,3</sup>, the problem has not yet been sufficiently studied, and, practically speaking, has not as yet emerged from the walls of the laboratory.

The addition of nitromethane to various liquid fuels can improve the combustion process<sup>4</sup>. By means of such additions, it is possible to reduce the ignition point, and also the to reduce the ignition time lag and the combustion time. The ignition problem is closely connected with the problem of drop evaporation. This is, of course, generally true, and not only for nitromethane additions.

The solubility of nitromethane in a number of fuels is small. In our measurements we obtained the following solubilities at 20°C, in percent (by weight):

In diesel fuel:	2.1 percent
In kerosene:	3.2 percent
In gasoline:	5.7 percent

The solubility of nitromethane in ethyl or methyl alcohol is unlimited.

Our measurements showed that the reduction of the fuel flashpoints that are caused by the nitromethane additions are not appreciable, so that, practically speaking, there should be no problem in using such additions (Figure 7).

## II. EXPERIMENTAL SET-UP AND PROCEDURE

In our investigation, we tested single drops on a hot surface. The following variables were measured:

$$\begin{array}{lll} & 1) & \tau = f_1(t_s) ; \\ & 2) & t_{ig} = f_2(\sigma) ; \\ \text{and} & 3) & \Delta\tau_{ig} = f_3(\sigma) ; \end{array}$$

where  $\tau$  is the evaporation time of a single drop in seconds,  $t_s$  is the temperature of the hot surface in °C,  $t_{ig}$  is the minimum hot-surface temperature necessary for ignition  $\sigma$  is the percent (by weight) concentration of nitromethane in the fuel tested, and  $\Delta\tau_{ig}$  is the ignition time lag in seconds.

The tests were carried out as follows: Using a special dropper (Figure 1), drops of variable size can be obtained. The upper end of the dropper is connected with a long rubber tube passing between two hard rubber rollers. By rotating roller 5 (Figure 1), the section of the tube between the dropper and the rollers is lengthened or shortened, thus increasing or reducing the minimum pressure required for releasing a drop. This results in drops of uniform shape and size, irrespective of the height of the liquid column in the dropper.



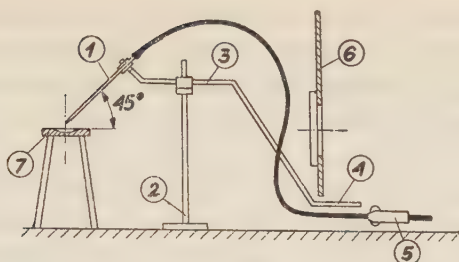


Figure 1

## Drop-release instrument

1—Dropper; 2—Stand; 3—Turning mechanism; 4—Handle; 5—Drop-squeezer; 6—Shielding door; 7—Plate.

The set-up is such that the experiment can be carried out from behind a shield. Thus, the dropper is charged and manipulated from behind the shield by means of a suitable mechanism, so as to prevent heating of the dropper and of the liquid in it (both for reasons of safety and of accuracy), and to return it to its correct position over the center of the plate for each drop. The shield is provided with a steel door having a plexiglass observation window. The set-up is shown in Figure 2.

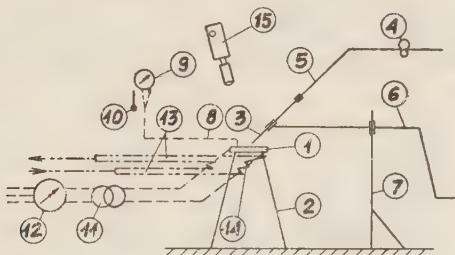


Figure 2

## Experimental set-up

1—Heating plate; 2—Base; 3—Dropper; 4—Pipe rollers; 5—Rubber tube; 6—Handle; 7—Stand; 8—Thermocouple; 9—Galvanometer; 10—Thermometer; 11—Transformer; 12—Variac; 13—Cooling water; 14—Cooling pipe; 15—Movie camera.

The evaporation time  $\tau$  was measured with a stop watch, and also by means of photographs taken with a movie camera. The plate is made of stainless steel. The contact surface must be very smooth, and requires frequent polishing in the course of the experiment. The surface temperature  $t_s$  was measured by means of a chromel-alumel thermocouple attached to the plate with a screw.

The above-described method for studying evaporation has already been used by other investigators<sup>6</sup>.

The movie film (taken at 64 frames per second) shows the changes taking place in the drops while on the hot surface, and also enables us to measure the ignition time lag  $\Delta\tau_{ig}$ .

The evaporation curve  $\tau = f_1(t_s)$  can be divided into three sections (Figure 3). In the first section, where the temperatures are low, an increase in surface temperature  $t_s$  sharply reduces the evaporation time  $\tau$ , up to a certain minimum value. After this minimum, the second section begins, in which an increase in  $t_s$  sharply

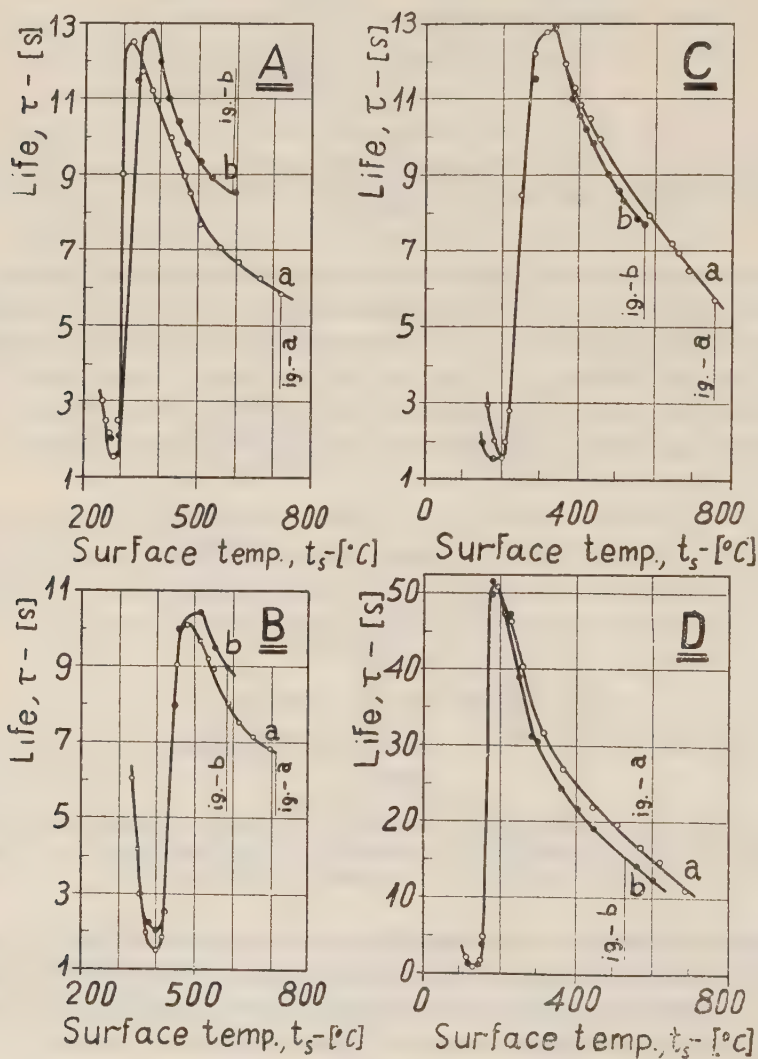


Figure 3

Evaporation time  $\tau$  (seconds) of drop on hot surface as function of surface temperature  $t_s$  (°C)  
(Drop diameter approx. 3 mm.)

Curves A: a—kerosene; b—kerosene with 1.5 per cent nitromethane.

Curves B: a—diesel fuel; b—diesel fuel with 1 per cent nitromethane.

Curves C: a—gasoline; b—gasoline with 3.0 per cent nitromethane.

Curves D: a—methyl alcohol; b—methyl alcohol with 10 per cent nitromethane.

The ignition points are marked on all the curves.

increases  $\tau$  up to a certain maximum value. After this maximum, the third section begins, in which an increase in  $t_s$  again reduces  $\tau$ .

The first section of the curve represents evaporation under non-spheroidal conditions. (The drop loses its spheroidal shape immediately upon coming into contact with the hot surface, and is transformed into a thin film covering the whole hot surface.) In the third section of the curve, the drop retains its spheroidal shape until it is completely evaporated, which represents evaporation under spheroidal conditions<sup>4</sup>. The second section represents a transition between the conditions prevailing in the first and the third sections.

In our experimental method, the values of the ignition temperature represent the temperatures  $t_{ig}$  of the hot surfaces upon which the drop is placed. The experiment was carried out under ordinary ambient temperature and pressure conditions. The measurements of the ignition time lag  $\Delta\tau_{ig}$  were carried out by means of the same method and under the same conditions.

In additional experiments, the flash points of methyl alcohol, of ethyl alcohol, and of kerosene, with added nitromethane were measured. These measurements were carried out by means of the Martens-Pensky apparatus, with initial cooling.

### III. RESULTS OF THE MEASUREMENTS

Figure 3 shows the results of the evaporation-time measurements (single drops on a hot surface) for the following fuels:

- Curves A: Aviation kerosene
- Curves B: Diesel fuel
- Curves C: Commerical automobile gasoline
- Curves D: Methyl alcohol (99 percent)

The curves "a" and "b" represent the various fuels without and with nitromethane additions respectively. The following percent (by weight) nitromethane additions were used:

- 1.5 percent in kerosene
- 1 percent in diesel fuel
- 3 percent in gasoline
- 10 percent in methyl alcohol

On each of the above curves, the ignition temperature (in °C) is also marked. The diameter of the drops was approximately 3 mm.

The curves of Figure 3 show that the effect of the nitromethane additions on the evaporation time is not great. The additions to kerosene (A) and to diesel fuel (B) increase the evaporation time  $\tau$  in the spherical range, while they decrease  $\tau$  for gasoline (C) and methyl alcohol (D). In all cases, the nitromethane addition appreciably reduces the ignition temperature (Figure 3).



Figure 4 presents results of our measurements of the ignition temperature  $t_{ig}$  as a function of the nitromethane concentration  $\sigma$  in industrial ethyl alcohol – curve “a”, and in methyl alcohol (99% grade) – curve “b”. The curves show that an increase of the nitromethane concentration in these alcohols reduces the ignition temperature  $t_{ig}$  only within a certain range, up to  $\sigma \approx 25$  percent (by weight) in our experiments. For  $\sigma > 25$  percent, further increases in  $\sigma$  produce either no appreciable changes at all, or a slight increase in  $t_{ig}$ . It is characteristic that, for  $\sigma$  close to 100 percent, a further increase in  $\sigma$  increases  $t_{ig}$ . This means that, if we add methyl or ethyl alcohol to nitromethane, we can in this way also reduce the ignition temperature  $t_{ig}$ .

We thus see from Figure 4 that it is possible to obtain

$$(t_{ig})_{F1+F2} < (t_{ig})_{F1}$$

and also

$$(t_{ig})_{F1+F2} < (t_{ig})_{F2}$$

where  $(t_{ig})_{F1}$  is the ignition temperature for the first fuel,

$(t_{ig})_{F2}$  is the ignition temperature for the second fuel,

and  $(t_{ig})_{F1+F2}$  is the ignition temperature for the mixture of the two fuels.

In other words, the ignition temperature of fuel mixtures can be lower than the ignition temperature of each component separately.

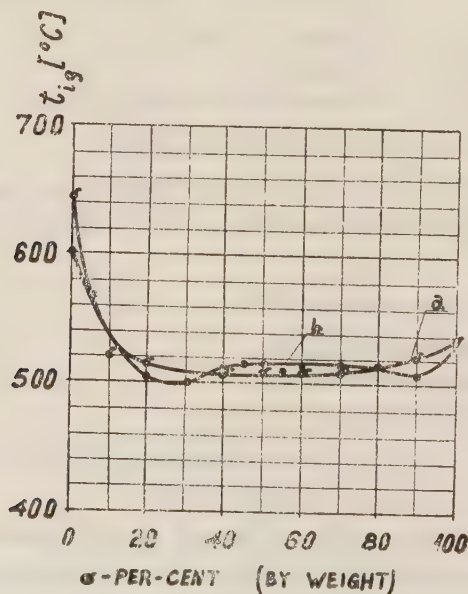


Figure 4

Ignition temperature  $t_{ig}$  (°C) as function of nitromethane concentration in per cent (by weight) in ethyl alcohol—curve “a”, and in methyl alcohol—curve “b”.

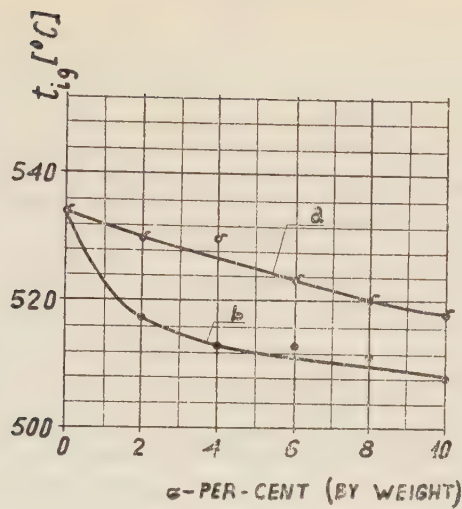


Figure 5  
Ignition temperature  $t_{ig}$  (°C) as function of ethyl alcohol concentration  $\sigma$ —curve "a", and methyl alcohol concentration  $\sigma$ —curve "b", in per cent (by weight) in nitromethane.

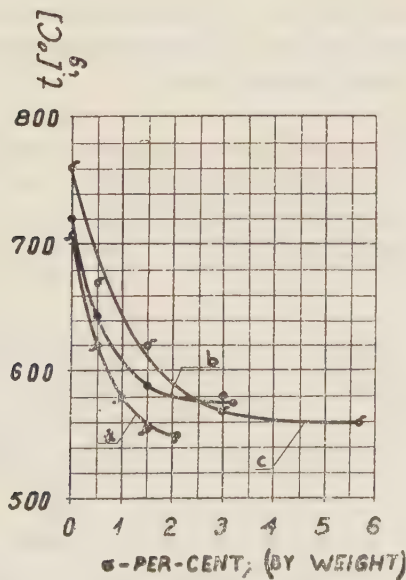


Figure 6  
Ignition temperature  $t_{ig}$  (°C) as function of nitromethane concentration  $\sigma$  in per cent (by weight) in diesel fuel—curve "a", kerosene—curve "b", and gasoline—curve "c".

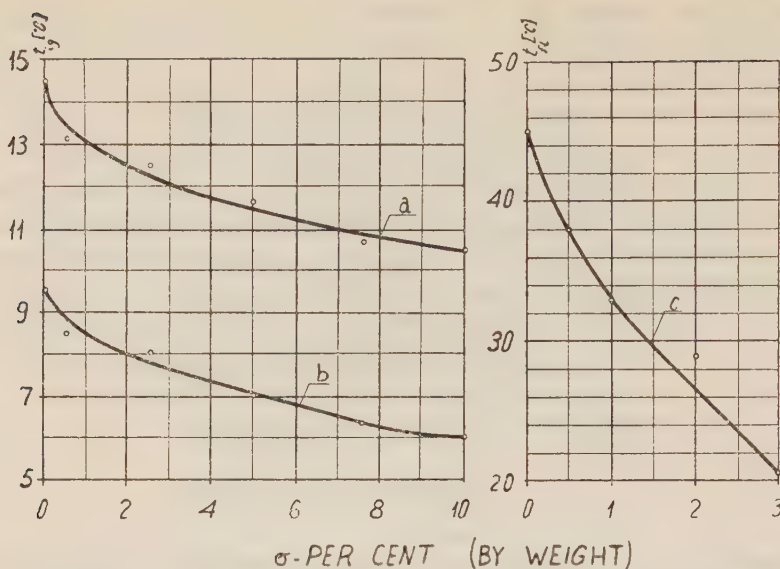


Figure 7

Flash point ( $^{\circ}\text{C}$ ) of ethyl alcohol—curve “a”, methyl alcohol—curve “b”, and kerosene (aviation)—curve “c” as function of nitromethane concentration  $\sigma$  in per cent (by weight).

It might be worth nothing that Barrère and Moutet<sup>5</sup> have pointed out the possibility of obtaining an ignition time lag of a fuel mixture which is smaller than the corresponding lag for each individual component.

Figure 5 presents results of our measurements for additions of ethyl alcohol (industrial)—curve “a”, and additions of methyl alcohol (99 percent grade)—curve “b”, to nitromethane. The curves show that additions of these alcohols reduce the ignition temperature  $t_{ig}$  of nitromethane. This phenomenon can obviously be of practical importance.

Figure 6 shows results of our measurements for additions of nitromethane (in small quantities) to diesel fuel—curve “a”, to aviation kerosene—curve “b”, and to commercial gasoline—curve “c”. The curves show that the nitromethane addition has an appreciable effect on the ignition temperatures  $t_{ig}$  of these fuels.

Table I shows the effect of nitromethane additions on the ignition time lag  $\Delta\tau_{ig}$  of kerosene, as found in our measurements carried out by means of a movie camera photographing 64 frames per second. The temperature of the hot surface had to be adjusted according to the respective ignition temperature  $t_{ig}$  for the given mixture. Table I shows results for two different values of hot-surface temperature.



TABLE I  
*Ignition time lag  $\Delta\tau_{ig}$  of single drops on a hot surface of temperature  $t_s$*

Nitromethane concentration $\sigma$ per cent (by weight) in aviation kerosene	0	0.5	1.0	3.0
Temperature of the hot surface $t_s$ ( $^{\circ}\text{C}$ )	675	675	552	552
Ignition time lag $\Delta\tau_{ig}$ (seconds)	0.36	0.09	0.30	0.17

Figure 7 shows the effect of nitromethane additions on the flashpoint of ethyl alcohol — curve “a”, methyl alcohol — curve “b”, and kerosene — curve “c”. The additions produce a reduction of the flashpoint.

By means of movie-camera photographs of single drops on the hot surface, the changes taking place in the drop during evaporation, ignition, and combustion can be studied. For the above-mentioned fuels used in this investigation, and also for some other fuels, we have established the fact that the drop at certain moments experiences an appreciable increase in diameter, while, at other moments, the drop diameter suddenly shrinks. This change in the drop diameter is liable to appear at the beginning, and also several times afterwards in the course of the evaporation and combustion process. For diesel fuel, these changes in the drop diameter are especially pronounced. When nitromethane additions are used, this phenomenon appears to an even greater extent.

These changes undoubtedly influence the evaporation and ignition processes and the combustion time, but it is difficult to determine any systematic correlation. It seems that the phenomenon might be of importance in trying to explain the effects of additions to fuels on their evaporation and ignition, and also the connection between the evaporation and ignition of drops of various fuels.

#### IV. CONCLUSIONS

The addition of nitromethane to various fuels (diesel fuel, kerosene, gasoline, methyl and ethyl alcohol) influences their evaporation and ignition processes.

##### 1. Effect of nitromethane additions on the evaporation of drops.

a. For some fuels (diesel fuel and kerosene), the nitromethane additions cause an increase in the evaporation time, while, for other fuels (gasoline and methyl alcohol), the evaporation time is decreased. The effect, however, is not appreciable, and, in our tests, amounted to approximately 10 percent.

b. During the evaporation process, vapours (and also gases resulting from possible decomposition) can collect inside the drop. The drop expands up to a certain size, whereupon it can burst, with the consequent release of the vapours or gases. This produces a new drop of smaller diameter taking the place of the previous drop. The new drop again expands, and this sequence can be repeated several times until the end of the evaporation process. This phenomenon is very pronounced for diesel fuel, and becomes even stronger with nitromethane additions.

2. Effect of nitromethane additions on the ignition temperature  $t_{ig}$  and on the ignition time lag  $\Delta\tau_{ig}$ .

a. Small concentrations of nitromethane cause a great decrease of  $t_{ig}$ , especially for diesel fuel, kerosene and gasoline. Thus, 0.5 percent (by weight) of nitromethane in kerosene or in diesel fuel reduces  $t_{ig}$  by about 100°C. In order to obtain such a reduction in alcohols, approximately 10 percent of nitromethane is required for ethyl alcohol, and approximately 20 percent in methyl alcohol.

b. The ignition temperature  $t_{ig}$  for a mixture of two fuels can be lower than that of each fuel alone. Thus, the  $t_{ig}$  of ethyl alcohol and that of nitromethane were, in our tests, found to be 640°C and 535°C respectively, whereas the minimum  $t_{ig}$  for a mixture of these two fuels was 500°C.

c. The ignition time lag  $\Delta\tau_{ig}$  of the various fuels tested is reduced by the addition of nitromethane. Thus, a 0.5 percent addition of nitromethane reduces  $\Delta\tau_{ig}$  of kerosene by a factor of 4.

3. The addition of nitromethane to various fuels reduces their flashpoint, but by a relatively small amount. Thus, a 0.5 percent addition of nitromethane to kerosene reduces its flashpoint by 7°C. It is characteristic that the flashpoint of a mixture of two fuels also can be lower than that of each fuel alone. This has been verified for mixtures of nitromethane with methyl and ethyl alcohol and also with kerosene.

4. The addition of methyl or ethyl alcohol to nitromethane of up to about 20 percent reduces its ignition temperature  $t_{ig}$  by as much as 30°C.

#### V. ACKNOWLEDGMENT

The above-described tests are part of the research carried out at the Mechanical Engineering Faculty of the Technion with the help of the Fohs Fund. The author wishes to express his thanks to Prof. D. Ginzburg and Prof. S. Frank for their help in organizing the research, and also to Miss A. Kerner and Messrs. D. Cohen and A. Huberman, who helped in constructing the test equipment and with the measurements.

#### REFERENCES

1. MAKOVKY, A. AND LENJI, L., 1958, *Chemical Reviews*, **58**, 4.
2. STARKMANN, E. S., 1954, *Chem. Eng. News*, **32**, 4474.
3. SABLINA, Z. A. AND GURIEEV, A. A., 1959, *Prisadki k motornym toplivam* (in Russian), *Gos-  
techizdat*, Moscow.
4. GROSS-GRONOMSKI, L., 1959-60, *Israel Institute of Technology - Reports*.
5. BARRERE, M. AND MOUTET, A., 1956, *Selected Combustion Problems*, II.
6. TAMURA, Z. AND TANASAWA, Y., 1958, *Seventh International Combustion Symposium*, London.

# STRUCTURE, VARIATIONS AND MEASUREMENTS OF THE EARTH'S IONOSPHERE AND EXOSPHERE

COLMAN ALTMAN

*Department of Physics, Technion – Israel Institute of Technology, Haifa*

## ABSTRACT

The extensive use of high altitude rockets during, and subsequent to, the IGY period has yielded much useful information about the structure of the *E* and *F* layers of the ionosphere. Measurements in earth satellites and space probes have revealed the inner and outer radiation belt, and also ring-currents encircling the earth at distances of many earth radii. These measurements have supplemented and enlarged the existing body of knowledge of the inner ionosphere (*D*, *E* and *F* regions) acquired primarily by ionosonde techniques and geomagnetic measurements, and also of the outer ionosphere (or exosphere), in which atmospheric "whistlers" played a pioneer role. Our present state of knowledge is surveyed and work being conducted in this field by the Ionospheric Physics group in the Technion is briefly described.

## INTRODUCTION

The movement of the earth and its dipole magnetic field through a very hot hydrogen gas — an extension of the sun's coronal atmosphere — and the consequent conduction of heat into the earth's atmosphere plays an important role in the thermal economy of the high atmosphere. The 'solar wind' consisting of neutral clouds of ionized hydrogen is effective in sweeping away the extension of the earth's magnetic field at a distance of some 5–8 earth radii on the sunlit side of the earth and creating a magnetic discontinuity in part of the auroral zones into which high speed protons are funnelled directly from the solar wind. In addition, high speed protons and electrons which leak through the magnetic barrier are trapped in the geomagnetic field and give rise to the outer Van Allen radiation belt. This belt, together with the direct contribution of solar protons in the near polar regions, heat the auroral atmosphere above 100 km height and generate wind circulations which transport heat to the equatorial and temperate zone ionospheres, and heat the thermosphere of the earth to over 1000°K.

The ultraviolet radiation of the sun and soft X-rays ionize the *D*-, *E*- and *F*-layers of the ionosphere, and the interplay of production, collision and recombination rates of ion pairs generate the variation of electron densities in the ionosphere which determine the conditions of electromagnetic wave propagation. Diurnal tides in the ionosphere generated by solar heating institute world-wide current systems in the *E*-layer which are manifested in the diurnal geomagnetic variation.



At the base of the thermosphere water-vapour and methane are decomposed by solar ultraviolet radiation and by upward diffusion the neutral hydrogen atoms from a "telluric hydrogen corona". Thermal protons are generated by charge-exchange reactions and their relative abundance gradually increases until they become the main component at a height of one earth radius.

The Van Allen radiations, formed by trapped solar emissions, although important in their effects, form a negligible proportion of the total ion content at these heights.

Each component — the neutral hydrogen atoms, the thermal protons and the energetic Van Allen radiations — is manifested by its distinctive effects. Some effects and proposed measurements are discussed.

#### THE INTERPLANETARY MEDIUM

The medium in which the earth's orbit is situated is determined by conditions prevailing in the sun, constituting a distant extension of the solar corona. At a height of 50,000 km above the solar surface, the corona acquires a kinetic temperature of one to two million degrees, consisting mainly of a completely ionized hydrogen plasma. The thermal conductivity of a plasma is proportional roughly to  $T^{5/2}$  and because of the high conductivity attained, the corona is comparatively isothermal over large radial distances. At the earth's orbit Chapman<sup>1,2</sup> finds that this plasma has a temperature between 50,000°K and 200,000°K (corresponding to 6–25 ev protons), using a model of hydrostatic equilibrium in which  $T = 10^6$ °K for the corona in the sun's vicinity. Using higher values of coronal temperature —  $2 \times 10^6$ °K — which certainly exists in active regions of the corona, Parker<sup>3</sup> has found that the hydrostatic equation is not valid, yielding finite values of density at an infinite distance, and concludes that the corona is continually expanding outwards, as a "solar wind". Using an equation of hydrodynamic equilibrium Parker finds solar wind velocities of the order of 500–1500 km/sec at the earth's orbit (up to 10 kev proton energies).

Experimental observations support these conclusions. Biermann<sup>4,5</sup> has found that extreme accelerations of comet tails can only be explained by corpuscular streams from the sun of densities between 50 and  $10^4$  particles/cm<sup>3</sup> and velocities of some  $10^3$  km/sec at the earth's orbit. Measurements on the zodiacal light<sup>6</sup> have yielded electron densities at the earth's orbit of 50– $10^4$  electrons/cm<sup>3</sup>. The figures vary from low values at sunspot minimum to high values in periods of intense solar activity.

Finally we should mention the close correlation between solar flares and geomagnetic activity on the earth 24–40 hours later, which clearly indicate that the ionized clouds emitted by the sun travel with radial velocities between 1000–1500 km/sec.

To summarize, the picture which emerges is roughly as follows. The earth's orbit is immersed in a hot solar ionized gas of temperature between 50,000°K to 200,000°K with a density of several hundred protons/cm<sup>3</sup> through which a solar wind of some-

what lower density frequently blows, tending to carry with it the stationary interplanetary gas. At times of solar activity, the solar wind takes the form of dense, high velocity ionized clouds. Because of its relatively high kinetic energy density the ionized solar wind will tend to sweep away all transverse magnetic fields in its path, leaving behind it radial magnetic field lines, which slowly spiral outwards because of the sun's rotation<sup>3</sup>.

#### THE INTERACTION BETWEEN THE SOLAR WIND AND THE EARTH'S MAGNETIC FIELD

Equating the magnetic energy density  $B^2/8\pi$  of the earth's dipole field with the kinetic energy density  $\frac{1}{2} n m v^2$ , we find equality at radial distances of 5–8 earth radii on the sunlit side. We may thus expect the earth's dipole field to be swept away at larger radial distances, whereas at small distances the solar wind will be excluded. We thus define an outer limit to the outer radiation belt. If penetration by high speed protons occurs, these particles will be trapped and constrained to spiral back and forth between magnetic mirror points along lines of magnetic field. The outer limit of the geomagnetic field will correspond to field lines which meet the earth's surface at geomagnetic latitudes of  $65^\circ$ – $70^\circ$ , i.e. in the auroral zones. Furthermore, at somewhat higher latitudes (towards the polar regions) clouds of solar protons will frequently pour into the earth's atmosphere on the sunlit side of the earth. Such clouds probably generate by travelling-wave-tube mechanisms<sup>7</sup> or cyclotron radiation<sup>8</sup> the audio frequency electromagnetic emissions such as "dawn-chorus", hiss, etc., which in high latitudes are regularly received in the early morning and in times of geomagnetic activity<sup>7,9,10</sup>.

On the night-side of the earth the magnetic field lines are "shielded" from the solar wind, and hence will extend outwards considerably, some investigators believing up to one hundred earth radii.

A further postulated effect of the solar wind interaction with the geomagnetic field is that electrons and protons being oppositely deflected will set up electrostatic forces which will drive "ring currents" to girdle the earth<sup>12</sup>. Magnetic measurements in the first Soviet moon rocket<sup>13</sup> revealed such a westward flowing ring current at a height of 22,000 km from the center of the earth (inside the outer Van Allen belt), and later measurements<sup>14</sup> in Explorer VI revealed an additional (or perhaps displaced) ring current system of some five million amperes girdling the earth at a radial distance of 40,000 km.

#### THE RADIATION BELTS AND THE EARTH'S EXOSPHERE

The outer radiation belt particles are engendered by penetration of electrons and protons having an energy peak probably near 10 kev. Once captured, they spiral back and forth along lines of magnetic force, their pitch angle  $\theta$  (angle between guiding line of force and direction of velocity vector) being related to the magnetic intensity,  $B$ , by the relation

$B/\sin^2 \theta = \text{const}$ , and the mirror point,  $M$ , being defined by  $\theta_m = \pi/2$ , and  $B_m = B/\sin^2 \theta$ . The steeper(smaller) the initial angle,  $\theta$ , the closer to the earth's surface will the mirror point be, and the smaller the survival time of such a particle. Hence a non-isotropic distribution is soon set up in which large pitch angles are favored. Energetic particles are lost to the medium following charge-exchange collisions with neutral hydrogen atoms in the belt. The collision rate for such collisions has been shown to be constant for energies between 100 ev and 20 kev above which the collision rate falls rapidly<sup>15</sup>. We may thus expect the outer Van Allen belt radiation to contain protons with energies well above 20 kev, and according to Stuart<sup>16</sup> with energies mainly above 50 kev. The electron component has a much longer lifetime and is the main radiation constituent of the outer belt, concentrating in the energy range 20–100 kev<sup>17</sup>. Nevertheless their absolute abundance is very low, roughly  $10^{-1}$  electrons/cm<sup>3</sup> with energies greater than 20 kev<sup>18</sup>.

The generation of the outer belt radiation in the solar wind has been clearly demonstrated. Measurements of the drag on Sputnik III<sup>19</sup> (which passed regularly through the outer belt in the auroral zone) showed a 27-day cycle and also two large increases in drag, each time some 36 hours after major flares in the sun, and in step with geomagnetic storms. Vanguard I, on the other hand, which passed through the inner radiation belt showed little such effect. This lent support to the theory that the inner belt originates primarily in the decay of neutrons in the cosmic ray albedo, which would account too for the relative hardness of its radiation. More convincing were the results of the Pioneer IV flight<sup>18</sup>, launched six days after a strong magnetic storm, which revealed radiation intensities about 100 times higher than previous measurements by Pioneer III and by Mechta, the Soviet moon rocket, during magnetically quiet periods, indicating clearly injection of corpuscular radiation by ionized solar clouds.

#### THE THERMOSPHERE AND HETEROSPHERE OF THE EARTH

The temperature of the atmosphere reaches a minimum (about 150°K) at a height of some 85 km in the so-called mesopause, and above this the temperature gradient is positive—defining the earth's thermosphere. Nicolet and Chapman consider that the thermosphere continues (i.e. that its temperature gradient is positive) until it finally merges with the hot solar plasma beyond the radiation belts<sup>20</sup>. Rocket measurements however, based on pressure-altitude variations<sup>21,22</sup>, indicate that the atmosphere becomes roughly isothermal close to 200 km with temperatures varying from 1000°K–2000°K depending on local time and season. At an altitude of about 550 km the mean free path in a horizontal direction of the neutral atmospheric components equals the scale height, so that neutral particles travelling vertically with sufficient energy are able to leave the earth's field without further collisions. This level is the base of the neutral particle exosphere, in which temperature is no longer well defined, and in which usual gas-kinetic relationships no longer hold<sup>23</sup>.



Above the mesopause solar ultraviolet radiation is strongly absorbed, dissociation of  $O_2$  and to a lesser extent  $N_2$  resulting. Because of the low recombination rates, which decrease with altitude, we find that the concentration of atomic oxygen increases and it becomes the main atmospheric constituent at a height of several hundred kilometres, although at 250 km molecular nitrogen,  $N_2$ , is probably still more abundant<sup>24</sup>.

Because at these altitudes vertical diffusion is much more important than mixing due to wind circulations, the density of each constituent tends to fall off with altitude according to its own scale height  $H = RT/Mg$  (i.e. diffusive equilibrium is established) and the composition of the atmosphere changes constantly with height, lighter elements gradually predominating. This region is thus called the earth's heterosphere. The decomposition of water vapour and methane just below the mesopause<sup>20</sup> liberates neutral atomic hydrogen which, because of its large scale height (even though scale-height is not strictly defined in an exosphere), replaces oxygen as the main neutral atmospheric constituent above 1200 km<sup>25</sup>, and forms a "telluric hydrogen corona" at greater heights. The presence of this vast hydrogen cloud or corona encompassing the earth (with particle densities of  $10^5$  particles/cm<sup>3</sup> at 200 km and  $3 \times 10^4$  particles/cm<sup>3</sup> at 1200 km<sup>25</sup>) has been demonstrated by rocket measurements of the night sky<sup>26</sup> which was found to be aglow with diffuse Lyman- $\alpha$  emission (resonantly absorbed and re-radiated from the Lyman- $\alpha$  flux of hydrogen in space), and also by the shape of the narrow absorption strip in the centre of the solar Lyman- $\alpha$  emission line<sup>27</sup>.

The atmospheric densities at heights ranging from 100 km to 700 km have been measured by calculation of drag on satellites<sup>19</sup>, and directly by rocket-borne ionization gauges<sup>21</sup>. These measurements were interpreted (for instance by Jastrow<sup>28</sup>) as indicating the simultaneous occurrence of temperatures of 2000°K in the auroral zones and 1000°K in the temperate-equatorial zones at heights of 200 km, corresponding pressures in the auroral zones being five times higher than in the temperate. Johnson later demonstrated that such pressure and temperature differences were dynamically inconceivable at these heights<sup>29</sup>. For even under extreme anticyclonic conditions (which apparently do not exist at this altitude) the constant pressure surface would be 12 km higher over the poles than over the equator. Additional pressure differences must introduce a wind circulation from pole to equator. Now heating of the auroral atmosphere by energetic radiations in the outer Van Allen belt and solar corpuscular streams spiralling in along field lines outside of the outer belt undoubtedly does occur. Heating would occur mainly at 100 km altitude tailing off towards 200 km as evidenced by the height distribution of auroral displays. We may thus assume (with Johnson<sup>29</sup>) a circulation in which high wind velocities would be set up at 200 km and above (dropping with a steady gradient to zero at 100 km), which would transport heat from the polar to the equatorial atmosphere and here downwards from the observed temperature of 1500°K at 200 km to 200°K in the mesopause ( $\sim 100$  km). Assuming a wind velocity of 150 km/sec at 200 km

and above we may show that sufficient heat would be transported to supply all the heat requirements of the temperate and equatorial ionospheres. Further a circulation of this type would be maintained by a constant pressure surface only 8 km higher at the pole than at the equator at 200 km. Adding this to the maximum 12 km height difference due to conceivable limiting anticyclonic circulations, and bearing in mind that the scale height at this level is some 50 km, we find that a 50% pressure difference (which could be engendered by a 100°K temperature difference only between poles and equator) would set up a wind circulation which would cover the thermal budget of the entire ionosphere. It would appear now that the extreme pressure and temperature differences reported stem from the fact that the auroral measurements were performed during a more active phase of the sunspot cycle than the corresponding temperate zone measurements, a factor which presumably had a considerable influence.

At higher altitudes (at 400 km say) the auroral pressures might indeed exceed the temperate values by a factor of five, since the viscous forces in a given wind velocity gradient are independent of pressure, and so become a dominant factor at higher altitudes.

To conclude this section it may be remarked that measurements of wind velocities above 90 km by radio observations of drifting meteor trails<sup>30</sup> have shown that above 105 km winds blow from pole to equator all year round, summer velocities reaching 40 metres/sec at 105 km, and the velocity gradient is always positive above 90 km. This seems to be clear support for Johnson's model.

#### THE IONOSPHERE OF THE EARTH

The ionosphere is formally considered to start where the ionization density is sufficiently high to affect radio propagation, and this is just below the mesopause ( $\sim 80$  km). For many years the ionosphere was investigated by ionosonde techniques only, which yielded fairly accurate height versus electron-density profiles up to the level of maximum ionization. These profiles tended to show distinct layers of ionization termed the *D*, *E* and *F* layers according to the height at which they occurred. However, recent rocket measurements have shown that frequently "ledges" (where the density gradient is positive but small) tend to form between layers rather than "valleys". In view of this a formal definition has been adopted in which the *D*-layer is that part of the ionosphere below 90 km, the *E*-layer is situated between 90 and 160 km, and above 160 km the *F* layer is located.

The *F*-layer is formed primarily by the ionization of atomic oxygen by the entire spectral range of solar radiation from 200–850 Å,<sup>32</sup> so that ionized atomic oxygen is already the main ionic component of the atmosphere at 200 km, as verified by rocket measurements<sup>33</sup>. The *E*-layer is formed mainly by soft X-rays in the 10–100 Å range<sup>32</sup> and the *D*-layer by harder X-rays ( $\lambda < 10$  Å) and, proceeding to lower altitudes by Lyman- $\alpha$  and by cosmic radiation<sup>34</sup>. It should be remembered,

however, that these ionospheric layers are predominantly neutral regions. The ion to neutral component ratio at the *E* and *F* layer peaks are about  $10^{-7}$  and  $10^{-4}$  respectively.

Above the *F*-layer peak recombination gradually becomes unimportant and a diffusive equilibrium is set up for the ionic component too. Now hydrogen ions are formed by charge-exchange between hydrogen atoms and oxygen ions, the ionization potential being almost identical for the two<sup>35</sup>. Charge exchange collisions will be important only up to the base of the exosphere, and since the reaction can proceed equally well in both directions the neutral and ionized oxygen-hydrogen ratios here will be equal, and relative ionic scale heights will determine the subsequent ionic distribution higher up. We thus find that at 1600 km protons become the main ionic component<sup>25</sup>.

Now the scale height of a plasma is determined by a temperature equal to the sum of the ionic and electronic temperatures, so that the ionized hydrogen scale height is about twice that of the neutral hydrogen. (Note that because of the large cross-section for ion-ion collisions, the ion-ion mean free path is nowhere larger than the scale height, and the ionized hydrogen component is nowhere in an ionic exosphere, but instead governed by hydrostatic equilibrium). A second factor which increases the scale height of the ionic component is the magnetic field. Because of the high conductivity of the ionosphere magnetic field lines are "anchored" in the lower ionosphere, and since the latter rotates together with the earth, so too do the field lines higher up and together with them the whole ion-electron plasma. The ions are thus compelled to maintain a constant angular velocity (rather than angular momentum) and the resulting centrifugal force further increases the scale height. The net result is that at a height of one earth radius protons become more numerous than neutral hydrogen, their concentration decreasing very slowly with height. We thus find that the inner radiation belt is populated primarily by neutral and ionized thermal hydrogen and the outer belt primarily by thermal protons and electrons.

The presence of this ionized hydrogen plasma, or protonosphere as Johnson<sup>25</sup> has called it, surrounding the earth to large radial distances was discovered<sup>36</sup> and investigated by means of "whistlers". In general the ionospheric layers are a reflecting medium for all frequencies below about 5 Mc/s. However, at very low (audio) frequencies the ionosphere is transparent to the extraordinary component of electromagnetic waves which travel in the direction of magnetic field lines. Further, the field lines have a focussing action on the wave which will follow the magnetic lines from one hemisphere to the other and then back again. Now electromagnetic energy in the audio region is propagated by lightning discharges, and by measuring the time delay of each frequency component to make the round trip along field lines from hemisphere to hemisphere, the electron density at the top of the magnetic



path may be estimated. In this fashion Storey<sup>36</sup> found unexpectedly high electron densities of several hundred per  $\text{cm}^3$  at distances of several earth radii, and since then the total distribution has been estimated by this method<sup>37</sup>.

It may be mentioned that the magnetic field line through Haifa reaches a height of 2000 km above the magnetic equator, and it is hoped that whistler measurements being conducted by the Ionospheric Physics group of the Technion will yield information of thermal ion concentration at the base of the inner radiation belt and its correlation with electron densities at the  $F$  layer peak (as obtained by ionosonde techniques).

The total ion content of the ionosphere has been calculated by measuring the Faraday effect (the rotation of the plane of polarisation of an electromagnetic wave in a magnetoionic medium) for radio frequency signals transmitted from satellites<sup>38</sup>. These measurements have verified that 2 to 3 times as many electrons may be found above the  $F$  layer peak as below.

#### CONCLUSION

The nature and generation of the Van Allen radiations, the thermal whistler medium or protonosphere, and the telluric neutral hydrogen corona have been described. A great deal concerning the role of the solar wind and the extended solar corona is not clear as yet, and their clarification awaits the more extensive measurements of the future earth satellites.

#### REFERENCES

1. CHAPMAN, S., 1957, Notes on the solar corona and the terrestrial atmosphere, *Smithsonian Contrb. to Astrophys.*, **2**, 1.
2. CHAPMAN, S., 1960, The thermosphere—the earth's outermost atmosphere, *Physics of the Upper Atmosphere*, ed. J. A. Ratcliffe, Academic Press, New York.
3. PARKER, E., 1959, Extension of the solar corona into interplanetary space, *J. Geophys. Res.*, **64**, 1675.
4. BIERMANN, L., 1953, Physical processes in comet tails and their relation to solar activity, *Mem. Soc. Roy. Sci. Liege* [4], **13**, 291.
5. BIERMANN, L., 1957, Solar corpuscular radiation in the interplanetary gas, *Observatory*, **77**, 109.
6. BLACKWELL, D. E., 1957, The zodiacal light and the nature of the interplanetary gas, *Observatory*, **77**, 187.
7. GALLET, R. M., 1959, The very low frequency emissions generated in the earth's exosphere, *Proc. I.R.E.*, **47**, 211.
8. MAC ARTHUR, J. W., 1959, Theory of the origin of the very low frequency radio emissions from the earth's exosphere, *Phys. Rev. Letters*, **2**, 491.
9. ELLIS, G. R. A., 1957, Low frequency radio emission from the aurora, *J. Atmos. Terr. Phys.*, **10**, 302.



10. ELLIS, G. R. A., 1959, Low frequency electromagnetic radiation associated with geomagnetic disturbances, *Planet and Space Sci.*, **1**, 4.
11. BEARD, D. B., 1960, The interaction of the terrestrial magnetic field with the solar corpuscular radiation, *J. Geophys. Res.*, **65**, 3559.
12. CHAPMAN, S. AND FERRARO, V. C. A., 1931, A new theory of magnetic storms, *Terr. Mag. and Atmos. Elect.*, **36**, 77 and 171.
13. DOLGINOV, S. SH. AND PUSHKOV, N. V., 1960, Magnetic field of the outer corpuscular region, *Proc. Moscow Cosmic Ray Conference*, **3**, 30.
14. SMITH, E. J., COLEMAN, P. J., JUDGE, D. L. AND SONETT, C. P., 1960, Characteristics of the extraterrestrial current system, *J. Geophys. Res.*, **65**.
15. FITE, W. L., BRACKMAN, T. R. AND SNOW, W. R., 1958, Charge exchange in proton-hydrogen-atom collisions, *Phys. Rev.*, **112**, 1161.
16. STUART, G. W., 1959, Satellite measured radiation, *Phys. Rev. Letters*, **2**, 417.
17. VERNOV, S. N., CHUDAKOV, A. E., LEBEDINSKY, A. I. AND IVANENKO, I. P., 1960, Composition of the earth's corpuscular radiation and possible mechanisms of its origin, *Proc. Moscow Cosmic Ray Conference*, (Moscow 1960), **3**, 46.
18. VAN ALLEN, J. A. AND FRANK, L. A., 1959, Radiation measurements to 658,300 km with Pioneer IV, *Nature*, **184**, 219.
19. JACCHIA, L. G., 1959, Corpuscular radiation and the acceleration of artificial satellites, *Nature*, **183**, 526.
20. NICOLET, M. AND CHAPMAN, S., 1960, *Physics of the Upper Atmosphere*, ed. J. A. Ratcliffe, Academic Press, New York, Chaps. 1 and 2.
21. HOROWITZ, R. AND LA GOW, H. E., 1957, Upper air pressure and density measurements from 90 to 220 km with Viking 7 rocket, *J. Geophys. Res.*, **62**, 57.
22. HOROWITZ, R., LA GOW, H. E. AND GUILIANI, J. F., 1959, Fall-day auroral-zone atmosphere structure measurements from 100 to 188 km, *J. Geophys. Res.*, **64**, 2287.
23. OPIK, E. J. AND SINGER, S. F., 1959, Distribution of density in a planetary exosphere, *Phys. Fluids*, **2**, 653.
24. NICOLET, M., 1959, Constitution of the atmosphere at ionospheric levels, *J. Geophys. Res.*, **64**, 2092.
25. JOHNSON, F. S., 1960, The exosphere and upper *F* region, *J. Geophys. Res.*, **65**, 2571.
26. KUPPERIAN, J. E., BYRAM, E. T., CHUBB, T. A. AND FRIEDMAN, H., 1958, Extreme ultraviolet radiation in the night sky, *Ann. Geophys.*, **14**, 329.
27. PURCELL, J. D. AND TOUSEY, R., 1960, The profile of solar hydrogen-Lyman- $\alpha$ , *J. Geophys. Res.*, **65**, 370.
28. JASTROW, R., 1959, Outer atmospheres of the earth and planets, *J. Geophys. Res.*, **64**, 1789.
29. JOHNSON, F. S., 1960, Pressure and temperature equalisation at 200 km altitude, *J. Geophys. Res.*, **65**, 2227.
30. ELFord, W. G., 1959, Winds in the upper atmosphere, *J. Atmos. Terr. Phys.*, **15**, 132.
31. FRIEDMAN, H., 1959, Rocket observations of the ionosphere, *Proc. I.R.E.*, **47**, 272.
32. FRIEDMAN, H., 1960, The sun's ionizing radiations, *Physics of the Upper Atmosphere*, ed. J. A. Ratcliffe, Academic Press, New York, Chap. IV.
33. JOHNSON, C. Y., MEADOWS, E. B. AND HOLMES, J. C., 1958, Ion composition of the Arctic ionosphere, *J. Geophys. Res.*, **63**, 443.
34. NICOLET, M., 1960, The formation of the *D*-layer of the ionosphere, *J. Geophys. Res.*, **65**, 1469.

35. JOHNSON, F. S., 1960, Ion distribution above the  $F_2$  maximum, *J. Geophys. Res.*, **65**, 577.
36. STOREY, L. R. O., 1953, An investigation of whistling atmospherics, *Phil. Trans.*, A, **246**, 113.
37. ALLCOCK, G. MCK., 1959, The electron density distribution in the outer ionosphere derived from whistler data, *J. Atm. Terr. Phys.*, **14**, 185.
38. GARRIOTT, O. K., 1960, The determination of ionospheric electron content and distribution from satellite measurements, *J. Geophys. Res.*, **65**, 1139.

# BUCKLING OF THIN CIRCULAR CONICAL SHELLS SUBJECTED TO AXISYMMETRICAL TEMPERATURE DISTRIBUTIONS\*

JOSEF SINGER

*Department of Aeronautical Engineering, Technion-Israel Institute of Technology, Haifa*

## ABSTRACT

A method developed previously for the analysis of the instability of conical shells under external pressure<sup>1</sup> is now applied to the problem of buckling due to axisymmetrical temperature distributions.

The method is based on a solution of the Donnell type stability equations, derived by Seide<sup>2,3</sup> in the presence of slightly relaxed boundary conditions. The solution satisfies the usual simple support conditions regarding the radial deflections  $w$ , rigorously, but implies elastic restraints as far as the axial and circumferential displacements are concerned. However, the constraint on the circumferential,  $v$ , displacements is of such a nature that it practically represents the rigid fixation required by the usual simple supports; and the much weaker constraint on the axial,  $u$ , displacements (in the direction of the generators) combines with the very small  $u$  displacements themselves to a condition approximating freedom from axial restraint. The effect of the  $u$  restraint on the instability of cylindrical and conical shells under external pressure was previously investigated and the critical pressures found to differ by 1–2 percent for typical shells<sup>4,5</sup>.

The stability equation in the radial direction is then rederived in a modified form to facilitate solution by the Galerkin method.

This solution may be applied to any type of loading for which the prebuckling stresses are functions of  $x$  only and the hoop stresses are the prime cause of buckling. The thermal stresses due to an axisymmetrical temperature distribution are such a case.

The thermal stresses may be computed from Meissner type equations, since the equilibrium equations upon which the Seide stability equations are based, reduce to Meissner equations for rotational symmetry. A solution for the Meissner equations in the presence of axisymmetrical temperature distribution given by Huth<sup>6</sup>, but in a slightly modified form, is used here for the calculation of the thermal stresses.

For the thermal buckling analysis the thermal stresses are then expressed so that their magnitude depends on a temperature parameter  $T_1$ , which also determines the

---

\* This paper is based on research supported by the United States Air Force through the Air Force Office of Scientific Research, ARDC, under Contract No. AF 61 (052)—339.

magnitude of the temperature distribution, and their functional form is approximated by power series in  $x$ .

A method for the calculation of the critical temperature parameter  $T_1$  (which indicates the onset of buckling), similar to the above mentioned method for the buckling under external pressure, is then developed. The method is also suitable for analysis of a shell subjected simultaneously to external pressure and axisymmetrical temperature distributions. Typical cases are analysed.

#### REFERENCES

1. SINGER, JOSEF, 1960, Buckling of circular conical shells under axisymmetric external pressure, *Technion Research and Development Foundation, Haifa Israel*, AF OSR TN 60-711.
2. SEIDE, PAUL, 1957, A Donnell type theory for asymmetrical bending and buckling of thin conical shells, *Journal of Applied Mechanics*, **24**, 547.
3. SEIDE, PAUL, 1957, Note on "Stability equations for conical shells", *Journal of the Aeronautical Sciences*, **28**, 342.
4. SINGER, JOSEF, 1959, The effect of axial constraint on the instability of thin circular cylindrical shells under external pressure, *Journal of Applied Mechanics*, **27**, 737; also, *Technion Research and Development Foundation, Haifa, Israel*, Technical Note No. 1, Contract No. AF 61(052)-123, September 1959.
5. SINGER, JOSEF, 1960, The effect of axial constraint on the instability of thin conical shells under external pressure, *Technion Research and Development Foundation, Haifa, Israel*, AF OSR TN 60-860, December.
6. HUTH, J. H., 1953, Thermal stresses in conical shells, *Journal of the Aeronautical Sciences*, **20**, 613.



# ON THE PHYSICAL RIEMANN-CHRISTOFFEL TENSOR IN ORTHOGONAL COORDINATES

ZVI KARNI

*Division of Mechanics, Technion-Israel Institute of Technology, Haifa*

## ABSTRACT

Expression for the physical Riemann-Christoffel tensor is derived and its geometrical meaning stated.

1. The derivation of the physical Riemann-Christoffel tensor, also known as the curvature tensor, is based on the concept of the curvilinear derivative of a physical tensor and that of the physical Christoffel symbols. The definition and derivation of these concepts form the subject of a separate paper\* of which only the main results will here be stated.

A three-dimensional curvilinear network is formed by the families of curves  $x_i = \text{const.}$  ( $i = 1, 2, 3$ ) where the  $x_i$  denote the curvilinear coordinates of a point in the space. The network can also be represented by means of the position vector  $\mathbf{r}(x_1, x_2, x_3)$  or  $\mathbf{r}(y_1, y_2, y_3)$  where the  $y_i$  stand for the cartesian coordinates. The positive unit tangent vectors to the curves at a point of the network, denoted  $\mathbf{t}_i$ , form a local cartesian system of coordinates. A physical tensor is defined with respect to the local system, hence it is always a cartesian tensor.

The two-fold metric system  $g_{ij}$  (which is not a physical tensor) is found from

$$g_{ij} = \frac{\partial y_\alpha}{\partial x_i} \frac{\partial y_\alpha}{\partial x_j} \quad (1.1)$$

where it should be understood that repeated Greek indices only imply summation while repeated Latin indices are not summed. The necessary and sufficient condition for a curvilinear network to be orthogonal is

$$g_{ij} = 0 \quad (i \neq j) \quad (1.2)$$

The discussion in this paper is confined to orthogonal coordinates only, hence all indices are written as subscripts.

\* By Braun, Karni and Reiner, to be published shortly.

The "curvilinear derivative" at a point  $P$  of the network of a vector field  $\mathbf{A}$  is identified with the vector difference of the vector field while proceeding along a curve of the network and per unit arc length  $ds_i$ . This derivative is denoted by a comma, thus

$$\mathbf{A}_{,j} = \frac{\partial \mathbf{A}}{\partial s_j} \quad (1.3)$$

where

$$ds_i = \sqrt{g_{ii}} dx_i \quad (1.4)$$

The physical Christoffel symbols  $G_{ijk}$  are defined as the projections of the three principal curvatures  $1/\rho_i$  of the coordinate curves on the planes of the local system  $\mathbf{t}_i$  at  $P$ . Thus  $G_{ijk}$  means the projection of the principal curvature  $1/\rho_i$  on the plane formed by the unit tangents  $\mathbf{t}_j$  and  $\mathbf{t}_k$ , namely the plane  $\mathbf{t}_j \times \mathbf{t}_k$ . From the definition it follows that

$$G_{ijk} = -G_{ikj} \quad (1.5)$$

Furthermore, for three mutually different indices

$$G_{ijk} = 0 \quad (i \neq j \neq k \neq i) \quad (1.6)$$

because the principal curvature  $1/\rho_i$  has no projection on its tangent  $\mathbf{t}_i = \mathbf{t}_j \times \mathbf{t}_k$ . In view of (1.5) and (1.6), the matrix of the non-vanishing symbols takes the form

$$\|G_{iji}\| = -\|G_{iij}\| = \begin{vmatrix} 0 & G_{121} & G_{131} \\ G_{212} & 0 & G_{232} \\ G_{313} & G_{323} & 0 \end{vmatrix} \quad (1.7)$$

The  $G_{ijk}$  can be calculated from the components of the metric system  $g_{ij}$  by means of the relation

$$G_{ijk} = \frac{1}{2\sqrt{g_{ii} g_{jj} g_{kk}}} \left( \frac{\partial g_{ik}}{\partial x_j} - \frac{\partial g_{ij}}{\partial x_k} \right) \quad (1.8)$$

It should be noted that the physical Christoffel symbols form a tensor of the third rank with the property of skew-symmetry — Eq. (1.5).

The  $i$ -th component of the curvilinear derivative of  $\mathbf{A}$  — Eq. (1.3) — is now expressed in terms of the symbols  $G_{ijk}$  as

$$(\mathbf{A}_{,j})_i \equiv A_{i,j} = \frac{\partial A_i}{\partial s_j} + A_a G_{j ai} \quad (1.9)$$

The curvilinear derivative of an absolute physical tensor of rank  $n$  is given by

$$A_{i_1 i_2 \dots i_n, j} = \frac{\partial A_{i_1 i_2 \dots i_n}}{\partial s_j} + A_{a i_2 \dots i_n} G_{j a i_1} + A_{i_1 a \dots i_n} G_{j a i_2} + \dots A_{i_1 i_2 \dots a} G_{j a i_n} \quad (1.10)$$

2. The physical Riemann-Christoffel tensor  $R_{ijkl}$  is obtained on performing the difference in the second, mixed derivative along a curve of the vector  $A_i$ , namely

$$A_{i,kl} - A_{i,lk} = A_\alpha R_{i\alpha kl} \quad (2.1)$$

In view of Eqs. (1.8), (1.9), (1.10) and the identity, obtained from Eq. (1.8),

$$G_{ljk} + G_{jkl} + G_{kij} = 0$$

it is found that

$$R_{ijkl} = \frac{\partial G_{kji}}{\partial s_l} - \frac{\partial G_{lji}}{\partial s_k} + G_{k\beta i} G_{l\beta j} - G_{l\beta i} G_{k\beta j} + G_{\beta ij} G_{\beta kl} \quad (2.2)$$

Again, in view of Eqs. (1.5), (1.6), (1.8) it is readily established that

$$R_{ijkl} = -R_{ijlk} = -R_{jilk} = R_{klij} \quad (2.3)$$

The symmetrical and skew-symmetrical properties of the physical tensor are thus similar to those of the corresponding analytical tensor, denoted here as  $R_{ijkl}^*$ , which is obtained on performing the similar difference in the second covariant derivatives of a contravariant vector  $A^i$ . The principal distinction between the two tensors is in the dimensions of the two. All the components of the physical tensor possess the same dimension, that of the square of curvature, whereas the components of the analytical tensor need not be of the same dimension in the various curvilinear coordinates. The relation between the two tensors in orthogonal coordinates is

$$R_{ijkl}^* = \sqrt{g_{ii}g_{jj}g_{kk}g_{ll}} R_{ijkl} \quad (2.4)$$

The six non vanishing components of the Riemann-Christoffel tensor in a three dimensional space, as results from Eq. (2.3), form a symmetric matrix

$$\| R_{ijkl} \|_{1,2,3} = \begin{vmatrix} R_{1212} & R_{1223} & R_{1231} \\ \cdot & R_{2323} & R_{2331} \\ \cdot & \cdot & R_{3131} \end{vmatrix} \quad (2.5)$$

It is also known that

$$\frac{R_{1212}^*}{g_{11}g_{22}} = -K$$

where  $K$  stands for the Gaussian curvature; hence from Eq. (2.4)

$$R_{1212} = -K \quad (2.6)$$

We therefore conclude that the three "normal" (diagonal) components in the matrix (2.5), namely of the type  $R_{ijij}$ , coincide precisely with the Gaussian curvatures of the three surfaces formed by each pair of the coordinate curves of the network.

3. If we consider the vector  $\mathbf{t}$ , the components of which  $t_i$  are the unit tangents of the network at  $P$ , as an example of a vector field, then the single non-vanishing component of the Riemann-Christoffel tensor in a two-dimensional space (surface) is found from Eq. (2.1) and (2.3) to be

$$t_{1,12} - t_{1,21} = t_2 R_{1212} = R_{1212} = t_{2,21} - t_{2,12} = t_1 R_{2121} = R_{2121} \quad (3.1)$$

Now,  $t_{1,12}$  means the projection on the local axis  $t_1$  of the second vector difference of the tangent  $\mathbf{t}$  while traversing along the arc of unit length  $ds_1$  first, then along the unit arc  $ds_2$ , namely

$$t_{1,12} = \left( \frac{\partial}{\partial s_2} \frac{\partial \mathbf{t}}{\partial s_1} \right)_1 \quad (3.2)$$

Alternatively, if the tangent vectors at  $P, P', P'', P'''$  are labelled  $\mathbf{t}', \mathbf{t}'', \mathbf{t}'''$  respectively (Figure 1b), then  $t_{1,12}$  is obtained from the vector difference of these vectors taken in the order

$$(\mathbf{t}''' - \mathbf{t}'') - (\mathbf{t}' - \mathbf{t})$$

Similarly,  $t_{1,21}$  is obtained from the vector difference taken in the order

$$(\mathbf{t}''' - \mathbf{t}') - (\mathbf{t}'' - \mathbf{t})$$

or

$$t_{1,21} = \left( \frac{\partial}{\partial s_1} \frac{\partial \mathbf{t}}{\partial s_2} \right)_1 \quad (3.3)$$

These projections, on either  $t_1$  or  $t_2$ , are in general not equal and the Riemann-Christoffel tensor measures the difference in value of these projections. In the case of the sphere  $\mathbf{r}(\theta, \varphi, a)$  for example (Figure 1a)



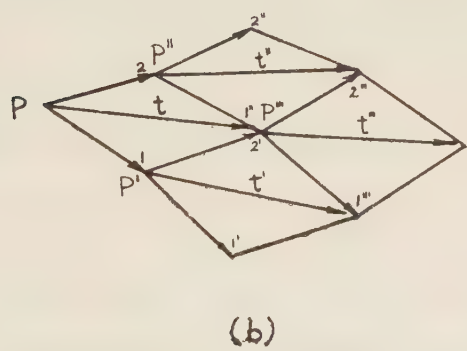
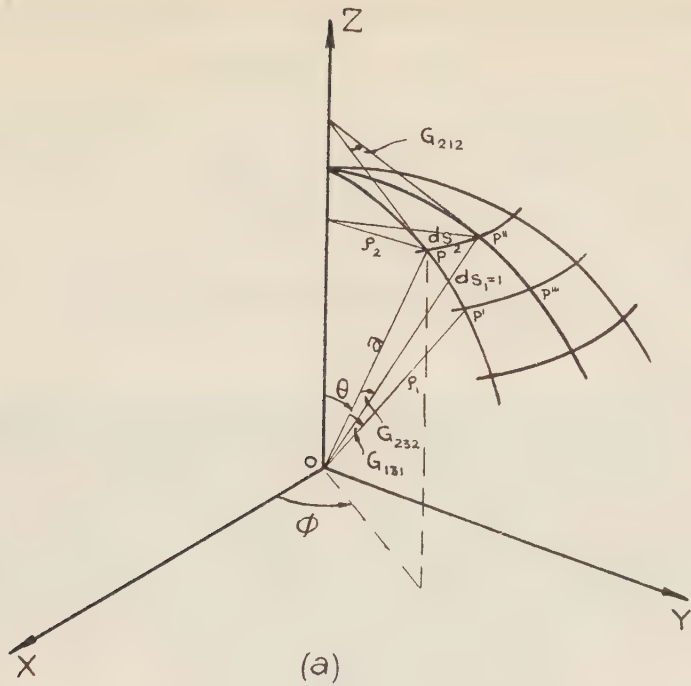


Figure 1  
a. Curvilinear network on a sphere of unit arcs to  $ds_i$   
b. Tangent vectors with respect to the local systems

the matrix of the physical Christoffel symbols reads

$$\| G_{iji} \|_{1,2} = \begin{vmatrix} 0 & 0 \\ \text{ctg } \theta & 0 \\ \frac{1}{a} & \end{vmatrix} \quad (3.4)$$

making use of Eqs. (1.1), (1.3), (1.9), (1.10) and (3.4), we find for Eqs. (3.2), (3.3)

$$t_{1,12} = -t_{2,12} = \left( \frac{\text{ctg } \theta}{a} \right)^2;$$

$$-t_{1,21} = t_{2,21} = \frac{1}{a} \frac{\partial}{\partial \theta} \left( \frac{\text{ctg } \theta}{a} \right)$$

Consequently,

$$R_{1212} = R_{2121} = \frac{1}{a} \frac{\partial}{\partial \theta} \left( \frac{\text{ctg } \theta}{a} \right) + \left( \frac{\text{ctg } \theta}{a} \right)^2 = -\frac{1}{a^2} = -K$$

in view of Eq. (2.6).

What has been said about the geometrical interpretation of a single component of the physical Riemann-Christoffel tensor applies equally well to the other components, all being of the same physical dimension. Not so with the analytical tensor the meaning of which can only be sought in conjunction with other quantities which make the entire expression an invariant. We know that if a vector  $A^{*i}$  of unit length undergoes a parallel displacement from a point  $P$  along a closed curve in a continuum, then the angle formed by the vector on returning to  $P$  can be expressed in terms of  $R_{ijkl}^*$  and the surface element bounded by the curve. When, therefore, the direct physical or geometrical interpretation of a tensor is of an interest, the physical tensor has this advantage over the corresponding analytical one.

# HYDRODYNAMICAL APPLICATIONS OF A THEOREM ON SPHERICAL MEANS

ERI JABOTINSKY

*Division of Mathematics, Technion-Israel Institute of Technology, Haifa*

## ABSTRACT

A Theorem on vectorial spherical means is applied to the angular momentum theorem for a spherical volume completely immersed in a laminar flow. The resulting formula yields directly classical results for perfect fluids and shows that  $\text{rot rot rot } \mathbf{v}$  is an indicator of magnitude of the moments of shear and thus possibly also of the conditions for the inception of turbulence.

Consider a portion of the medium in a volume  $\tau$  inside a closed surface  $\sigma$ . Let  $d\tau$  be an element of the volume  $\tau$ . Denote by  $\rho(x, y, z, t)$ ,  $\mathbf{v}(x, y, z, t)$  and  $\mathbf{a}(x, y, z, t)$  respectively the density, the velocity and the acceleration of the matter in  $d\tau$ . We note that

$$\mathbf{a} = \frac{d\mathbf{v}}{dt} = \frac{\partial \mathbf{v}}{\partial t} + (\mathbf{v} \cdot \nabla) \mathbf{v}.$$

Let  $\mathbf{f} \rho d\tau$  be the outside volume force acting on the matter in  $d\tau$ , and let  $\mathbf{F} d\sigma$  be the outside surface force acting through  $d\sigma$ . Furthermore denote by  $\mathbf{r}$  the position vector of points in  $\tau$  or on  $\sigma$ , that is the position vector of volume elements  $d\tau$  or of surface elements  $d\sigma$  relatively to a fixed origin  $O$ .

Then the angular momentum theorem, applied to the matter within  $\sigma$ , yields:

$$\int \int_{\sigma} (\mathbf{r} \times \mathbf{F}) d\sigma + \int \int \int_{\tau} (\mathbf{r} \times \mathbf{f}) \rho d\tau = \frac{d}{dt} \int \int \int_{\tau} (\mathbf{r} \times \mathbf{v}) \rho d\tau.$$

Differentiating under the integral sign and using the equation of continuity and the fact that  $\frac{d\mathbf{r}}{dt} = \mathbf{v}$  and collecting the volume integrals, we find:

$$\int \int_{\sigma} (\mathbf{r} \times \mathbf{F}) d\sigma = \int \int \int_{\tau} [\mathbf{r} \times (\mathbf{a} - \mathbf{f})] \rho d\tau. \quad (1)$$

We shall need here only the special case in which (1) is applied to the matter inside a spherical surface  $\Sigma$  and the origin  $O$  of the position vectors  $\mathbf{r}$  is the fixed point which, at the moment  $t$ , coincides with the center of  $\Sigma$ . Here only the tangential components of the surface forces  $\mathbf{F}$  contribute to the moments  $(\mathbf{r} \times \mathbf{F}) d\sigma$ . We shall denote by  $S$  the spherical volume inside  $\Sigma$ .

## THEOREM I.

Consider a continuous medium of density  $\rho(x,y,z,t)$ . Inside that medium consider a spherical surface  $\Sigma$  of radius  $R$ , enclosing the spherical volume  $S$ . Let  $\mathbf{r}$  be the position vector of the surface element  $d\Sigma$  of  $\Sigma$  or of the volume elements  $dS$  of  $S$  relative to the center of  $\Sigma$ . Let  $\mathbf{T}d\Sigma$  be the shear applied to the matter in  $S$  by the outside medium through  $d\Sigma$  and let  $\rho\mathbf{f}(x,y,z,t)dS$  be the external volume force applied to the matter in the volume element  $dS$ . Then, if  $\mathbf{a}$  is the acceleration of the matter in  $dS$ :

$$\iint_{\Sigma} (\mathbf{r} \times \mathbf{T}) d\Sigma = \frac{4\pi}{15} R^5 \overline{\text{rot } \rho(\mathbf{a} - \mathbf{f})}, \quad (2)$$

where  $\overline{\text{rot } \rho(\mathbf{a} - \mathbf{f})}$  is the weighted average of  $\text{rot } \rho(\mathbf{a} - \mathbf{f})$  in  $S$  given by:

$$\iiint_S \frac{R^2 - r^2}{2} \text{rot } \rho(\mathbf{a} - \mathbf{f}) dS = \frac{4\pi}{15} R^5 \overline{\text{rot } \rho(\mathbf{a} - \mathbf{f})}. \quad (3)$$

PROOF: The angular momentum theorem can here be written

$$\iint_{\Sigma} (\mathbf{r} \times \mathbf{T}) d\Sigma = \iiint_S [\mathbf{r} \times (\mathbf{a} - \mathbf{f})] \rho dS,$$

and it remains to transform the volume integral. We have:

$$\iiint_S [\mathbf{r} \times (\mathbf{a} - \mathbf{f})] \rho dS = \int_{\beta=0}^{\beta=R} d\beta \iint_{\Sigma_{\beta}} [\mathbf{r} \times (\mathbf{a} - \mathbf{f})] \rho d\Sigma_{\beta},$$

where  $\Sigma_{\beta}$  is the spherical surface of center  $O$  and radius  $\beta$ . Putting  $\mathbf{r} = \beta \mathbf{n}$  where  $\mathbf{n}$  is the unit vector normal to  $d\Sigma_{\beta}$  and denoting by  $S_{\beta}$  the interior of  $\Sigma_{\beta}$  we have, by a classical result:

$$\iint_{\Sigma_{\beta}} [\mathbf{r} \times (\mathbf{a} - \mathbf{f})] \rho d\Sigma_{\beta} = \beta \iint_{\Sigma_{\beta}} [\mathbf{n} \times (\mathbf{a} - \mathbf{f})] \rho d\Sigma_{\beta} = \beta \iiint_{S_{\beta}} \text{rot } \rho(\mathbf{a} - \mathbf{f}) dS_{\beta},$$

so that:

$$\iiint_S [\mathbf{r} \times (\mathbf{a} - \mathbf{f})] \rho dS = \int_{\beta=0}^{\beta=R} \beta d\beta \iiint_{S_{\beta}} \text{rot } \rho(\mathbf{a} - \mathbf{f}) dS_{\beta} = \iiint_S \frac{R^2 - r^2}{2} \text{rot } \rho(\mathbf{a} - \mathbf{f}) dS.$$

We thus have:

$$\iint_{\Sigma} (\mathbf{r} \times \mathbf{T}) d\Sigma = \iiint_S \frac{R^2 - r^2}{2} \text{rot } \rho(\mathbf{a} - \mathbf{f}) dS, \quad (4)$$

and the main theorem follows because:

$$\iiint_S \frac{R^2 - r^2}{2} dS = \frac{4\pi}{15} R^5.$$



## APPLICATION TO SOLIDS

In a solid  $\text{rot } \mathbf{a}$  is constant in space. Indeed if  $\omega$  is the angular velocity of the solid at the time  $t$ , then:

$$\text{rot } \mathbf{a} = 2 \frac{d\omega}{dt}. \quad (5)$$

This is due to the fact (which is easily checked analytically) that in a solid:

$$\text{rot } \frac{d\mathbf{v}}{dt} = \frac{d}{dt} \text{rot } \mathbf{v},$$

and:

$$\text{rot } \mathbf{v} = 2\omega.$$

Therefore, for a homogenous solid, our Theorem I becomes:

## THEOREM II.

(Homogenous solid medium). If the medium is solid and homogenous of constant density  $\rho$  then:

$$\iiint_{\Sigma} (\mathbf{r} \times \mathbf{T}) d\Sigma = \frac{8\pi}{15} R^5 \rho \frac{d\omega}{dt}. \quad (6)$$

This yields interesting conclusions on the maximum  $\left| \frac{d\omega}{dt} \right|$  a solid can sustain without splitting.

## APPLICATION TO PERFECT FLUIDS

In a perfect fluid  $\mathbf{T} = 0$  and Theorem I yields easily:

## THEOREM III.

(Perfect fluids). In a non-viscous medium where all shears are zero:

$$\text{rot } \rho(\mathbf{a} - \mathbf{f}) = 0. \quad (7)$$

Three special cases are of interest:

A) *Incompressible perfect fluid.*

Here  $\rho$  is constant. If  $\mathbf{f}$  is the constant field of gravity,  $\text{rot } \mathbf{f} = 0$  and Theorem IV reduces to:

## THEOREM IV.

*In an incompressible perfect fluid under gravity:*

$$\text{rot } \mathbf{a} = 0 \quad (8)$$

B) *Two dimensional horizontal flow of a perfect fluid.*

Vector  $\mathbf{a}$  is now horizontal while  $\mathbf{f}$  is vertical. Writing that the vertical component of  $\text{rot } \rho(\mathbf{a} - \mathbf{f})$  is zero, we find, in this case:

## THEOREM V.

*In a two dimensional horizontal flow of a perfect fluid:*

$$\mathbf{rot} \rho \mathbf{a} = 0. \quad (9)$$

C) *Two-dimensional horizontal irrotational flow of a perfect fluid:*

In this case  $\mathbf{rot} \mathbf{v} = 0$ , which implies  $\mathbf{rot} \mathbf{a} = 0$  (this is easily checked analytically). Remembering that

$\mathbf{rot} \rho \mathbf{a} = \rho \mathbf{rot} \mathbf{a} - \mathbf{a} \times \mathbf{grad} \rho$  and applying formula (9) we find:

$$\mathbf{a} \times \mathbf{grad} \rho = 0 \quad (10)$$

which yields:

## THEOREM VI.

*In a two-dimensional irrotational flow of a perfect fluid in a horizontal plane the acceleration is parallel to the gradient of the density.*

## APPLICATION TO VISCOUS FLUIDS

We limit ourselves to the incompressible case with constant viscosity  $\mu$ . The Navier-Stokes equation here is:

$$\rho(\mathbf{a} - \mathbf{f}) = -\mathbf{grad} p + \mu \Delta \mathbf{v}$$

But  $\mathbf{rot} \mathbf{grad} p = 0$  and  $\Delta \mathbf{v} = \mathbf{grad} \operatorname{div} \mathbf{v} - \mathbf{rot} \mathbf{rot} \mathbf{v} = -\mathbf{rot} \mathbf{rot} \mathbf{v}$  for  $\operatorname{div} \mathbf{v} = 0$ , so that Theorem I now becomes:

## THEOREM VII.

*In the flow of an incompressible fluid of constant viscosity:*

$$\iint_{\Sigma} (\mathbf{r} \times \mathbf{T}) d\Sigma = -\mu \iiint_S \frac{R^2 - r^2}{2} \mathbf{rot} \mathbf{rot} \mathbf{rot} \mathbf{v} dS = -\frac{4\pi}{15} R^5 \mu \overline{\mathbf{rot} \mathbf{rot} \mathbf{rot} \mathbf{v}}$$

This result shows that the value of  $|\mathbf{rot} \mathbf{rot} \mathbf{rot} \mathbf{v}|$  is a measure of the moments of the shears in the considered flow and may possibly be an indicator for the condition of the inception of turbulence.

# THE MECHANICAL PROPERTIES AND STRUCTURE OF SOME HIGH TENSILE ALLOY STEELS

S. BECKER AND M. G. BADER

*Israel Atomic Energy Commission and Battersea College of Technology, London*

## ABSTRACT

Some outstanding results have been obtained while the mechanical and tempering properties of some silicon – molybdenum – vanadium – copper high tensile alloy steels have been investigated, in the water quenched and tempered condition. Metallography has been limited to optical microscopy, in spite of this limitation some relationship between mechanical properties and microstructure could be found.

## 1. PREFACE

The work described in this report was carried out at Battersea College of Technology, London, and forms part of a much larger investigation in progress.

During the period of the present work the first author has been in receipt of a Travelling Scholarship provided by the British Council, for which he would like to express his appreciation.

The authors would also like to thank all those in the Metallurgy Department, Battersea College of Technology, for their advice and encouragement, especially to Mr. L. W. Derry and Dr. B. L. Daniel.

## 2. MATERIAL

The steels were manufactured from Swedish iron, and appropriate master alloys in a vacuum induction furnace. Ingots of approximately 56 lb. weight were produced and these were hot rolled to a bar of approximately 5/8" diameter except in the case of steel "D" which was rolled to approximately  $2\frac{1}{2}" \times 5/8"$  so that test pieces could be extracted in the transverse direction. Test piece blanks about  $2\frac{1}{2}"$  long were heat treated and test pieces were then machined.

The composition and treatment of the steels are shown in Tables I and II and it should be noted that Steels "A" and "D" are of similar composition and treatment but in "A" the test pieces are parallel to the rolling direction and in "D" they are transverse.

On account of the high hardness of many samples of both, the gauge length and the threaded portions of the test pieces were ground.

Owing to the short supply of material there were in some cases insufficient test pieces for a full range of heat treatments. When this was so, small test specimens were heat treated to obtain the hardness figures.

TABLE I  
*Analysis of steels (% — WT)*

Steel	C	Si	Cu	Mo	V	Mn	S	P	Ni	Cr	Al
C	0.45	1.22	0.90	1.86	0.13	0.35	0.019	0.060	0.02	0.04	0.015
Q	0.38	1.56	2.35	0.98	0.35	0.47	0.009	0.005	0.01	0.02	0.04
L	0.37	1.50	1.62	2.08	0.36	0.52	0.008	0.026	0.01	0.04	0.04
O	0.32	1.50	2.52	1.49	0.34	0.43	0.009	0.018	0.01	0.03	0.04
E	0.29	1.55	2.06	0.94	0.28	0.50	0.027	0.025	0.02	0.04	—
F	0.28	1.06	1.45	2.50	0.34	0.25	0.023	0.034	0.02	0.04	—
A	0.18	1.50	1.73	0.80	0.30	0.29	0.033	0.016	0.06	0.16	—
D	0.18	1.50	1.73	0.80	0.30	0.29	0.033	0.016	0.06	0.16	—

Ae = Aluminium.

TABLE II  
*Heat treatment*

All specimens quenched from 970°C and tempered to the following temperatures:

Spec. No.	Treatment C	Treatment Q	Treatment L	Treatment O	Treatment E	Treatment F	Treatment A	Treatment D
1	—	A.Q.	—	A.Q.	A.Q.	A.Q.	A.Q.	A.Q.
2	87°C	100°C	100°C	100°C	105°C	110°C	100°C	100°C
3	215°C	245°C	235°C	235°C	205°C	220°C	200°C	200°C
4	395°C	395°C	400°C	400°C	390°C	405°C	390°C	390°C
5	505°C	535°C	515°C	525°C	515°C	530°C	505°C	505°C
6	600°C	600°C	600°C	600°C	600°C	600°C	600°C	600°C
7	—	—	650°C	650°C	650°C	650°C	650°C	650°C
8	—	—	—	700°C	700°C	700°C	700°C	700°C

A.Q. = as water quenched.

The 0.1 per cent proof stress, ultimate tensile strength, elongation reduction of area, Young's modulus and hardness have been measured in duplicate experiments and plotted graphically.

More than 50 microsections have been examined and 15 photomicrographs are presented.



### 3. EXPERIMENTAL PROCEDURE

#### (a) *Mechanical testing*

One hundred and eleven test pieces were tested on a Denison 50 ton tensile testing machine, using a 1" Lamb optical extensometer. Full stress/strain graphs were plotted and elongation and reduction of area of test piece was measured. Typical stress strain curves are reproduced in Figures 1-8.\*

Hardness tests were conducted on all specimens on a Vickers diamond pyramid hardness testing machine with 30 kg load. Microhardness tests were conducted on some of the specimens using a Bell Telephone testing machine.

#### (b) *Metallographic examination*

Some fifty microsections cut in the longitudinal and transverse direction from the tensile test pieces have been examined after being polished and etched with 2% Nital. Twenty-three photomicrographs illustrating typical structures are shown. Only 10 photomicrographs are shown herewith.

### 4. MECHANICAL TEST RESULTS

The results of the tensile tests are shown in Figures 9-17.\*\*

The following quantities were determined:

- (a) 0.1 per cent proof stress (Tons per sq. inch)
- (b) Ultimate tensile strength (Tons per sq. inch)
- (c) Elongation (% on  $4\sqrt{\text{Area}}$ )
- (d) Reduction of area (%)
- (e) Hardness (V.P.N. HD/30)
- (f) Young's Modulus (lb/sq. inch)

#### *Steel "C" (Figures 1 and 9)*

This steel has the highest carbon content (0.45%C) of those tested but the other alloying elements are relatively low, particularly copper and vanadium.

A tensile strength of about 150 tons per sq. inch. together with elongation of 8% was obtained in the as quenched condition. The tensile strength drops quite rapidly on tempering to 100 tons per sq. inch at 600°C. (This may be compared with 0.45 per cent plain carbon steel as quenched approx. 130 t.s.i. dropping to 45 t.s.i. on tempering at 600°C).

The hardness follows the same trend as the tensile strength and agrees with the usually quoted relationship of  $\text{V.P.N.} \times 0.2 = \text{U.T.S.}$  Proof stress values however show an increase with tempering with a slight drop as the higher tempering tempe-

\* Only Figures, 1,6,7 are included in this paper (pp. 70-71).

\*\* Only Figures 9,10,13,14,15,17 are shown herewith (pp. 71-74).

ratures are achieved. With steel "C" as with most of the others investigated the elongation stays nearly constant on tempering up to 500°C while the reduction of area increases initially and then decreases.

### *Steel Q*

This steel is of lower carbon content than "C" and its alloying elements are somewhat higher. With this steel the rate of decreasing tensile strength and hardness is less than in "C". The 0.1 per cent proof stress increases on tempering up to 600°C, the ductility increases on tempering and the ratio of proof stress over ultimate tensile strength approaches unity.

### *Steel "L"*

There is doubt whether all the specimens in this batch responded to heat treatment. In particular there is a large difference between test pieces 2 and 2A\*. As it was not possible to obtain more material, small specimens cut from the broken test pieces were heat treated and the hardness figures obtained were very different from those obtained from the original heat treatment.

This being so, no further evaluation can be made on any of the other properties of the material or its structure.

### *Steel "O"*

The tensile strength shows only slight drop on tempering with a tendency to secondary hardening around 600°C. The proof stress rises slightly and then more drastically at 600°C, above 600°C the strength drops rapidly.

### *Steel "E"*

This steel is very similar to steel "O" which is discussed above.

### *Steel "F" (Figures 6 and 14)*

Generally very similar to Steels "O" and "E" but the secondary hardening is more marked. On tempering at 600°C its tensile strength is equal to the as quenched condition. This steel has the highest amount of carbide forming elements (Mo, V).

### *Steel "A" (Figures 7 and 15)*

This steel has the lowest carbon content (0.18 %C), of all the steels tested.

The general pattern of the curves is similar to steel "F". The tensile strength and hardness after tempering at 600°C are even higher than in the as quenched condition, also the 0.1 per cent proof stress shows the greatest increase between the as quenched and 600°C tempering temperatures of the steels under investigation.

---

\*\* Two specimens representative of each composition and heat treatment have been tested.

### *Young's Modulus*

This follows the well known<sup>13</sup> trend i.e. decrease of modulus for quenched steels with increase of carbon content. From Figure 17 it is seen that Young's modulus of steels "C" and "Q" is lower than of steels "L", "O", "E", "F", "A" which also show a tendency of increase of modulus on tempering. The modulus also increases quite appreciably on secondary hardening.

## 5. METALLOGRAPHIC EXAMINATION

Low power examination of longitudinal sections of the broken tensile test pieces revealed considerable banding in most of the steels. This can be seen in plates 1-4. There was also a considerable quantity of non-metallic inclusions often associated with the banding but not uniform throughout the bars.

Isolated large areas of a light etching constituent occurred in some steels, particularly in those of lower carbon contents as shown in plate 1. The exact nature of this constituent is not understood but it is possibly ferrite. The micro-hardness is 200-220 D.P.N.

It is possible that complete homogenisation was not obtained during the melting process and that these are regions of almost unalloyed iron.

In conclusion, it can be seen from the low power observation that the steels are far from homogenous and also relatively dirty for high grade alloy steels. This may be explained by the small experimental melts and small amount of reduction in hot working to produce the test bars. The need to conserve material has probably resulted in more of the ingot being utilized than in normal steelworks practice.

Examination at high power was carried out on several sections from each steel. In the as quenched condition the higher carbon steels "C", "Q", "L" and "O" were predominantly martensitic and the lower carbon steels "E", "F" and "A" showed considerable amounts of bainite.

Fine particles of microconstituent were visible in most of the as quenched steels and in some cases delineated the previous austenite grain boundaries. On tempering they increased in size and number, and in some cases the grain boundary effect was most marked. (Plates 6, 16, 20, 23). Precipitation also occurred in a random manner. The precipitated particles were very small and it was not possible to establish whether they were carbides or possibly the  $\epsilon$  (Cu Rich) Phase.

In most cases the background structure changed only slightly on tempering, and the sorbitic structure was only apparent on tempering at 650-700°C.

## 6. DISCUSSION

The breakdown of martensite in quenched steel during tempering has been studied by a number of workers, in carbon steels using mainly X-ray techniques, and dilatometric methods. In recent years with the development of the electron microscope it has been possible to follow the constitutional changes during different stages of



tempering. Using these means it has been proved that quenched hardened low alloy steels have the structure of tetragonal martensite, they may also contain residual face centred cubic austenite and "auto-tempered martensite"<sup>5,11,13</sup>.

The change in physical properties during tempering results from the combined effect of the decomposition of the two solid solutions, martensite and anstenite which is observed in three stages:

- (i) Precipitation of  $\epsilon$  - iron carbide (below 150°C)
- (ii) Transformation of retained anstenite into bainite (150°C–280°C)
- (iii) Precipitation of cementite (above 200°C)
- (iv) In some alloy steels an alloy carbide may form on tempering usually in the 400°C–700°C range.

The metallography in this work has been limited to optical microscopy which does not allow a detailed observation of the tempering process to be made. In spite of this limitation an attempt will be made to find a relationship between the mechanical results with:

- (a) Composition
- (b) Heat treatment
- (c) Microstructure.

Generally different quenching methods and alloy additions may alter the nucleation conditions of carbides or of solid solution and precipitation hardening. In designing for alloy steels to be used in the quenched and tempered condition it is usual to assume that if efficient quenching is achieved the as quenched strength of the steel depends predominantly upon the carbon content. The alloying elements are effective mainly in controlling martensitic hardenability and tempering characteristics so that in alloy steels a considerable upward displacement of the temperature ranges of tempering processes can occur.

It has been shown that when plain carbon steels are tempered from martensitic condition within the temperature range of 400°C–700°C their hardness decreases logarithmically with tempering time<sup>3</sup>. If the steels contain non-carbide forming alloying elements, this general type of softening still prevails although the rates of softening are decreased (e.g. silicon 0.5% delays martensite breakdown into ferrite and cementite due to solid solution hardening<sup>10</sup>, similar considerations apply to copper). With the addition of strong carbide forming elements such as molybdenum and vanadium the softening behaviour or tempering is greatly modified by the formation of a dispersion of alloy carbides. Between 200°C and 400°C i.e. within the temperature range of the precipitation and growth of cementite, alloy elements retard softening caused by tempering (see references<sup>5, 13</sup>) when present in sufficient amounts these alloy elements are about equally effective in retarding softening or even increasing hardness. If the amount is not sufficient to combine with all the carbon the retarding effect is not so obvious.



Thus there is a rapid decrease in hardness in a plain carbon steel between 250° and 450°C, but in the steels under investigation this drop has been delayed until temperatures between 600°C and 700°C are reached.

The addition of copper apart from retarding tempering of martensite confers some solution hardening by dissolving in ferrite and when present in sufficient quantity precipitation hardening occurs by precipitation of the  $\epsilon$  phase (solution of Fe in F.C.C. copper), this latter effect has by far the greatest influence on strength. The maximum hardening occurs in the range 400–500°C in copper bearing plain carbon steels <sup>4</sup>, but the temperature and extent of hardening might well be influenced by other alloying elements present.

### *Development of present steels*

In the development of the steels investigated there have been two main aims:

(a) Reduction on volume change on quenching, associated with the austenite to martensite reaction, and thus reduce internal stress and possibility of cracking on quenching.

(b) To retain high strength even after tempering at high temperatures.

To achieve the above aims silicon and molybdenum have been chosen as the principal alloying elements as they reduce the volume change during transformation <sup>10, 12, 14</sup> to a greater extent than more conventional alloying elements. In addition both elements have a marked effect in reducing martensitic breakdown on tempering.

Resistance to softening in the medium temperature range is achieved by the precipitation hardening due to the copper, and at higher temperatures secondary hardening occurs due to the formation of molybdenum and vanadium carbides.

The full interpretation of this somewhat complicated state of affairs is beyond the scope of the present work but, nevertheless, certain trends are indicated by study of the data obtained:

(a) Quenched strength is determined by carbon content. Steel "Q" has approximately the same composition as "E" except for the carbon content, steel "Q" shows a higher quenched hardness than steel "E".

(b) The copper to carbon and the silicon to carbon ratios determine initial decrease in strength on tempering <sup>9, 10</sup>.

This trend is seen mainly when comparing steel "Q" and "A" which differ mainly in the carbon content other alloying elements being similar in both steels. It is suggested that the higher the ratio of  $S_i + C_u/C$  the less will be the decrease in hardness in the 200°C–450°C tempering range.

(c) The ratio of molybdenum and vanadium to carbon determines secondary hardening. Steel "F" having twice the ratio of steel "C" will show more pronounced secondary hardening. This may indicate that there is a certain ratio of  $M_0 + V$  versus carbon for secondary hardening. This was also observed by some investigators in other steels <sup>2, 5, 11</sup>.

(d) The limit of proportionality is very low in the as quenched steels as can be seen in Figures 1, 6, 7 and in the P.S./U.T.S. ratio. On tempering there is an increase in P.S./U.T.S. which approximates to 0.90 at 600°C.

This is typical of precipitation hardening alloys. It is noteworthy that an increase in limit of proportionality occurs even on tempering below 200°C corresponding to the first stage of martensite breakdown ( $\epsilon$  carbide formation), or to transformation of retained austenite although there is no metallographic evidence of this.

## 7. CONCLUSIONS

Remarkable mechanical properties are obtained in the steels investigated. Tensile strength of 90–110 tons per sq. inch together with elongations of the order of 10–15% are obtained with little or no reduction on tempering up to 600°C.

These steels are still in the experimental stage and have yet to be evaluated in service but would seem to offer improved properties when compared with more conventional steels, particularly for operation at elevated temperatures.

In their present form water quenching is necessary for hardening and while it is more usual to prefer oil quenching steels in industry the objection to water quenching is largely overcome, because these steels have a low volume change on transformation.

There is insufficient evidence from the present work to suggest an optimum composition for this class of steel, and it is probable that variations for different applications will be required. However, although higher strength is obtained in steel "C" by nature of its higher carbon content the ductility is reduced, which suggests that the lower carbon versions might be more suitable for general use.

It would no doubt be possible to produce an oil-hardening version of these steels by increasing the hardenability by addition of suitable elements.

## REFERENCES

1. STEVEN, W., 1956, The temperature of formation of martensite and Bainite in low alloy steels, *J.I.S.I.*, **183**, 349.
2. KUO, K., 1956, Alloy carbides precipitates during the fourth stage of tempering, *J.I.S.I.*, **184**, 258.
3. HYAM, E. D. AND NUTTING, J., The tempering of plain carbon steels, *J.I.S.I.*, **184**, 148.
4. IRVINE *et al.*, 1957, The physical metallurgy of low carbon low alloy steels containing boron, *J.I.S.*, **186**, 54.
5. SMITH, E. AND NUTTING, J., 1957, The tempering of low alloy creep-resistant steels containing chromium, molybdenum and vanadium *J.I.S.I.*, **187**, 314.
6. IRVINE, K. J. AND PICKERING, F. B., 1957, Low carbon Bainitic steels, *J.I.S.I.*, **187**, 292.
7. IRVINE, K. J. AND PICKERING, F. B., 1958, Carbon bainitic steels, *J.I.S.I.*, **188**, 101.
8. SEAL, A. K. AND HONEYCOMBE, R. W. K., 1958, The effect of tantalum and niobium on the tempering of certain vanadium and molybdenum steels, *J.I.S.I.*, **188**, 343.

9. LORIG, C. H. AND ADAMS, R. R., 1957, Copper as an alloying element in steel and cast iron, McGraw Hill, New York.
10. KENNEFORD, A. S. AND WILLIAMS, T., 1957, The effect of some common alloying elements on the breakdown of martensite in water quenched 0.35% Carbon steel, *J.I.S.I.*, **186**,
11. IRVING, K. J. AND PICKERING, F. B., 1960, The tempering characteristics of low carbon, low alloy steels, *J.I.S.I.*, **194**,
12. KENNEFORD, A. S., 1958, The effect of some common alloying elements on the Volume change at  $A_{c3}$  of a 0.35% carbon steel, *J.I.S.I.*, **188**,
13. KURDJUMOV, G. V., 1960, Phenomena occurring in quenching and tempering of steels, *J.I.S.I.*, **194**,
14. SWINDEN, X., 1913, A study of the constitution of carbon molybdenum steels, *Carnegie Scholarship Memoirs*, **5**.

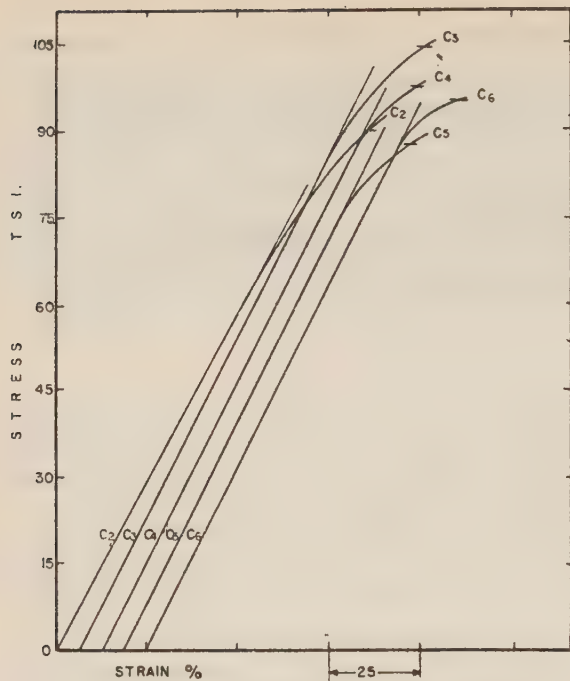


FIG. 1.- STRESS STRAIN CURVES OF STEEL 'C'

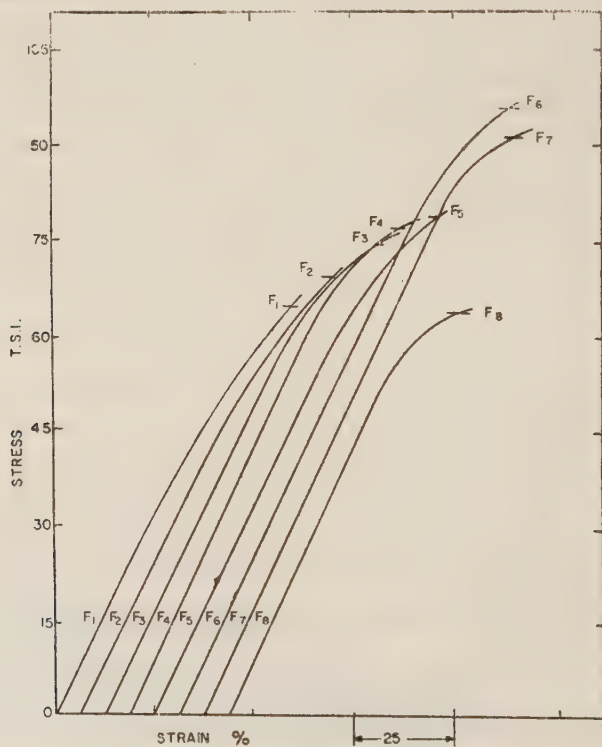


FIG. 6.- STRESS STRAIN CURVES OF STEEL 'F'



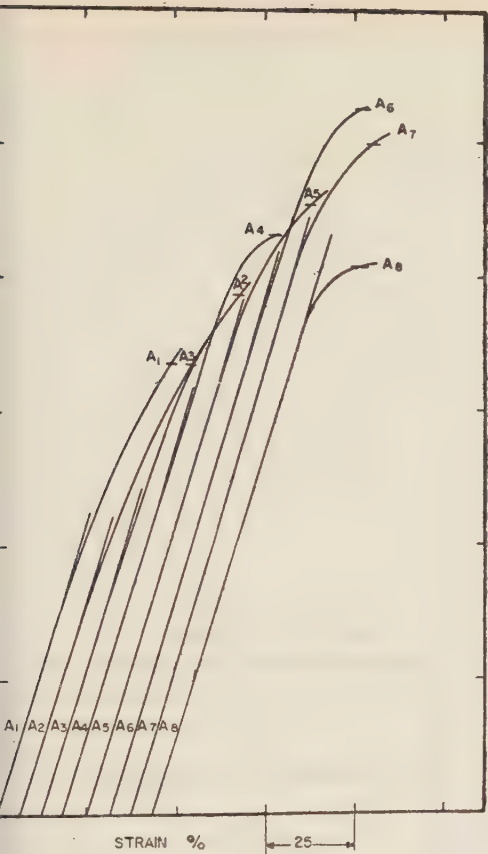


FIG. 7. - STRESS STRAIN CURVES OF STEEL 'A'

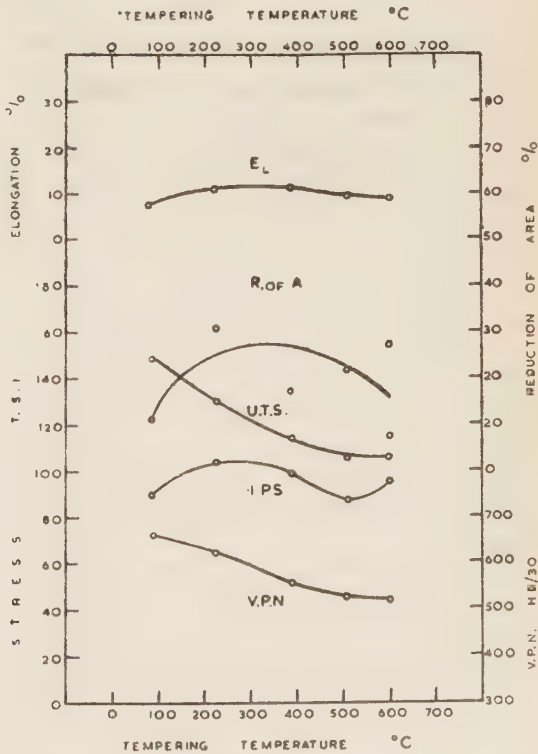


FIG 9 - AVERAGE MECHANICAL TEST RESULTS OF STEEL 'C'

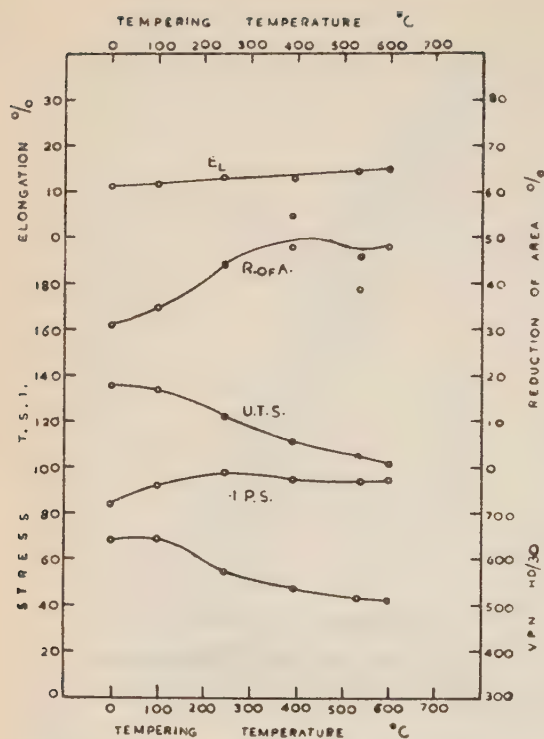


FIG.10—AVERAGE MECHANICAL TEST RESULTS OF STEEL 'Q'.

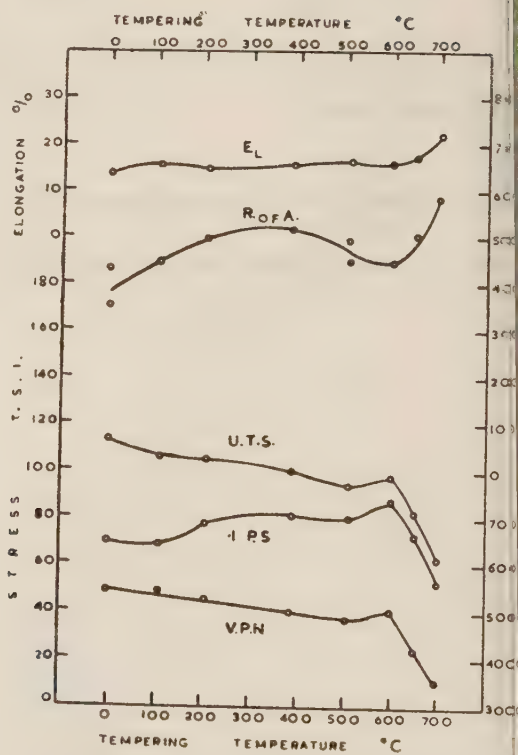


FIG.13—AVERAGE MECHANICAL TEST RESULTS OF STEEL 'E'.

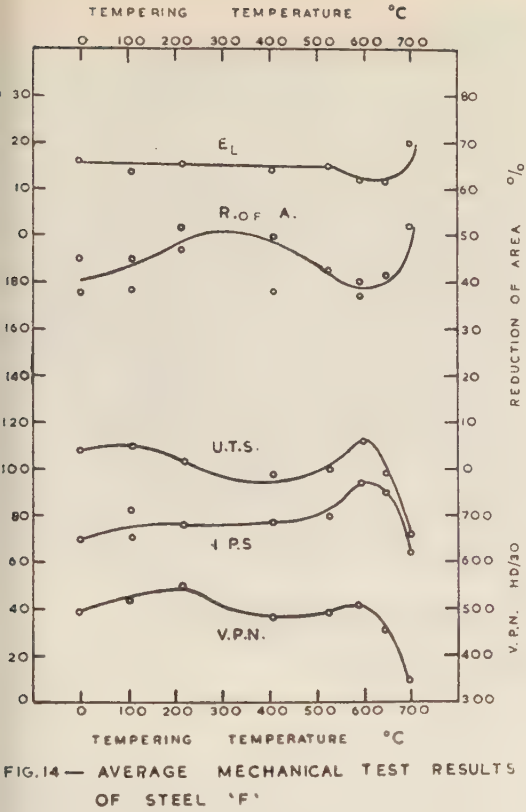


FIG.14— AVERAGE MECHANICAL TEST RESULTS OF STEEL 'F'

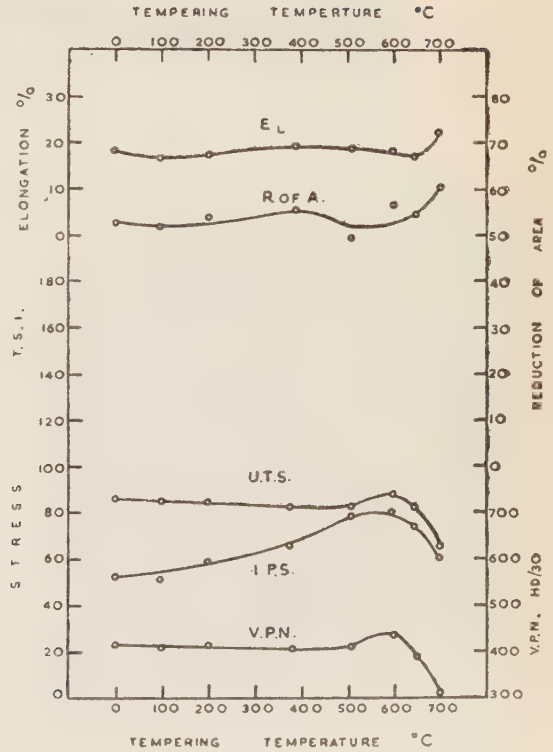


FIG 15— AVERAGE MECHANICAL TEST RESULTS OF STEEL 'A'.

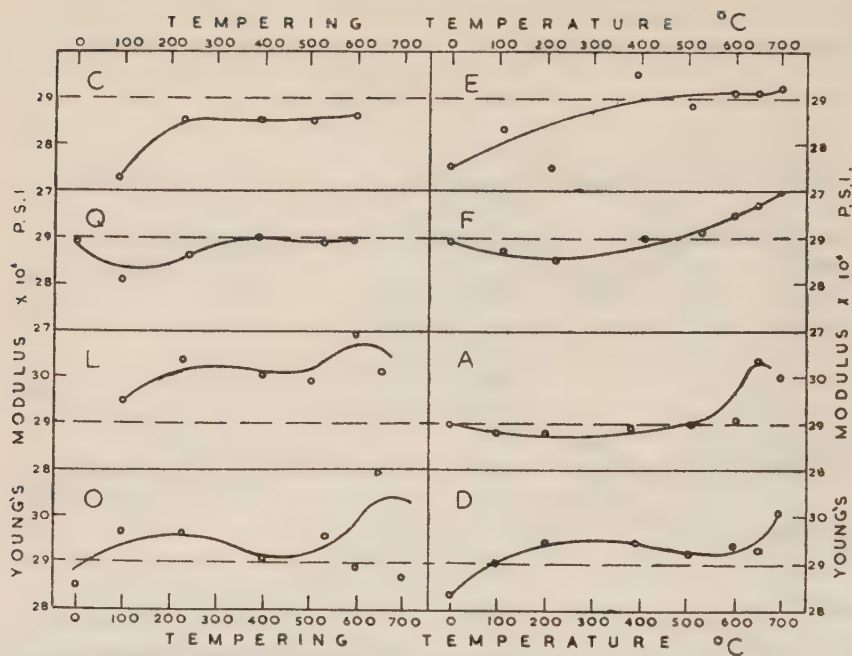


FIG.17—YOUNG'S MODULUS VERSUS TEMPERING TEMPERATURE





Plate No. 1  
 $A_5 \times 250$ . T—505 °C



Plate No. 2  
 $F_1 \times 250$ . As W.Q.

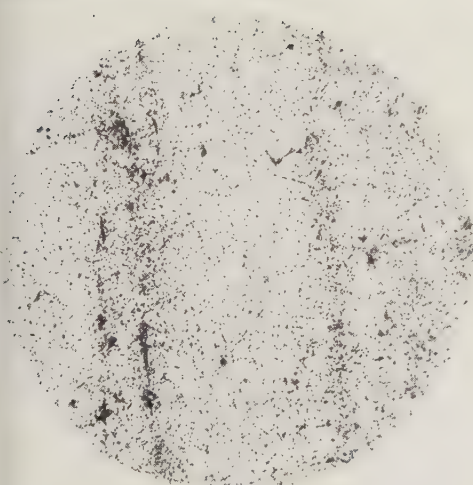


Plate No. 3  
 $F_6 \times 250$ . T—600 °C

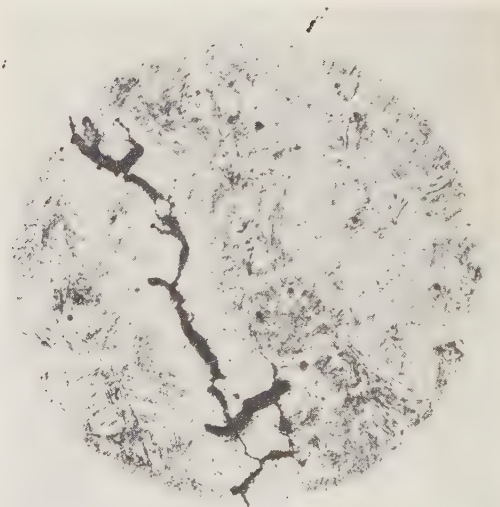


Plate No. 4  
 $Q_3 \times 250$ . T—245 °C

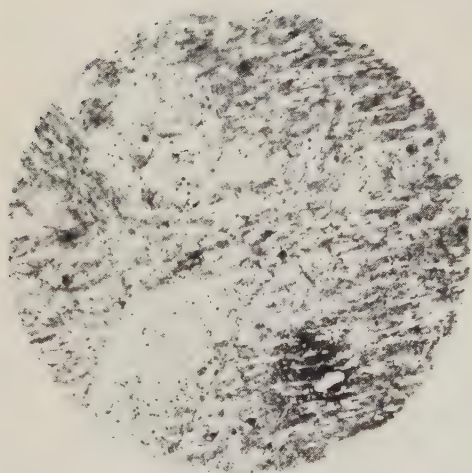


Plate No. 5  
 $C_2 \times 750$ . T—87 °C

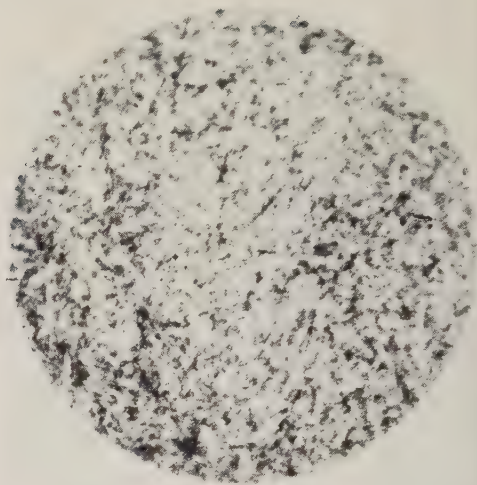


Plate No. 6  
 $C_6 \times 750$ . T—600 °C

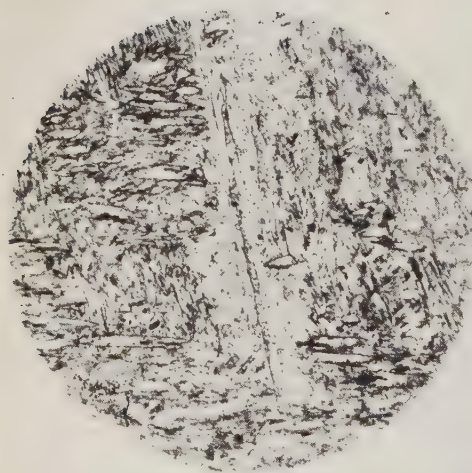


Plate No. 15  
 $E_1 \times 750$ . As W.Q.

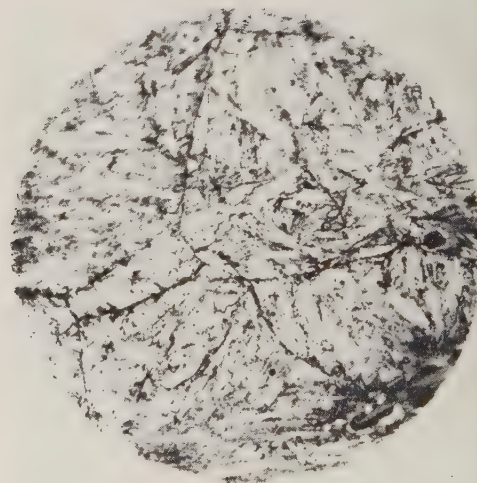


Plate No. 16  
 $E_6 \times 750$ . T—600 °C

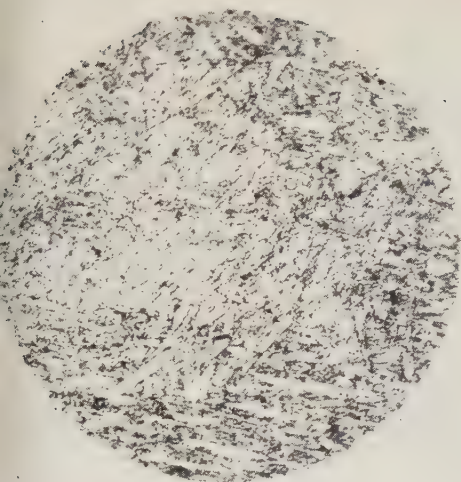


Plate No. 17  
 $E_8 \times 750$ . T—700 °C

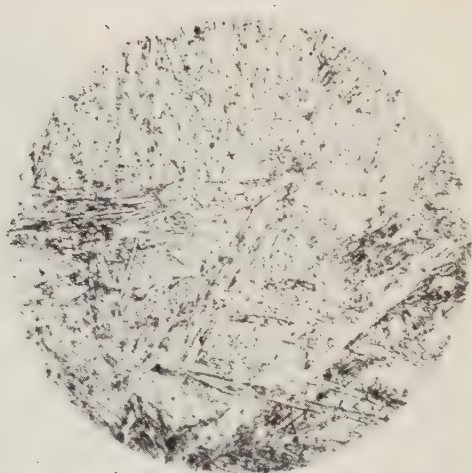


Plate No. 18<sup>1</sup>  
 $F_1 \times 750$ . As W.Q.

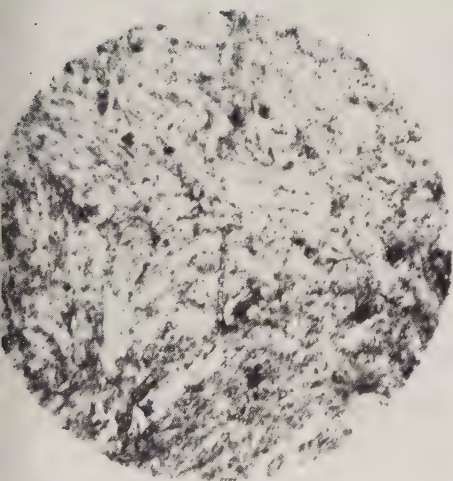


Plate No. 19  
 $F_6 \times 750$ . T—600 °C

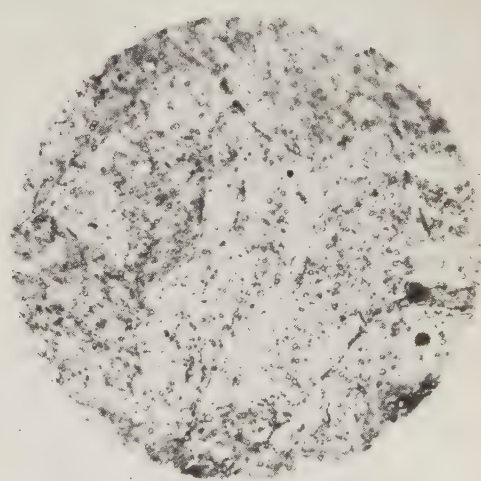


Plate No. 20  
 $F_7 \times 750$ . T—650 °C



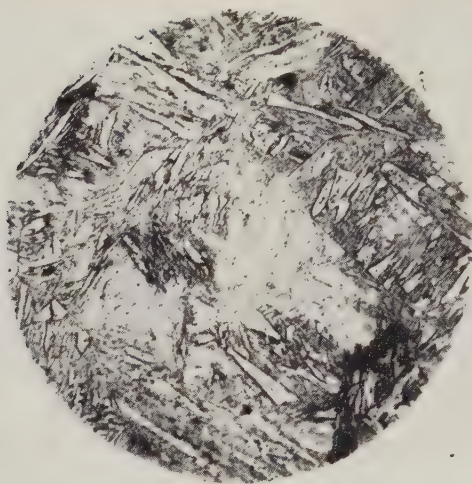


Plate No. 21  
 $A_1 \times 750$ . As W.Q.

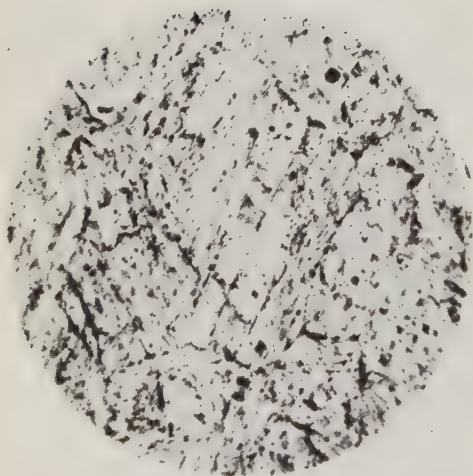


Plate No. 22  
 $A_6 \times 750$ , T—600 °C

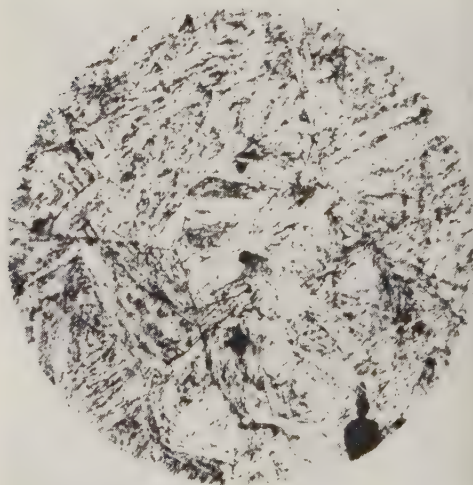


Plate No. 23  
 $A_8 \times 750$ , T—700 °C



# PRELIMINARY DEVELOPMENT OF AN ANNULAR JET INJECTOR

A. KOGAN AND M. VICTOR

*Department of Aeronautical Engineering, Technion-Israel Institute of Technology, Haifa*

## ABSTRACT

The paper describes research carried out at the Department of Aeronautical Engineering on an injector designed for operating the Department's transonic wind tunnel. Experiments were carried out in the low and high-subsonic ranges with a view to determining the influence of the injector components on its performance, using mixing tubes of variable length and two different diffusers.

It was established that optimum mixing tube length ranges from  $L_m/D_m = 2.5$  to 4 and that a  $4^\circ$  diffuser permits improvement of performance. It was also found that the performance level of the injector in question is lower than those of similar systems described in references. This may be attributed to the negative influence of the transition piece between the rectangular and circular sections, separation of the secondary flow before the injection area and the geometry of the injection slot.

Suggestions for improvement of performance are given.

## 1. INTRODUCTION

The experimental transonic wind tunnel (Figure 1) operates on the induction principle, consisting in the injection of high-pressure air (inducing air, or primary flow) into a channel in the direction of flow required for the induced air (secondary flow). As a result of the mixing process, momentum is imparted to the induced air and the desired flow is obtained. Injection may be central or peripheral (Figure 2); in most cases the latter method yields better results.

In wind tunnels, injection is effected downstream of the test section in order to preclude interference with the secondary flow. The smallest cross section of the inducing air nozzle (injection slot) is normally located in the injection area. Although a sonic velocity is obtainable in the slot when the stagnation pressure of the primary flow (blowing pressure) is about double the static pressure in the injection section, it is usually advantageous to use a higher blowing pressure. While this would not produce a higher velocity in the slot, it increases the density of the primary flow and hence the momentum imparted to the induced air. The same consideration holds if the minimum cross section is located before the injection area.

Injector performance may be evaluated by measuring the ratios  $p_{oj}/p_{oi}$  of the blowing pressure and secondary-flow stagnation pressure required for obtaining a given flow at Mach number  $M_i$  in the test section and  $m_i/m_j$  of the respective rates of mass flow. The performance level rises with increasing mass ratio and, conversely with decreasing pressure ratio for a given mass ratio and Mach number.

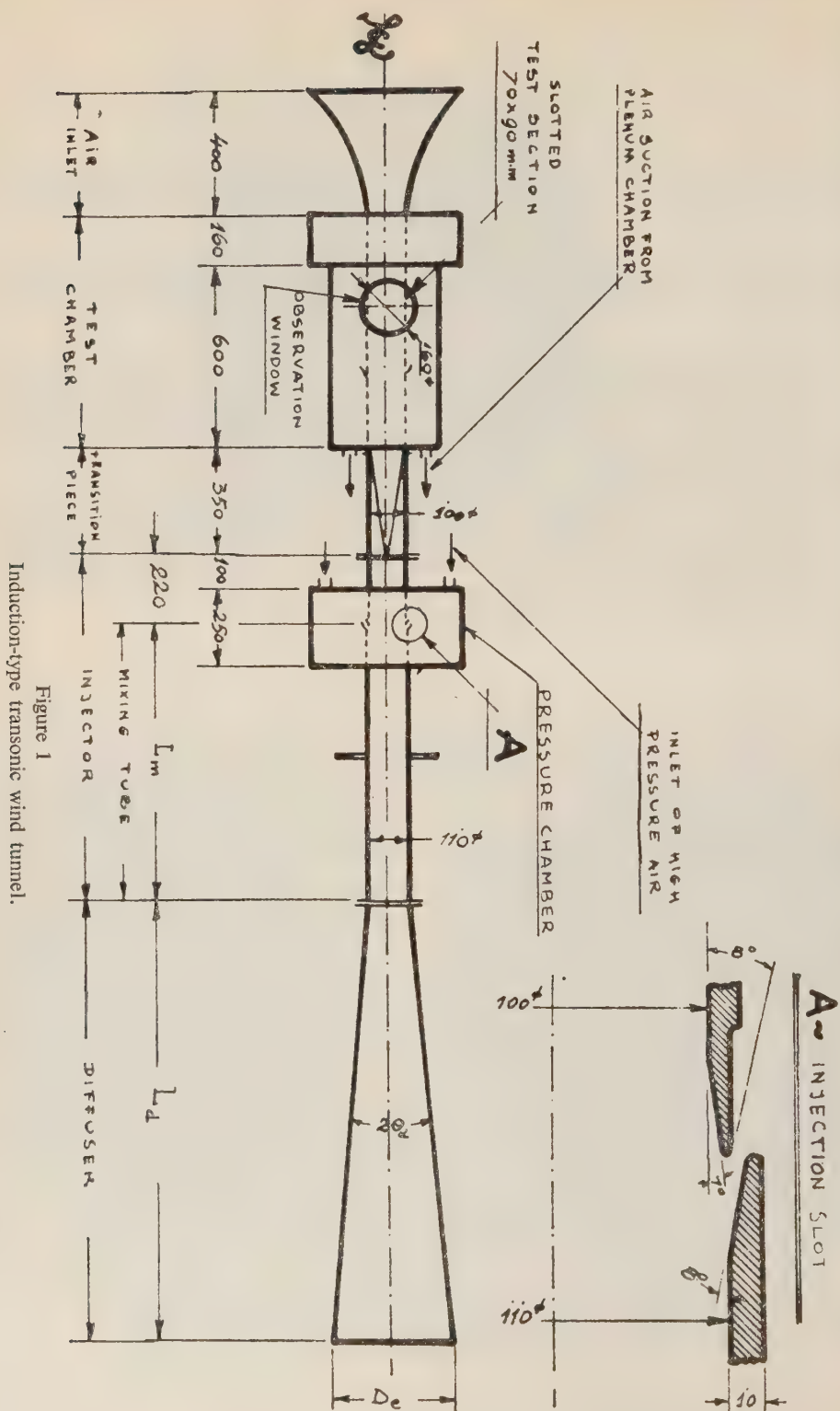


Figure 1  
Induction-type transonic wind tunnel.

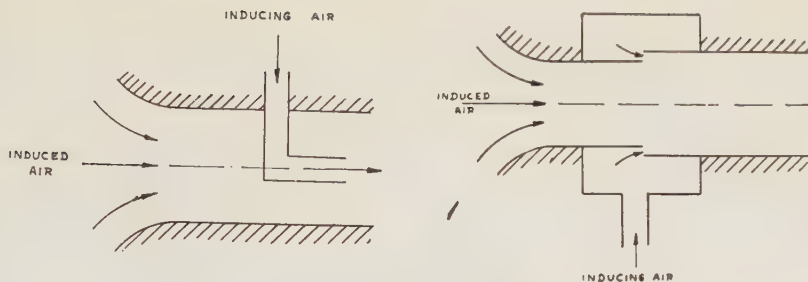


Figure 2  
Different ways of injection

The suitability of the induction system for the operation of wind tunnels was studied in a number of laboratories<sup>1-8</sup>. In the low subsonic range, the blowing pressure required is low and the mass ratio very high, but the induction method is impracticable in view of the large storage capacity required for the inducing air at low pressures. In the supersonic range, above  $M > 1.5$  in the test section, the blowing pressure is very high and the mass ratio decreases rapidly, so that the induction method is impracticable in this case as well. In the transonic range, however, the method was found practicable. The blowing pressure required for obtaining transonic velocities is not too high and the mass ratio range is reasonable.

## 2. DESCRIPTION OF INJECTOR AND HIGH-PRESSURE AIR SUPPLY SYSTEM

The injector in question is of circular cross section and injection section diameter of 110 mm. The advantage of the circular cross section lies in the simplicity of its design<sup>3,4</sup>. The test chamber, i.e. the minimum effective cross section area (see §5), is rectangular, dimensions  $69 \times 89$  mm. A transition piece from rectangular to circular cross section is interposed between the chamber and the injector. The injector, designed for open-circuit experiments, is shown in Figure 3 with a conical diffuser attached at its exit.

The supply of inducing air to the pressure chamber is effected from tanks through valve  $V$  and a 1" pipe. A throat  $p^*$  is fitted in the pipe for regulating the inducing air mass. After the throat, the pipe branches out providing two 1" inlets for the high-pressure air (Figure 4).

### 2.1 Construction

The air inlet  $A$  (design following Ref. 9) is made of sheet steel, and has a convergence ratio of 40:1. The transition piece  $B$  is made of aluminium casting, with a  $70 \times 90$  mm end attached to the air inlet. These are also the dimensions of the test chamber to be interposed between the air inlet and the transition piece. These dimensions ensure condensation-free flow in the transonic range<sup>10,11</sup>. This part comprises a gradual transition from rectangular to circular cross section of

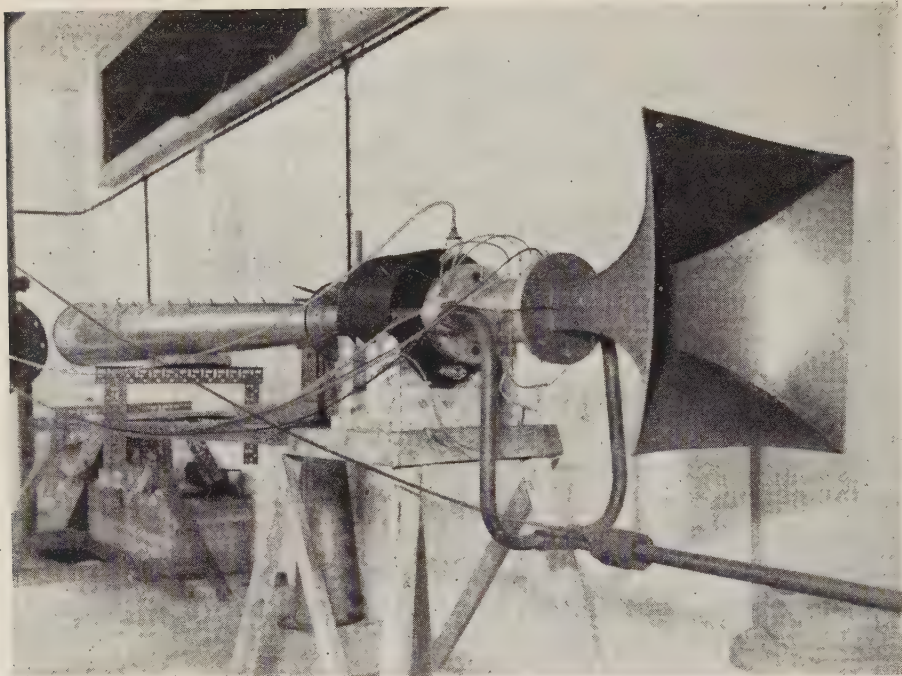


Figure 3  
Injector

100 mm diameter. In order to preclude choking of the secondary flow in the transition piece<sup>3</sup> or near the injection slot<sup>3,7</sup>, a 1.24 area-ratio was adopted for the circular and rectangular cross sectional areas. Since this part is in effect a diffuser, its total opening angle does not exceed  $6.5^\circ$ .

*C* is a fixed steel tube of 100 mm internal diameter and *E*, screwed into *D*, a similar tube of 110 mm internal diameter, this variation of diameter being an additional precaution against undesirable choking of the secondary flow<sup>3,7</sup>. The gap between parts *C* and *E* comprises the variable injection slot (Detail A, Figure 1). The slot is designed for continuous adjustment by rotating *E* with respect to *C* with the aid of handles *M*. The shape and dimensions of the slot provide for a 0–3 mm width range against a 25 mm horizontal displacement of *E*, ensuring sonic velocity in the slot and a constant injection angle of  $8^\circ$  between slot and injector axes.

Since in the case of peripheral injection perfect slot symmetry is essential, special attention had to be paid to precision in manufacture of the slot with respect to the concentricity of parts *C*, *D* and *E*. The total angle of conical transition from the 100 mm diameter of part *C* to the 110 mm of part *E* was  $14^\circ$ .



The primary flow enters the annular pressure chamber  $D$ , designed for a blowing pressure of about 40 atm, through pipes  $P$ , and then part  $E$  through the injection slot. The secondary flow follows a path through the air inlet  $A$ , transition piece  $B$  and tube  $C$ , and meets the primary flow in a mixing tube consisting of parts  $E$  and  $F$  (Figure 4). This mixing tube has a constant diameter of 110 mm and its length is adjusted by varying the attachment  $F$ , providing a range of length-to-diameter ratios between 4 and 10. The  $F$  pieces are fitted with conical diffusers  $G$  with the required angle and area expansion ratio.

### 3. MEASUREMENTS AND INSTRUMENTATION

Evaluation of injector performance requires the following data:

Mach number in the test section, blowing pressure, primary and secondary rates of discharge and cross sectional area of the slot, as well as the static pressure distribution along the injector and stagnation pressure distribution at the mixing tube (or diffuser) exit.

#### 3.1 *Velocity measurement in the test chamber*

The Mach number in the test chamber was determined by measuring the mean static pressure at the four walls of the chamber (pressure taps  $i$ , Figure 4). Assuming that the stagnation pressure in the chamber equals the atmospheric pressure

$$M_i = \left\{ \frac{2}{\gamma - 1} \left[ \left( \frac{p_{oi}}{p_i} \right)^{\frac{\gamma-1}{\gamma}} - 1 \right] \right\}^{\frac{1}{2}} \quad (1)$$

Static and atmospheric pressures were measured by means of a Collesman manometer.

#### 3.2 *Blowing pressure measurement*

Since the ratio of the pressure chamber and slot areas is 70 for a maximum slot opening and increases with decreasing slot area, the static pressure measured at the chamber wall closely approximates the stagnation pressure. This pressure is read by means of a Bourdon gauge.

#### 3.3 *Primary discharge measurement*

The primary rate of discharge can be measured by two methods: (a) by determining the stagnation pressure, throat area and stagnation temperature in the high-pressure air pipes (Figure 4), assuming that the flow in the throat is sonic; or (b) by determining the same data in the pressure chamber on the same assumption for the slot. In both cases the rate of discharge is given by Eq. (2), assuming further that flow from the stagnation point is isentropic and the discharge coefficient ( $k_p^*$  or  $k_j$  respectively) is 1.

$$m = \frac{p_0 A^*}{\sqrt{T_0}} \sqrt{\frac{\gamma}{R}} \left( \frac{2}{\gamma + 1} \right)^{\frac{\gamma+1}{2(\gamma-1)}} \quad (2)$$



In the first case the throat area ( $A_p^*$ ) is known and constant. The pressure measured before the throat ( $p_{op}$ ) is not the true stagnation pressure since at that point the velocity is not zero. The throat was proportioned so as to maintain sonic flow even at the minimum slot opening. The pressure measured at pressure tap<sub>op</sub> (Figure 4) is 0.994 of the stagnation pressure and readings should be corrected accordingly. At pressure tap<sub>p</sub> the static pressure of the inducing air is measured after the throat. The ratio of this static pressure and the stagnation pressure before the throat gives a rough indication of sonic flow in the throat. The mass ratio can be obtained accordingly with the aid of Eq. (2), for all cases where the  $p_p/p_{op}$  ratio is below the critical level (0.5283).

The stagnation temperature before the throat cannot be measured directly. It may be assumed, however, that it lies between those of the atmosphere (i.e. of the air in the tanks) and of the pressure chamber, which can be measured. The difference between these two is fairly small (10°C), so that it can be assumed that the stagnation temperature of the inducing air before the throat equals the atmospheric.

In the second case, the inducing air mass can be calculated with the aid of Eq. (2) if the blowing pressure is about double the atmospheric, ensuring sonic flow in the slot. The slot area ( $A_{jg}$ ) can be determined by measuring its width at minimum opening with the aid of standard-thickness shims and counting the number of half-turns of part *E* (Figure 4). The minimum area is  $\pi Ds_o$ . The slot width increment due to the displacement of part *E* is  $\Delta s = n/2 \times 1/16 \sin 8^\circ$ , where *n* is the number of half-turns (the number of threads per inch being 16 and the injection angle  $8^\circ$ , Figures 1 and 4). Hence, for a given *n*, the slot width is:

$$s = s_o + \Delta s \quad (3)$$

and the slot area:

$$A_{jg} = \pi Ds \quad (4)$$

### 3.4 Secondary discharge measurement

The induced air mass is given by

$$m_i = \frac{p_{oi} A_i}{\sqrt{T_{oi}}} \sqrt{\frac{\gamma}{R}} \frac{M_i}{\left(1 + \frac{\gamma - 1}{2} M_i^2\right)^{\frac{\gamma + 1}{2(\gamma - 1)}}} \quad (5)$$

$p_{oi}$  and  $T_{oi}$  being atmospheric pressure and temperature resp., and the discharge coefficient  $k_i = 1$ .

### 3.5 Determination of mass ratio

The mass ratio is given by

$$\left(\frac{m_i}{m_j}\right)_{A_p^*} = \frac{p_{oi} A_i}{p_{op} A_p^*} \left(\frac{\gamma + 1}{2}\right)^{\frac{\gamma+1}{2(\gamma-1)}} \frac{M_i}{\left(1 + \frac{\gamma-1}{2} M_i^2\right)^{\frac{\gamma+1}{2(\gamma-1)}}} \quad (6)$$

calculation being based on the stagnation pressure in the throat.

Alternatively, the mass ratio calculation can be based on the blowing pressure  $p_{oj}$ :

$$\left(\frac{m_i}{m_j}\right)_{A_j} = \frac{p_{oi} A_i}{p_{oj} A_j} \left(\frac{\gamma + 1}{2}\right)^{\frac{\gamma+1}{2(\gamma-1)}} \frac{M_i}{\left(1 + \frac{\gamma-1}{2} M_i^2\right)^{\frac{\gamma+1}{2(\gamma-1)}}} \quad (7)$$

### 3.6 Measurement of static pressure distribution along injector and stagnation pressure distribution at exit

For measuring the static pressures, taps were provided along the transition piece, mixing tube and diffuser. The stagnation pressures at the mixing tube or diffuser exit were measured with the aid of pressure rakes. All measurements were carried out with the aid of an alcohol multimanometer or mercury manometers, according to the range of pressure.

## 4. PRELIMINARY TESTS

The first test series was carried out with mixing tube No. 2 (length-to-diameter ratio 6) fitted with a conical diffuser with a total opening angle of  $8^\circ$  and area expansion ratio 8, designed in accordance with experimental results given in Ref. 2, 3, 5 and 6.

### 4.1 Location of test chamber

The test chamber is defined as the zone of lowest static pressure of the secondary flow. In order to locate this section, a series of pressure taps was provided at the end of the air inlet and along the transition piece (Figure 4). The injector was operated, for two slot widths at three different velocities of secondary flow. This velocity was determined for each width by adjusting the blowing pressure by means of valve  $V$ . Results (Figure 5) show that (a) the section of the lowest static pressure is about 60 mm from the transition piece inlet for all velocities of secondary flow; (b) flow in the transition piece is steady; (c) slot width has no influence on pressure distribution in the transition piece. This last indicates that the injection zone is sufficiently removed from the test chamber so that at subsonic velocities flow in the latter unaffected by the injection process.



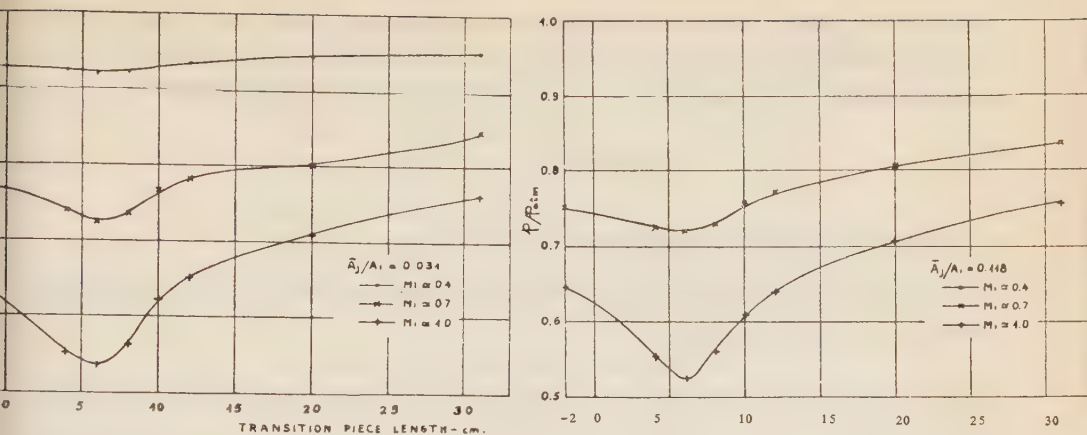


Figure 5

Pressure distribution along the transition piece as function of injection slot area and test section Mach number.

With the test chamber located as described above, four pressure taps were provided on its walls for measuring the mean static pressure. Separate measurements showed a maximum discrepancy of about 0.1" mercury between readings, i.e. within the limits of experimental error (accuracy  $\pm 0.05$ " mercury).

The Mach number in the chamber is determined by the average pressure  $p_i$  in this section.

## 5. EVALUATION OF INJECTOR PERFORMANCE

### 5.1 Procedure

For a given slot width determined by the number of half-turns of part *E*, the inducing air valve is opened so as to produce a static pressure corresponding to a desired value of Mach number  $M_i$ , see Eq. (1). Readings were taken for  $n = 0, 0.5, 1, 2, 3, 4, 5, 7, 10, 15, 20, 25$ , and for a Mach number range from 0.4 to 1 at intervals of 0.1.

### 5.2 Determination of "aerodynamic" slot area

As explained in §3.3, one of the principal factors governing injector performance is the slot section area. Measurement of the initial width  $s_0$  by means of standard shims entails a relative error ranging from 20% for  $n = 0$  to 5% for  $n = 15$ . Since the slot area is a parameter of the performance curve<sup>1-7</sup>, the latter cannot be plotted unless this error is minimised. One means of achieving this is "aerodynamic" measurement of the section area. It can be assumed with fairly close accuracy that flow in the inducing air supply pipe is one-dimensional with normal shock wave, involving no other losses between the throat  $p^*$  and the slot  $j$ . Hence, with sonic flow in both throat and slot, we have

$$p_{op} A_p^* = p_{oj} A_j \quad (8)$$

For each given  $n$ , corresponding stagnation pressures before the throat and the slot were obtained for different Mach numbers in the test chamber. Since the throat area is known, the slot area can be calculated for each case with the aid of Eq. (9)

$$A_j [\text{sq.in.}] = 0.1028 \frac{P_{op}}{P_{oj}} \quad (9)$$

in which  $A_p^* = 0.1028 \text{ sq.in.}$  is the throat area.

The mean "aerodynamic" area for each  $n$ , together with the corresponding mean deviation, is given in Table I.

TABLE I.

Mean "aerodynamic" area for mixing-tube of length-to-diameter ratio 6,  $8^\circ$ -diffuser of area expansion ratio 8.

$n$	$\bar{A}_j$	$\bar{\delta}_1 \times 10^3$	$\bar{\delta}_1 / \bar{A}_j$
Half-turns of part E	"Aerodynamic" mean area	Mean deviation	%
* 0	0.170	—	—
* 0.5	0.199	—	—
1	0.228	2.72	1.13
2	0.289	6.45	2.10
3	0.360	3.95	1.09
4	0.424	4.22	1.00
5	0.490	3.50	0.71
7	0.619	1.90	0.31
10	0.806	9.25	1.15
15	1.118	9.00	0.80
20	1.426	31.	2.20
25	1.730	—	—

\* Calculated by extrapolation from Figure 6.

The area, calculated by means of direct geometric measurement as explained in §3.3, is plotted against  $n$  in Figure 6, giving the result of the preliminary series. The diagram shows that the "aerodynamic" value ( $A_j$ ) is always higher than the one obtained geometrically ( $A_{jg}$ ), the maximum deviation not exceeding 2%; hence the error entailed in direct measurement is systematic and the mean "aerodynamic" area can be assumed as the actual slot area.

Since for small openings ( $n < 1$ ) the flow in the throat was not sonic, as expected (see §2.1 and §3.3),  $A_j$  was not calculated with the aid of Eq. (9), but determined by extrapolation of the curve in Figure 6. The final "aerodynamic" area was determined as the mean of the complete series of experiments. It is presented in Table II.

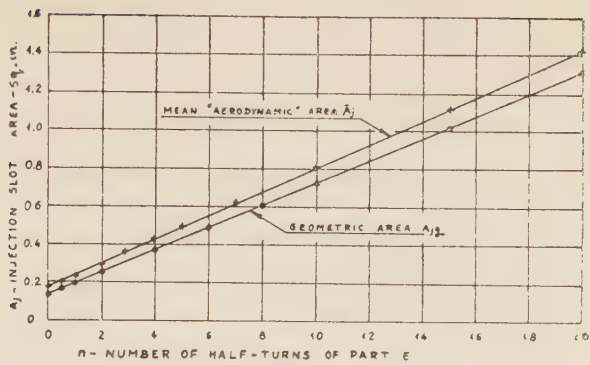


Figure 6

Injection slot area. Results based on geometric and aerodynamic calculations. Measured initial slot width  $S_0 = 0.098$  in;  $8^\circ$  diffuser.

TABLE II.  
Mean "aerodynamic" area, based on complete series

$n$ Half-turns of part E	0	0.5	1	2	3	4	5	7	10	15	20	25
$\bar{A}_j$ , sq. in.	0.172	*0.201	0.225	0.295	0.364	0.430	0.495	0.621	0.808	1.121	1.435	1.730
$\bar{A}_j/A_i$	0.018	0.021	0.024	0.031	0.038	0.045	0.052	0.065	0.085	0.118	0.150	0.182

\* Calculated by extrapolation.

5.3 Determination of pressure ratio

In all tests the stagnation pressure of the induced air was equal to the atmospheric. Results given in Figure 7, show the pressure ratio for the original injector (mixing tube length-to-diameter ratio 6;  $8^\circ$  diffuser). It is about 100% higher than that of the best similar system reported in the references<sup>2,3</sup> for small slot openings, and about 50% higher for the larger openings (Figure 8). For simplicity, the diagram is confined to the Mach number extremes of 0.4 and 1.0, but the same applies for the entire range.

5.4 Determination of mass ratio

The mass ratio was calculated with the aid of Eq. (6) and (7). Results (Figure 9) show complete agreement between the two methods of calculation for  $\bar{A}_j/A_i \geq 0.04$  and  $M_i > 0.5$ . For lower Mach numbers and smaller openings, the discharge coefficient  $k_j$ , not allowed for in Eq. (7), deviates considerably from 1<sup>5</sup>. It was also found that for  $\bar{A}_j/A_i < 0.024$  flow in the throat is not choked, so that results based on Eq. (6) are no longer accurate for this range.

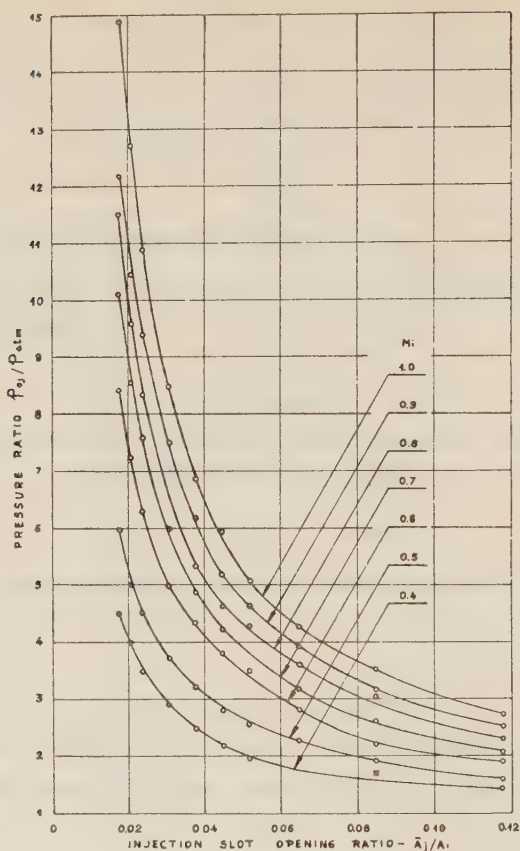


Figure 7

Blowing pressure as function of slot area and test section Mach number. Injector with  $8^\circ$  diffuser of area expansion ratio 8 and mixing tube of length-to-diameter ratio 6.0.

Figure 10 shows part of the results given in Figure 9 compared with corresponding results given in Ref. 2. For small openings, the mass ratio obtained in the present experiments is 50% lower than the corresponding ratio in Ref. 2, and for the larger openings—25% lower. Since the overall limit of accuracy does not exceed 6%, this discrepancy cannot be attributed to limitations of the measurement technique but to increasing losses in the system in question.

## 6. INFLUENCE OF INJECTOR COMPONENTS

### 6.1 Transition piece

A divergent transition piece causes an average reduction of about 10% in performance level, in both the subsonic and supersonic ranges<sup>2,3</sup>. With the transition piece used in the present experiments higher losses should not be expected, since in the range in question there is no separation of flow (Figure 5).



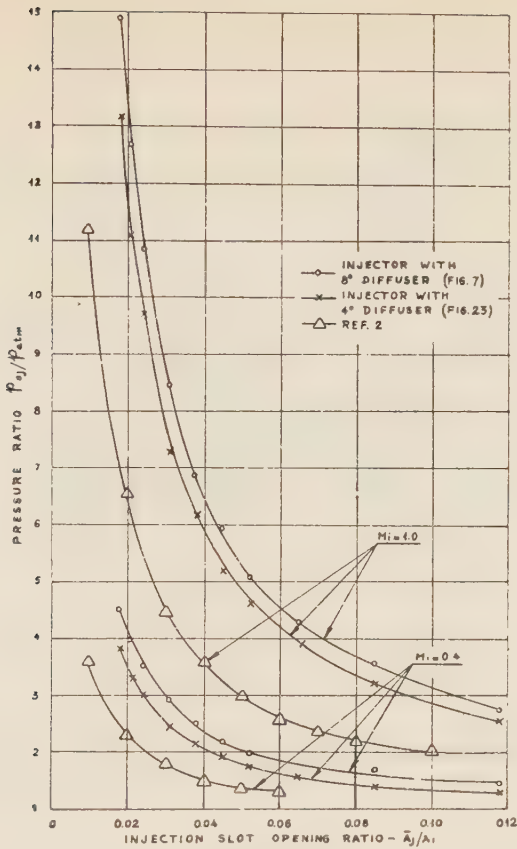


Figure 8

Blowing pressure as function of slot area and test section Mach number for different injectors.

6.2 Divergent section between part C and injection section

Table III shows the static pressure in section *a* before the slot (Figure 4) for different Mach numbers. The effective diameter of this section was calculated with the aid of one-dimensional Flow equations. The values obtained are 5% to 10% lower than the geometric diameter of 110 mm, indicating separation of the flow before this section. Considering that the total opening angle of this section is 14° (see

TABLE III  
Effective diameter of secondary flow in injection section

$M_i$	$P_a/P_{atm}$ Mean of complete series	$M_a$	$\frac{A_a}{A^*}$	$\frac{A_a}{A_i} = \frac{A_a/A^*}{A_i/A^*}$	$A_a$ mm <sup>2</sup>	$D_a$ mm
0.4	0.948	0.277	2.19	1.38	8480	104.0
0.7	0.871	0.448	1.45	1.32	8100	101.5
1.0	0.815	0.548	1.26	1.26	7750	99.4

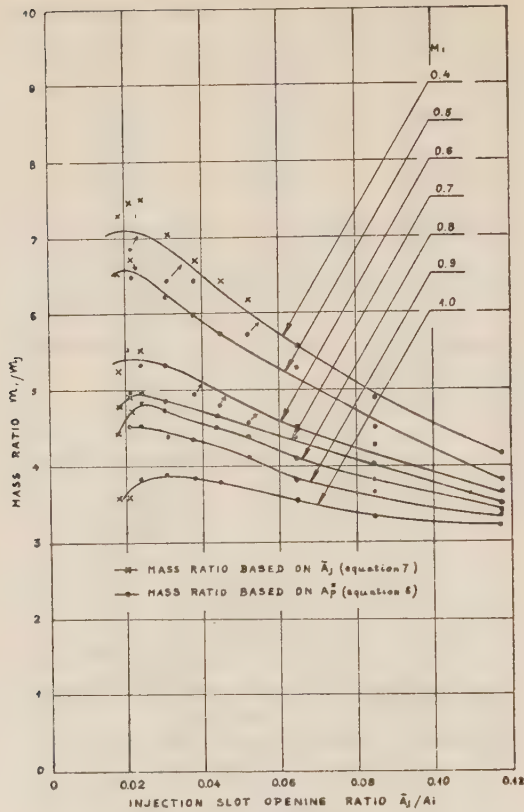


Figure 9

Mass ratio as function of slot area and test section Mach number. Injector with  $8^\circ$  diffuser of area expansion ratio 8 and mixing tube of length-to-diameter ratio 6.0

§2.1), it can be assumed that for a smaller angle, performance will be improved considerably.

### 6.3 Injection slot

#### 6.3.1 Injection angle

Experimental results<sup>3</sup>, show that this angle has almost no effect on performance, if smaller than  $10^\circ$ . This includes the present series, in which the angle was  $8^\circ$ .

#### 6.3.2 Shape of slot

The slot, as shown in Figure 1, comprises a long stretch of constant cross section. For small openings the length-to-width ratio is 40, so that a pressure drop can be expected. This drop, calculated with the aid of one-dimensional flow equations allowing for friction, ranges from 1% to 6% according to opening. Minimising this loss necessitates a modified shape as shown in Figure 11, with a reduced effective length-to-width ratio.

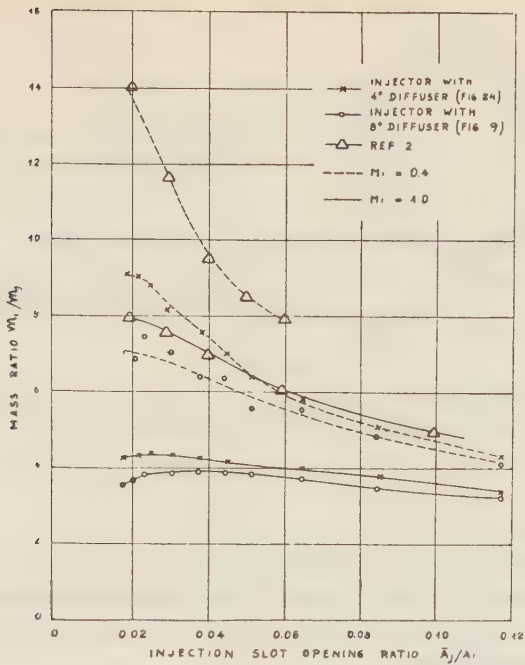


Figure 10

Mass ratio as function of slot area and test section Mach number for different injectors.

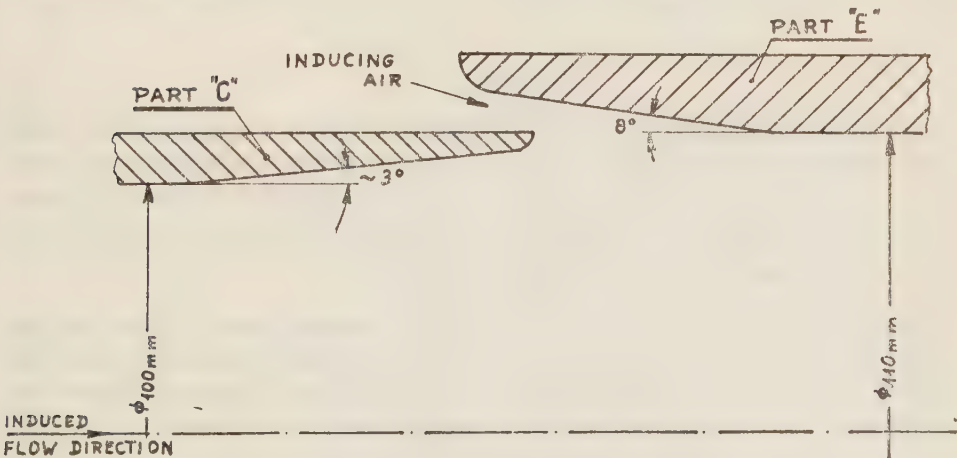


Figure 11

Cross section of proposed injection slot

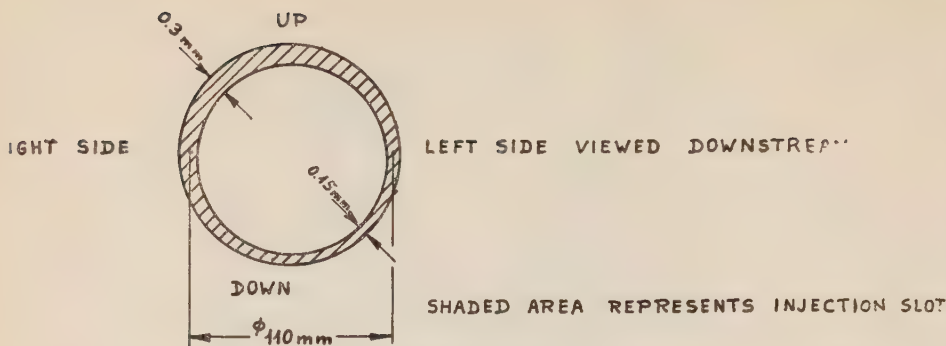


Figure 12

Peripheral distribution of actual injection slot width, as determined by geometric measurement. Injection slot opening ratio 0.018 ( $n = 0$ )

### 6.3.3 Non-symmetry

The stagnation pressure distribution at the exits of the various mixing tubes (Figure 13) and diffuser (Figure 14) show that the flow is non-symmetrical with respect to the injector axis. This non-symmetry is especially pronounced for small slot openings, irrespective of blowing pressure.

The width of the slot was measured at different points along its circumference by means of standard shims, showing a deviation from symmetry of about 0.2% (Figure 12). The effect of this non-symmetry on injector performance was studied in Refs. 2 and 3. The loss in blowing pressure due to this 0.2% deviation should not exceed 6% for an opening ratio of about 0.04.

## 6.4 Mixing tube

The longer the mixing tube, the more complete the mixing process, and the higher the momentum imparted to the induced air. Above a certain optimum length, however, the momentum increment is smaller than the loss due to increased friction.

In order to determine the optimal length of mixing tube, a series of experiments was performed with the mixing tubes listed in Table IV.

In all tests the static pressure distribution was measured along the tube, with the diffuser attached and without it. Where no diffuser was used, the pressure was found equal to the atmospheric near the point  $x_m/D_m = 4.5$ ; it rose further along an additional stretch of the tube and eventually dropped again to atmospheric level (Figure 15). The corresponding mass ratios are given in Figure 20.

With the diffuser attached, the maximum pressure point was shifted backwards to about  $x_m/D_m = 2.5$  for an  $8^\circ$  diffuser (Figure 17) and to  $x_m/D_m = 4$  for a  $4^\circ$  diffuser (Figure 19). The corresponding blowing pressures and mass ratios are



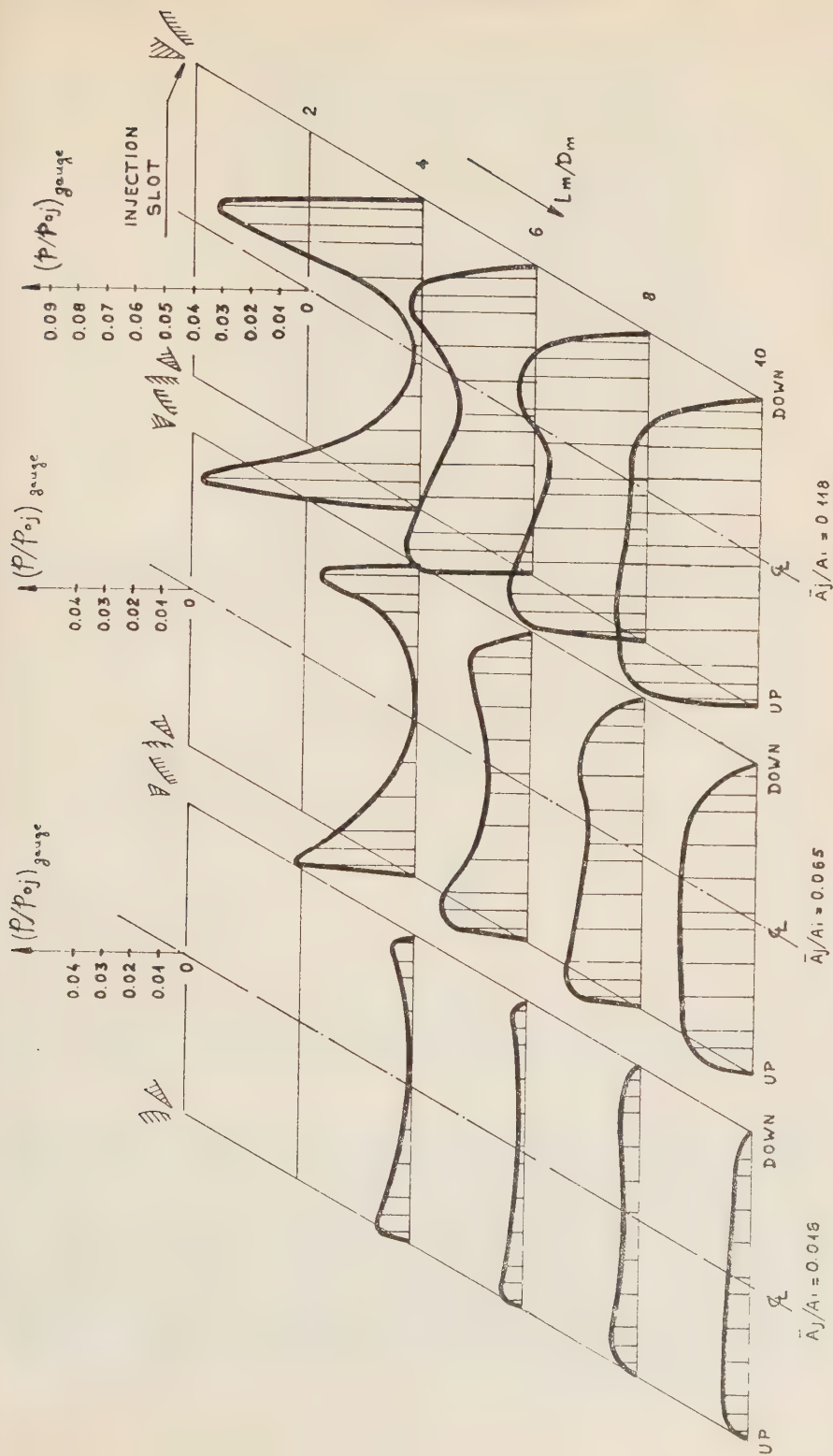


Figure 13

Stagnation pressure distribution along vertical tube exits, for different opening ratios of injection slot.  $P_{0j} = 20$  psig.

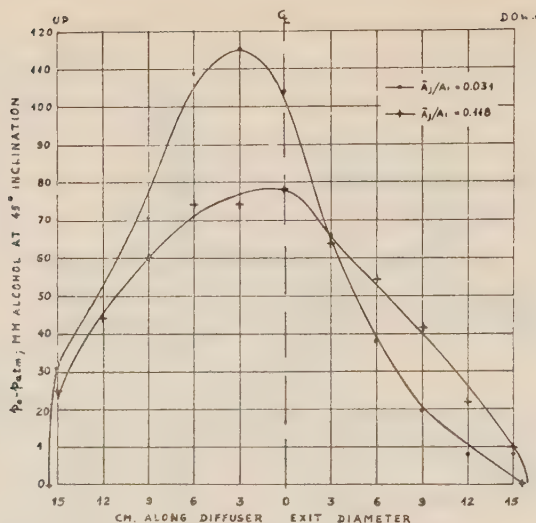


Figure 14

Stagnation pressure distribution at diffuser exit along vertical diameter for  $M_i = 1.0$ ,  $4^\circ$  diffuser of area expansion ratio 8.

TABLE IV  
Mixing tube data

Serial No.	Length $L_m$ (cm)	Length to diameter ratio $L_m/D_m$
1	44	4
2	66	6
3	88	8
4	110	10
2'	63	5.7
3'	80	7.3
4'	99	9.0

given in Figures 21 and 22, respectively. It can be concluded that, for the injector in question, the optimum mixing-tube length-to-diameter ratio ranges from 2.5 to 4.

The problem of optimum mixing-tube length was also studied in Refs. 5 to 6. According to Ref. 5, the optimum ratio for an annular injection system without a diffuser is about 5, while according to Ref. 6, the optimum ratio for a central system with a diffuser is 6.25. The fact that the former requires a shorter tube is due to the larger initial contact surface between inducing and induced air. It is assumed that

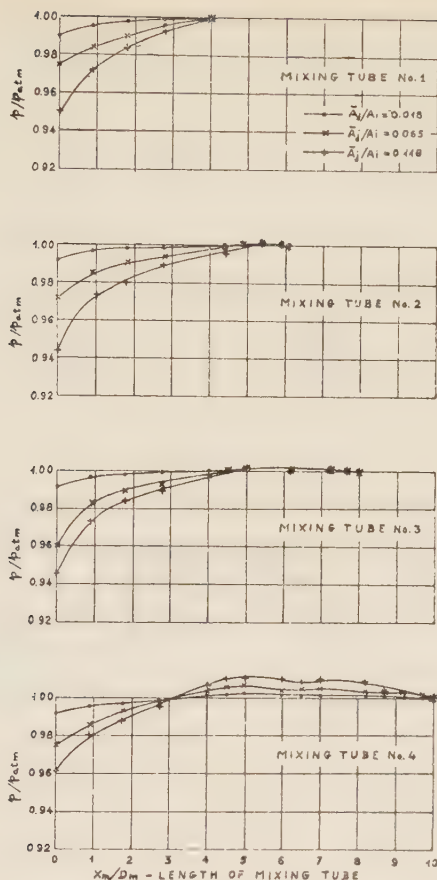


Figure 15

Static pressure distributions along mixing tubes.  $P_{oj} = 20$  psig. Injector without diffuser.

the irregularity of the secondary flow before the injection section, due to its separation in the transition piece between *C* and *E* (see §6.2) is a contributing factor to the acceleration of the mixing process in the experiments described here.

### 6.5 Diffuser

The static pressure distribution along the  $8^\circ$  diffuser with an area expansion ratio of 8 (Figure 16) indicates separation of the flow in all tests. This is also indicated by the stagnation pressure distribution at the diffuser exit. The flow separation zone (Figure 18) coincides with the section segment in which the air velocity at the mixing tube exit is lower (Figure 13).

In Figure 17, the static pressure distributions for both diffusers attached to mixing tube No. 2, are compared with the pressure distribution calculated by one-di-

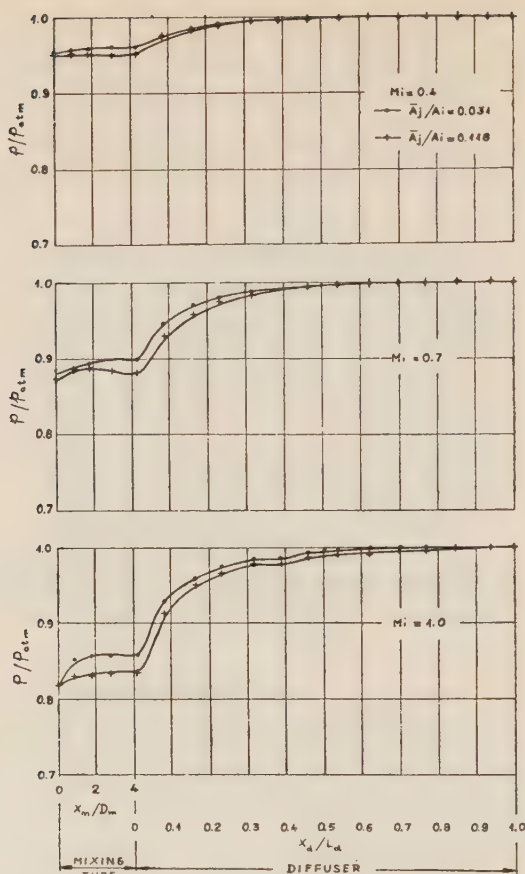


Figure 16A

Static pressure distribution along mixing tube No. 1 and  $8^\circ$  diffuser of area expansion ratio 8.

dimensional incompressible flow theory. This comparison permits location of the flow separation zone for the diffuser with the  $8^\circ$  opening angle. No appreciable separation was detected in any of the  $4^\circ$  diffuser tests.

The  $4^\circ$  diffuser permitted an average 12% improvement in pressure and mass ratios (Figures 8, 10, 23 and 24, Table V).

## 7. SUMMARY AND CONCLUSIONS

The conclusions drawn from the tests described above are as follows: An increase in mixing-tube length above  $L_m/D_m = 2.5$  or 4 respectively leads, in all cases, to a reduction in performance level. Elimination of the flow separation in the diffuser by reducing its opening angle results in improved performance. Pressure distribution along the mixing-tubes and diffusers is unaffected by slot width.



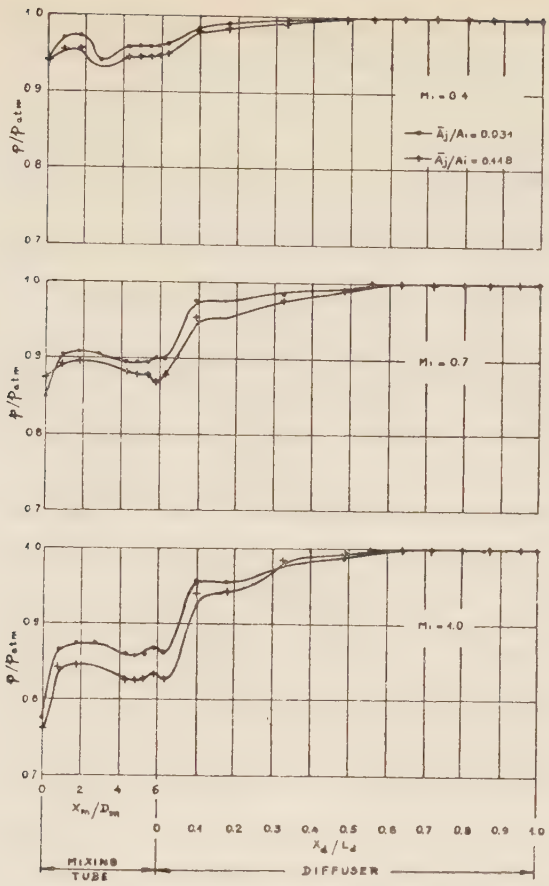


Figure 16B

Static pressure distribution along mixing tube No. 2 and 8° diffuser of area expansion ratio 8

The best performance level in the present tests was found to be 60% below those reported in Refs. 2 and 3 for low slot opening ratios. Even with the higher opening ratios, a difference of about 20% was still found. The main cause is believed to be separation of the secondary flow before the injection section. It is expected that a reduced opening angle in part C will lead to considerable improvement.

Additional loss factors are the presence of the transition piece between the rectangular and circular sections, imperfect symmetry and high primary flow friction in the slot. In future tests within the framework of this study, the system will be modified in the light of these conclusions. It is also proposed to study the effect of the diffuser inlet shape and area expansion ratio.

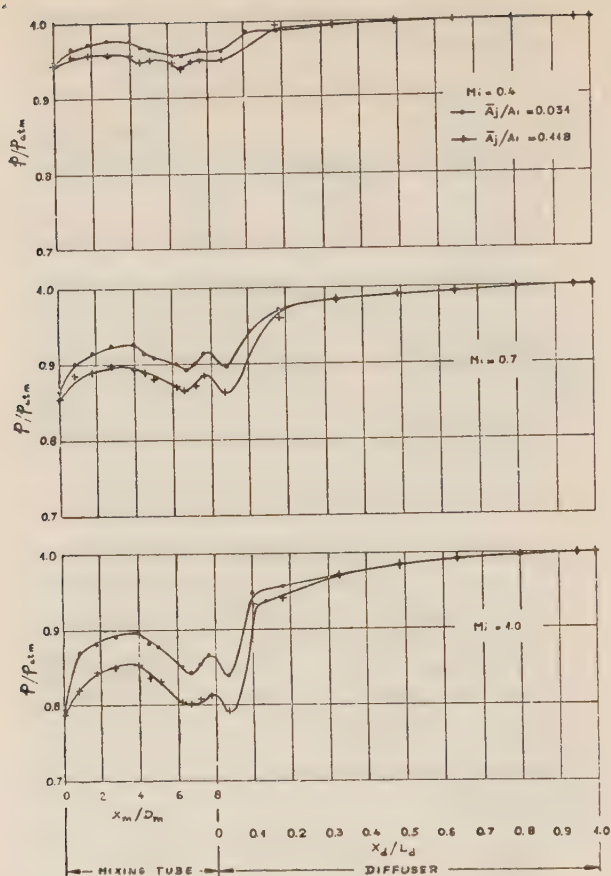


Figure 16C

Static pressure distribution along mixing tube No. 3 and 8° diffuser of area expansion ratio 8.

TABLE V

Injector performance with 4° and 8° diffusers compared with Ref. 2. Mixing tube length-to-diameter ratios 6, Mach number in test section 1.0.

$\bar{A}_j/A_i$	$P_{oj}$ psia Ref. 2	$P_{oj}$ psia 4° diffuser	$P_{oj}$ psia 8° diffuser	$\frac{P_{oj}}{(P_{oj})_{\text{Ref. 2}}}$	$\frac{P_{oj}}{(P_{oj})_{\text{Ref. 2}}}$ 4° diffuser	$\frac{P_{oj}}{(P_{oj})_{\text{Ref. 2}}}$ 8° diffuser
0.02	100	160	195	1	1.60	1.95
0.07	40	57	61	1	1.43	1.60
0.12	35	42	46	1	1.20	1.34

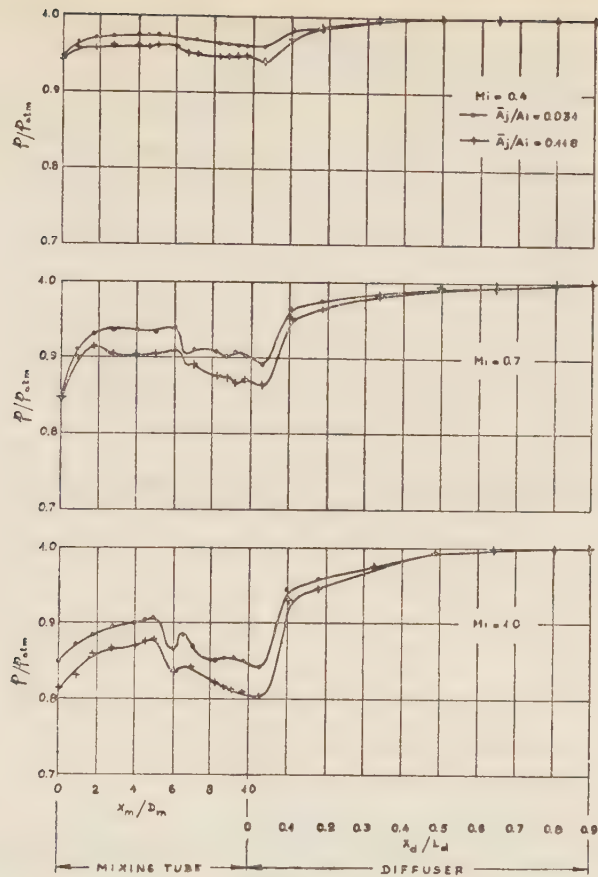


Figure 16D

Static pressure distribution along mixing tube No. 4 and 8° diffuser of area expansion ratio 8.

NOTATION

- |                                      |                                       |
|--------------------------------------|---------------------------------------|
| $A$ — cross-sectional area           | $R$ — gas constant                    |
| $D$ — diameter                       | $s$ — injection slot width            |
| $k$ — discharge coefficient          | $s^o$ — initial injection slot width  |
| $L$ — total length                   | $T$ — absolute temperature            |
| $m$ — rate of mass flow              | $x$ — length                          |
| $M$ — Mach number                    | $\gamma$ — specific heat ratio        |
| $n$ — number of half-turns of part E | $\delta_1$ — absolute error (Table 1) |
| $p$ — pressure                       | $\theta$ — angle                      |

Subscripts

- |                                      |                                 |
|--------------------------------------|---------------------------------|
| $a$ — injection area                 | $j$ — injection slot            |
| $d$ — diffuser, or diffuser inlet    | $m$ — mixing-tube               |
| $e$ — diffuser exit                  | $c$ — stagnation conditions     |
| $g$ — based on geometric calculation | $p$ — high pressure system      |
| $i$ — test section                   | $*$ — critical flow conditions. |

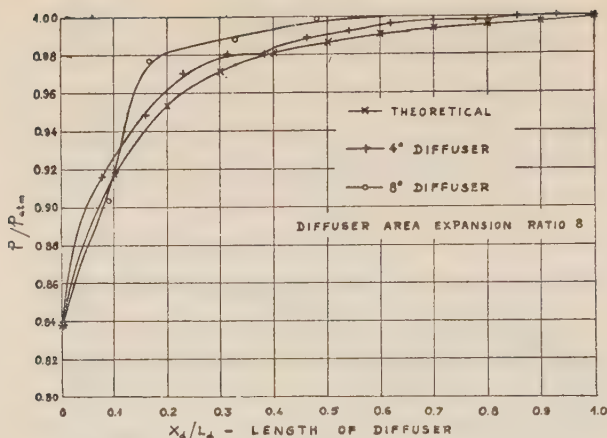


Figure 17

Static pressure distribution along diffusers compared with theoretical. Injector with Mixing tube No. 2 and  $A_j/A_i = 0.118$ .

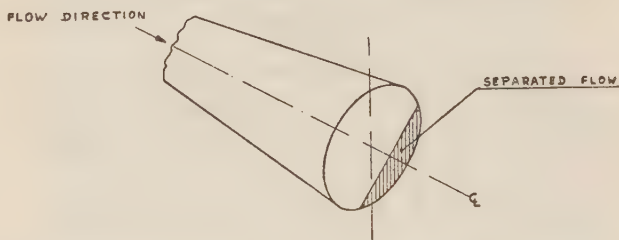


Figure 18

Zone of separated flow in the  $8^\circ$  diffuser as determined from stagnation pressure measurements at diffuser exit.

## REFERENCES

1. BEAVEN, J. A. AND HOLDER, D. W., 1950, Recent developments in High Speed Research in the Aerodynamics Division of the National Physical Laboratory, *J.R.Ae.S.*, **54**, 545-578.
2. HOLDER, D. W., 1954, The High-Speed Laboratory of the Aerodynamics Division, *N.P.L. A.R.C. Monograph*, R. & M. 2560.
3. KNOWLER, A. E. AND HOLDER, D. W., 1954, The Efficiency of High-Speed Wind Tunnels of the Induction type, *A.R.C. Monograph*, R. & M. 2448.
4. HOLDER, D. W. and NORTH, R. J., 1953, The  $9 \times 3$  in. Induced Flow High-speed Wind Tunnel at the National Physical Laboratory, *A.R.C. 12387*, R. & M. 2781.
5. REID, E. G., 1949, Annular Jet Ejectors, *NACA TN* 1949.
6. LAIDLAW, W. R., 1950, Ejector Theory and Its Application to Induction Type Wind Tunnels, *National Research Council of Canada, Rep. MA-232*.
7. LINDSEY, W. F., 1952, Choking of a Subsonic Induction Tunnel by the Flow from an Induction Nozzle, *NACA TN* 2730.
8. LINDSEY, W. F. AND CHEW, W. L., 1950, The Development and Performance of Two Small Tunnels Capable of Intermittent operation at Mach Numbers between 0.4 and 4.0, *NACA TN* 2189.
9. NELSON, W. J. AND BLOETSCHER, F., 1949, Preliminary Investigation of a Variable Mach Number Two-Dimensional Supersonic Tunnel of Fixed Geometry, *NACA RM L9D29a*.
10. BURGESS, Jr. W. C. AND SEASHORE, F. L., 1951, Criteria for Condensation-free Flow in Supersonic Tunnels, *NACA TN* 2518.
11. LUKASIEWICZ, J., 1947, Humidity Effects in Supersonic Flow of Air, *A.R.C.* 10977.



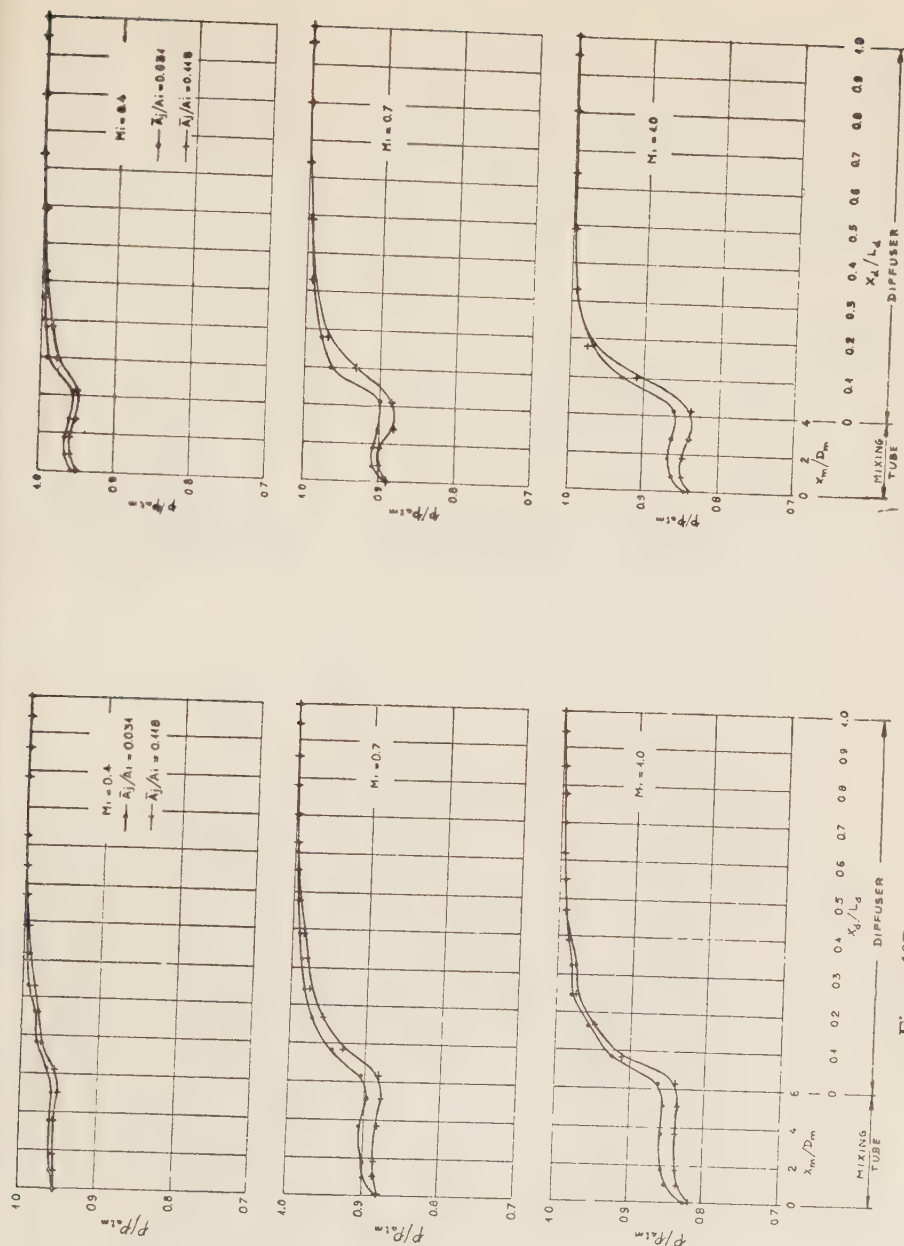


Figure 19A  
Static pressure distribution along mixing tube No. 1  
and 4° diffuser of area expansion ratio 8.

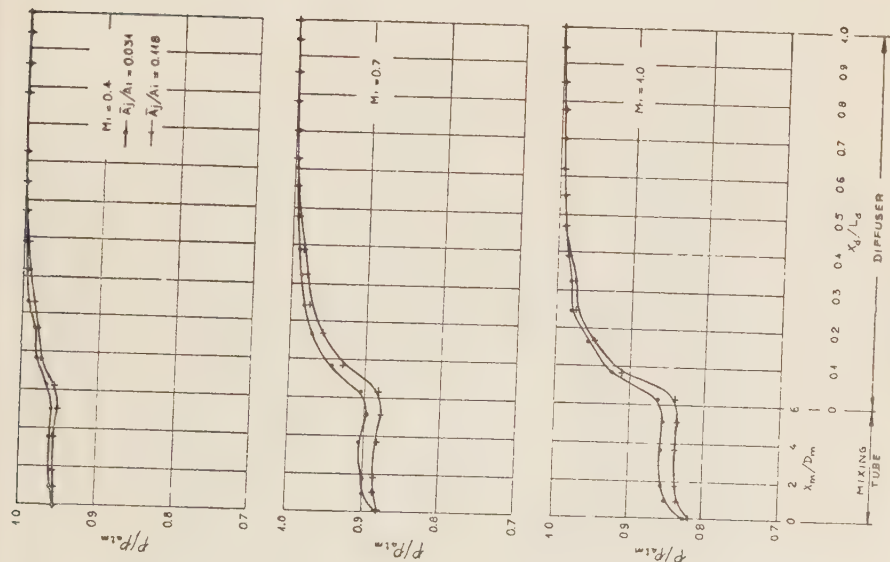


Figure 19B  
Static pressure distribution along mixing tube No. 2'  
and 4° diffuser of area expansion ratio 8.

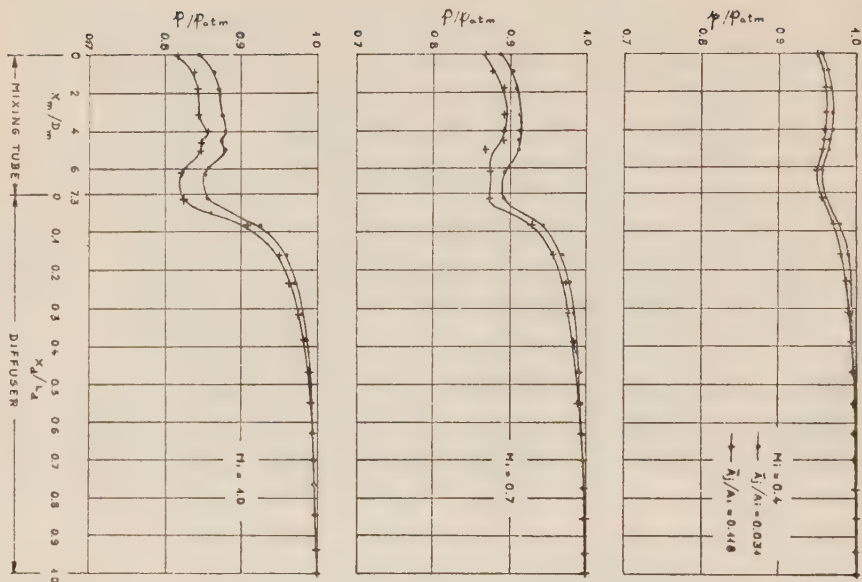


Figure 19C  
Static pressure distribution along mixing tube No. 3' and 4°  
diffuser of area expansion ratio 8.

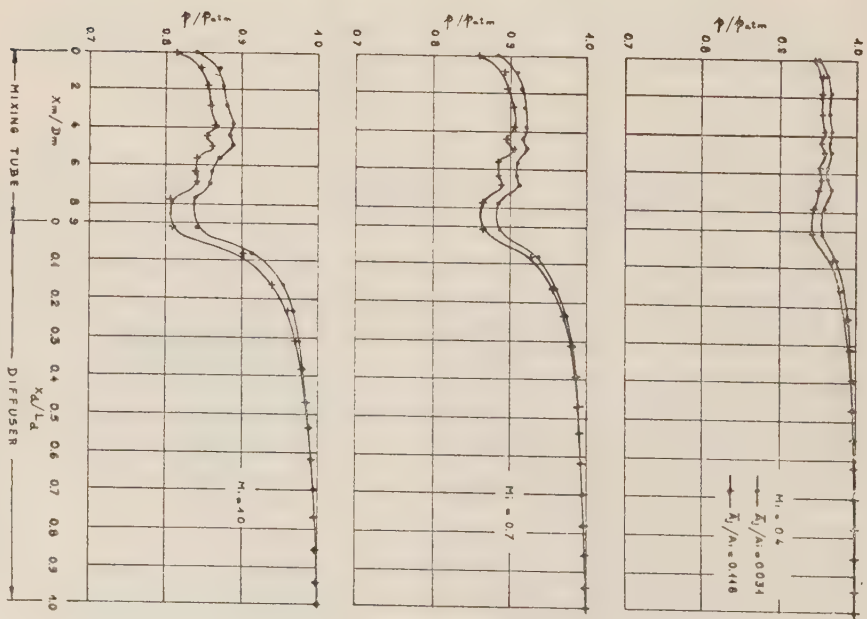


Figure 19D  
Static pressure distribution along mixing tube No. 4' and 4°  
diffuser expansion ratio 8.

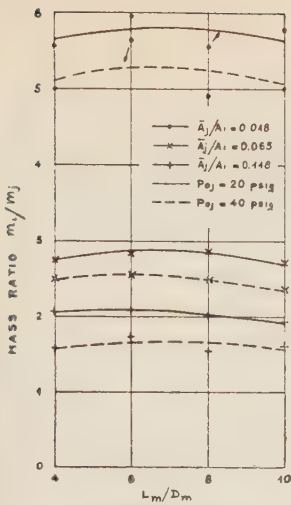


Figure 20

Mass ratio as function of mixing tube length and injection slot area. Injector without diffuser.

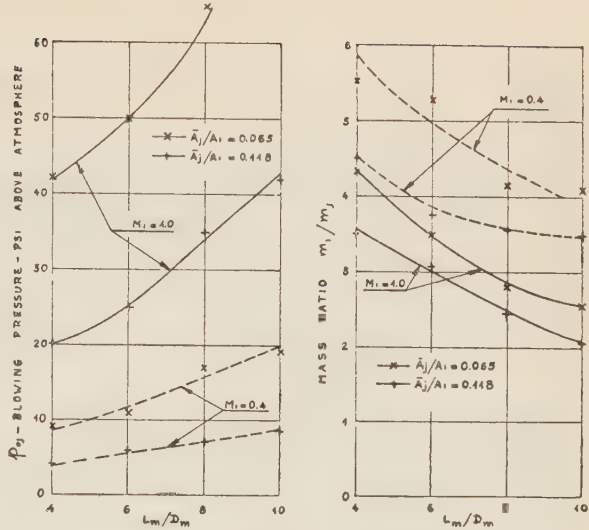


Figure 21

Blowing pressure and mass ratio as functions of mixing tube length. Injector with 8° diffuser of area expansion ratio 8.

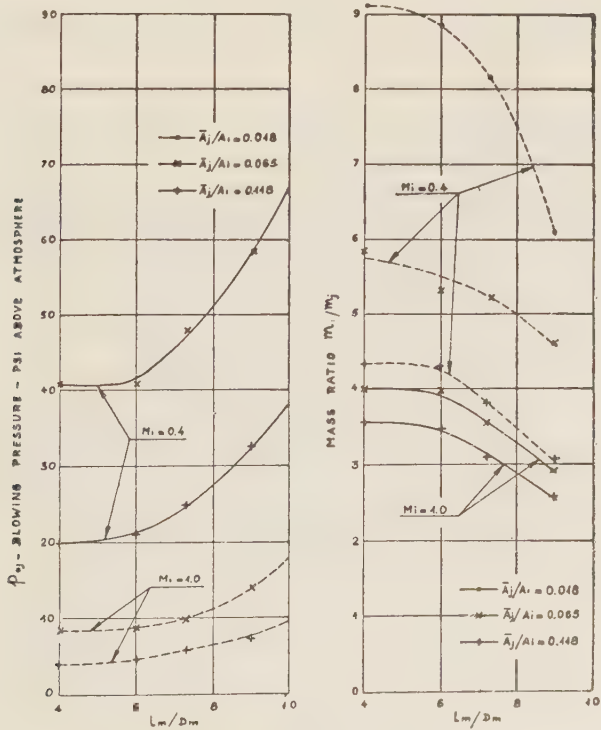


Figure 22

Blowing pressure and mass ratio as functions of mixing tube length. Injector with 4° diffuser of area expansion ratio 8.

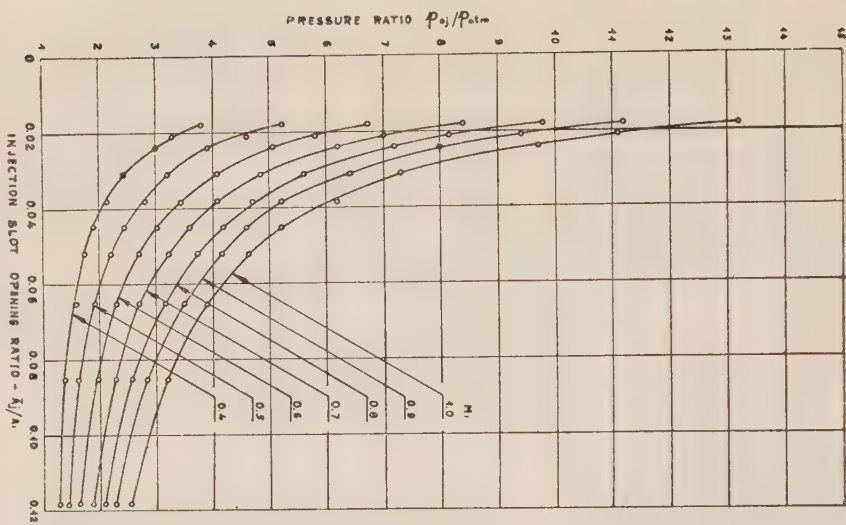


Figure 23

Blowing pressure as function of slot area and test section Mach number. Injector with  $4^\circ$  diffuser of area expansion ratio 8 and mixing tube of length-to-diameter ratio 6.0.

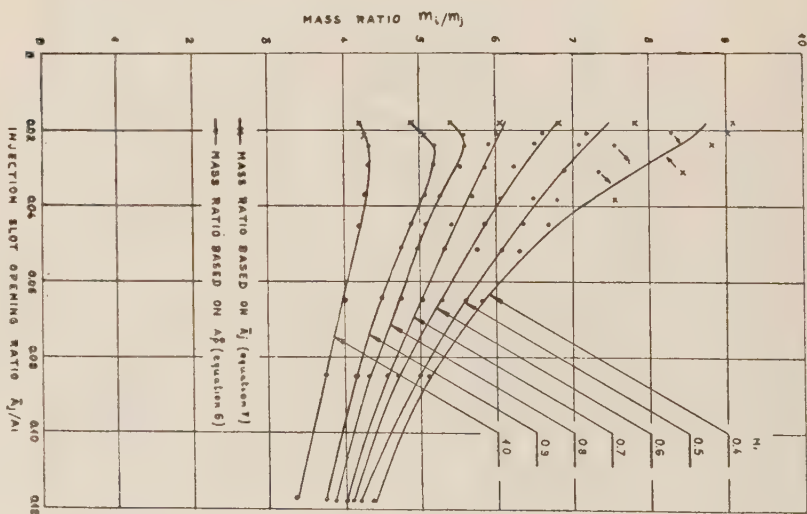


Figure 24

Mass ratio as function of slot area and test section Mach number. Injector with  $4^\circ$  diffuser of area expansion ratio 8 and mixing tube of length-to-diameter ratio 6.



# AERODYNAMIC RESEARCH FACILITIES AT THE DEPARTMENT OF AERONAUTICAL ENGINEERING, TECHNION-ISRAEL INSTITUTE OF TECHNOLOGY

JOSEF ROM (RABINOWICZ)

*Technion Israel Institute of Technology, Haifa*

## ABSTRACT

The research facilities developed by the staff of the Aeronautical Engineering Department, Technion-Israel Institute of Technology, are described. The aerodynamic facilities include the  $60 \times 90$  cm closed return subsonic tunnel, and the  $60 \times 60$  cm open circuit low speed tunnel. Two blow down supersonic tunnels  $10 \times 10$  cm and  $30 \times 30$  cm fed by a high pressure air supply of a 1000 ft. at 200 atm. An induction transonic tunnel model  $7 \times 9$  cm and a 7 meters long  $7.5 \times 7.5$  cm shock tube. The report describes briefly these facilities and their associated instrumentation.

## I. INTRODUCTION

Experimental aerodynamic research is based on the various facilities for simulating the flow conditions, as well as instrumentation for the measurement and recording of the experimental results.

The aerodynamic laboratory at the Technion was established in 1955. The construction of the high pressure air supply was completed in 1957 and the  $10 \times 10$  cm supersonic tunnel was completed in the beginning of 1958. The  $60 \times 90$  cm closed return subsonic tunnel was completed at the end of 1958. During 1959 – 1960 the open circuit low speed tunnel was added. Design and construction of the  $30 \times 30$  cm blow down supersonic tunnel was undertaken. A transonic tunnel model driven by an air injector was designed and built, and a shock tube of  $7.5 \times 7.5$  cm square section 7 meters long is under construction and will be completed early in 1961.

Concurrently, design and development of various instrumentation systems was undertaken. A number of manometers, multimanometers and bi-fluid micromanometers were installed. A three component side balance for the subsonic tunnel was designed and built. Under development now are various sting balances for all aerodynamic force and moment components. The recording system include, strain gauge bridges, pen-recorders and oscillographs, as well as, optical schlieren system for the supersonic tunnels.

The present report comes to summarize the development and to describe briefly these facilities which are used in the research and teaching activities of the Aeronautical-Engineering Department.



REMARK: DIMENSIONS IN PARANTHESES DESCRIBE DEPTH OF SECTION

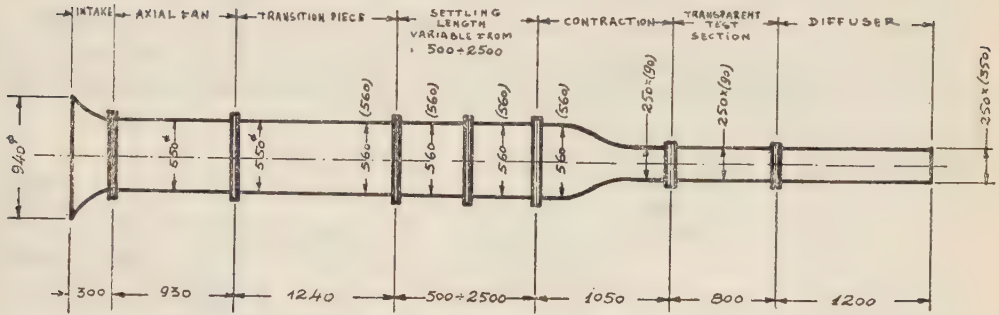


FIG 2. 25cm x 9cm SUBSONIC WIND TUNNEL

All tunnel cross sections are rectangular in shape except the round propellor section. Appropriate transition section from rectangular to round are provided both fore and aft of this section.

The tunnel top speed is 50 m/sec (110 mph) and the turbulence level is below 1%. Velocity distribution are uniform over the test section area within 1/2%.

### B. Open circuit 60 × 60 cm tunnel

A simple open circuit tunnel has been constructed using a ventilation blower powered by a 7.5 HP. d.c. motor which is controlled by a motor generator set. The blower is fitted with a central cone and the flow is directed through a transition section to a square channel of 60 × 60 cm cross section. This channel is constructed of 50 cm long sections. The overall length can be adjusted according to the testing demands. Various interchangeable contraction sections have been built. These are then connected to the end of the square channel so that a number of test sections of various cross sectional area and air velocity can be used. A short diffuser is also added to the test sections in order to increase the tunnel's efficiency and air spread. Figure 2 shows a typical arrangement of this tunnel. The versatility of this tunnel makes it particularly suitable for student experiments and other programs.

### III. TRANSONIC AND SUPERSONIC FACILITIES

#### A. High pressure air system

An air storage of 1000 cu.ft. at 200 atm. is used as a prime-mover for a number of blowdown high speed wind tunnels, and other facilities.

Three Worthington 4 stage reciprocating compressors each one powered by a 100 H.P. a.c. electrical motor are used in parallel to charge up the high pressure containers. The compressed air is cooled and the oil and moisture are separated by a flow reversal stage and then by a circumferential vortex separator. The cooled and

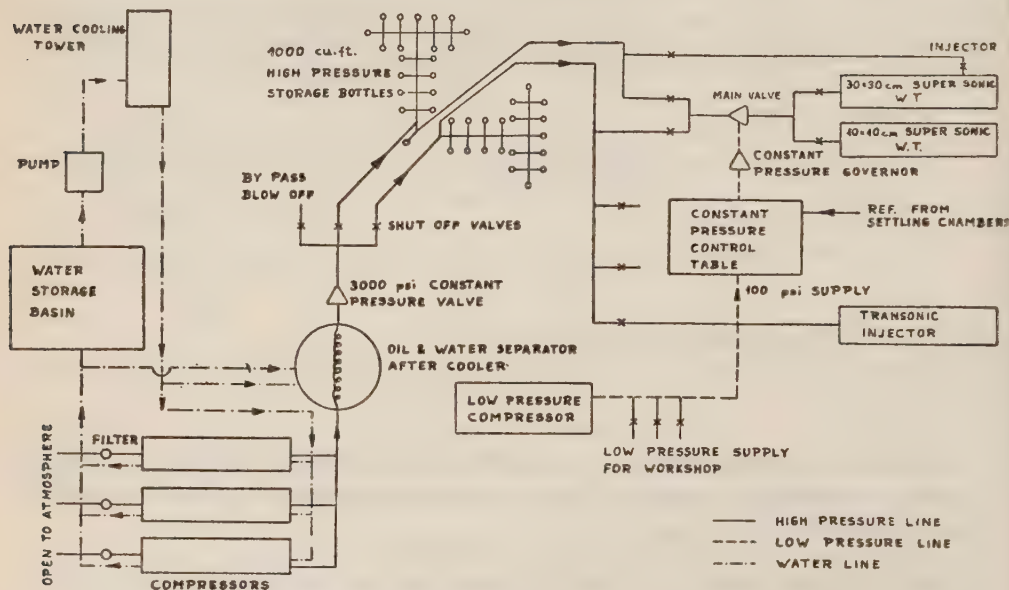


FIG. 3 HIGH AND LOW PRESSURE AIR SYSTEMS

dried air is then piped into the steel storage bottles. Two 2 1/4" high pressure pipes bring the air to a 3" pneumatically controlled "Conoflow" valve. The outlet of the control valve can be directed by various valves to the blow-down facilities. Safety diaphragms are fitted in the circuit to ensure relief in case of a blockage at some point in the low pressure side of the system. A diagram of the system is shown in Figure 3.

#### B. Supersonic blow down wind tunnels

A 10 × 10 cm blow down supersonic wind tunnel is in operation. This tunnel has the following structural sections:- (a) settling chamber, (b) nozzle and test section (c) diffuser (d) exhaust pipe. The settling chamber is a cylindrical tank 18" in diameter and 40" long. The air is admitted through a 90° angle directed backwards so that good mixing is enhanced. The forward flange is provided with an entrance cone



REMARK - SECTIONS ARE DESCRIBED BY INNER DIMENSIONS

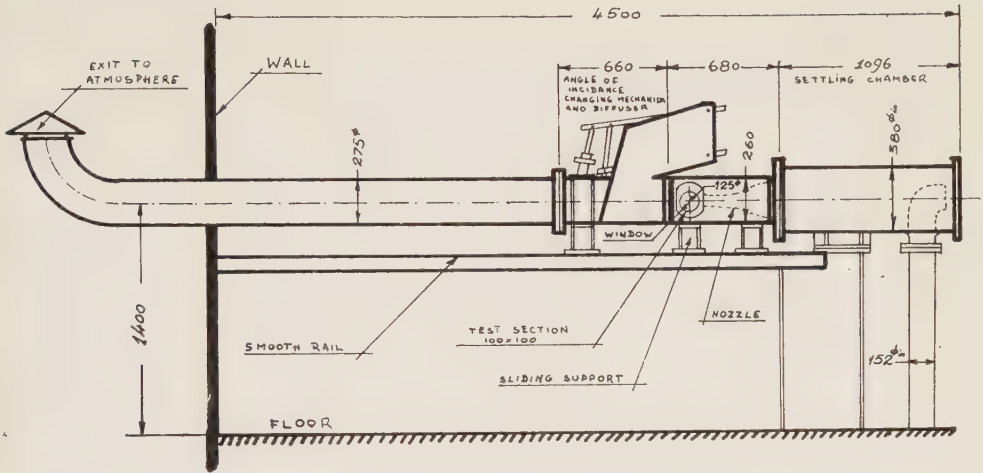


FIG 4a 1000 x 1000 SUPERSONIC WIND TUNNEL

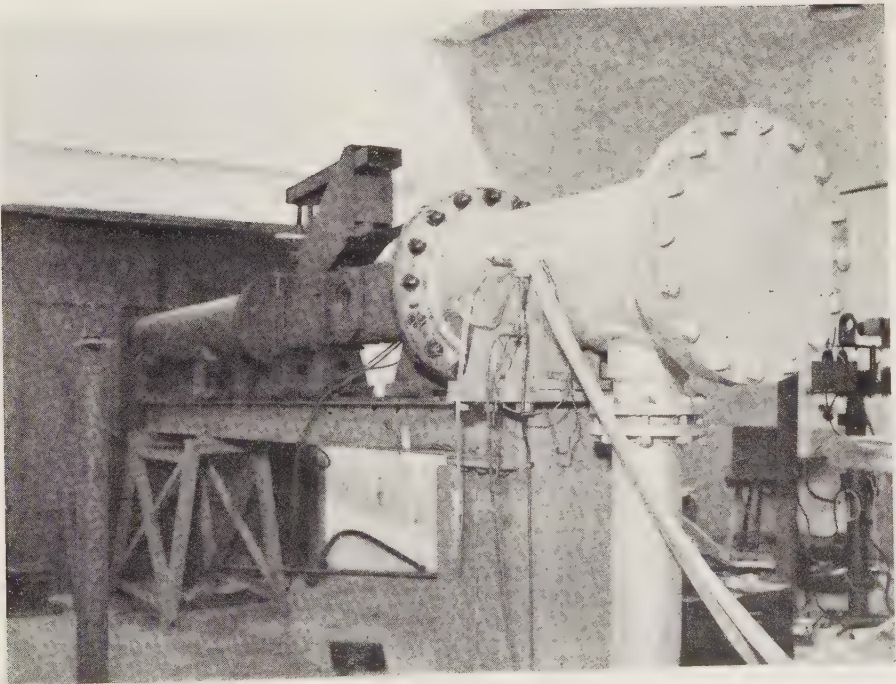


Figure 4b  
The 10 × 10 cm Supersonic Blowdown Wind Tunnel

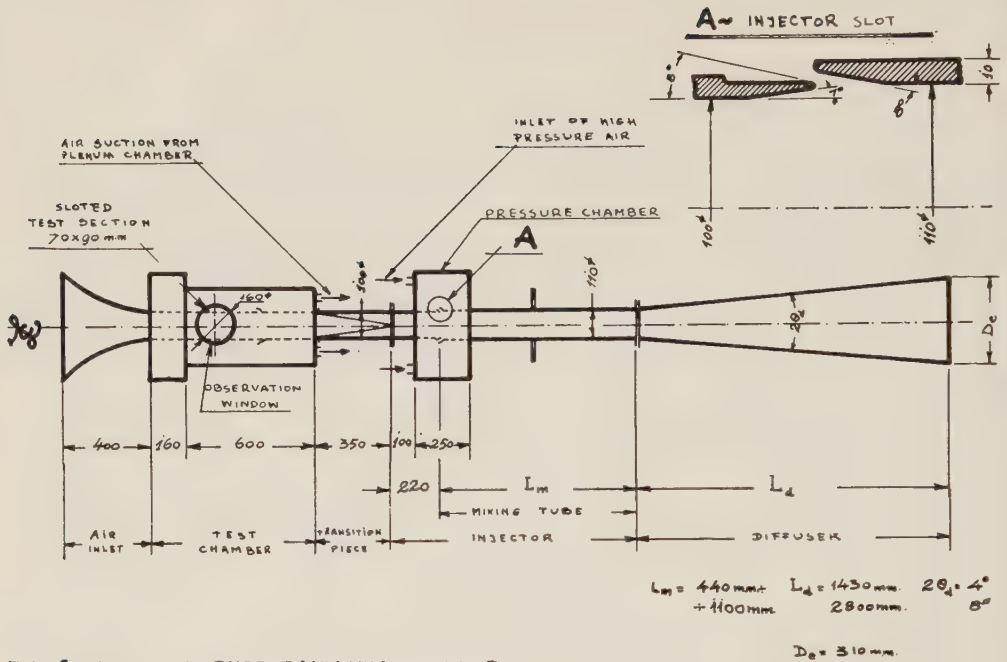


FIG 5 INDUCTION-TYPE TRANSONIC WIND TUNNEL

which has a transition to a rectangular section of  $4'' \times 7''$ . The nozzle section is a rectangular box  $4''$  wide  $7''$  high and  $26''$  long, in which the nozzle blocks are attached to the top and bottom walls and so provide a test section of  $10 \times 10$  cm. The boundary layer correction is obtained by increasing the test section size in the vertical plane only. A  $6''$  window is opened to the test section for optical observations. Nozzle blocks for Mach Numbers of 1.5; 2.25 and 3.5 are available. The diffuser is housed in a similar box. Wooden liners are used for defining the diffuser sections. This diffuser has a fixed second throat with an opening slightly larger than the best theoretical area. A model holder with adjustable angle of attack range is incorporated in the diffuser section. This mechanism is based on the parallelogram method in which the model holding bar follows the distortions of an external parallelogram about an axis which is centered in the test section.

From the diffuser section the air is led through a  $12''$  exhaust pipe to the atmosphere. An overall view of the tunnel is shown in Figure 4.

A second branch of the air supply is directed to the  $30 \times 10$  cm tunnel. It is similar in overall layout to the loxiocm one with all linear dimensions multiplied by approximately 3.

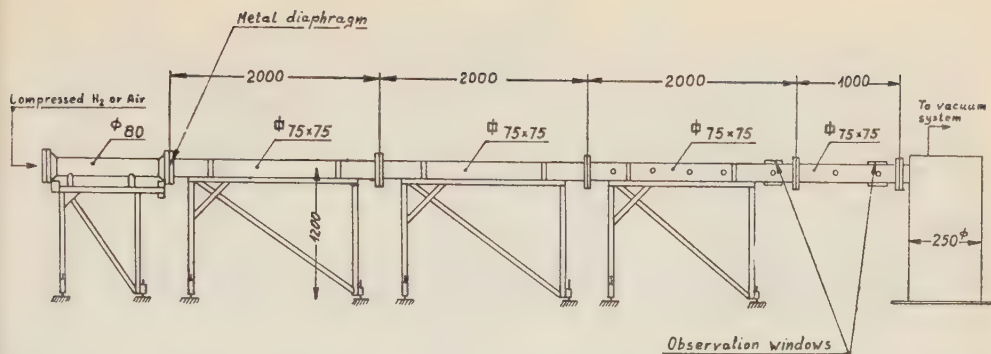


Fig. No. 6 SHOCK TUBE

### C. The $7 \times 9$ induction transonic wind tunnel model

A small induction tunnel which is used as a model for a transonic facility is now under development. An air injector supplied by the laboratory high pressure air supply is used for inducing a large mass of air through a  $7 \times 9$  cm test section. The tunnel is designed for operation at Mach numbers between 0.7 to 1.4.

The tunnel has a slotted wall test section, a circumferential injector followed by a length of mixing tube and a conical diffuser. The tunnel is shown in Figure 5 and is described in Ref. 2.

### D. Shock-tube

A shock tube is now under construction in the laboratory. The shock tube is driven by either compressed air or hydrogen at pressures up to 3000 psi. The compression chamber is a thick walled 3" steel pipe 1.5 m long. A metal diaphragm separates the high pressure from the low pressure sections. A square section  $7.5 \times 7.5$  cm and 7 m long can be evacuated to less than 1 mm Hg abs. The low pressure section is divided into a number of sections of which the two sections comprising the last 3m, are provided with instrumentation ports and observation windows. The low pressure chamber ends in a dump tank. High capacity vacuum pump is connected to the dump tank. A diagram of the tube is shown in Figure 6. A description of the shock tube and its instrumentation is given in Ref. 3. The 1 m section at the end of the low pressure chamber can be replaced by a hypersonic nozzle. This facility will be used for research in high energy, high Mach number flows.





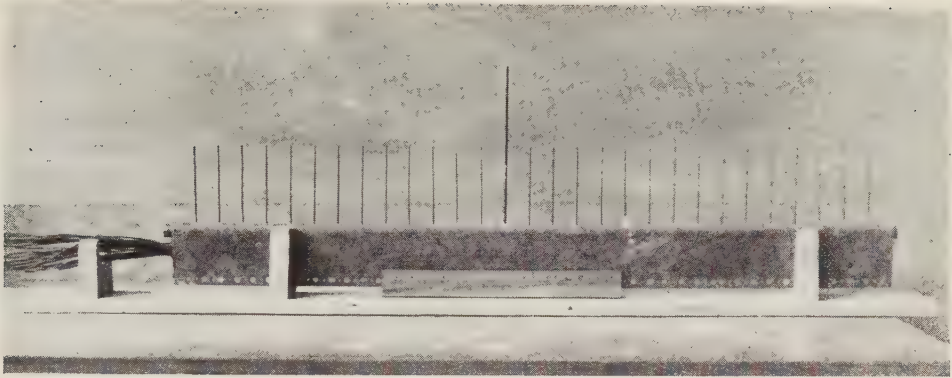


Figure 8a  
Pressure Rake for the  $60 \times 90$  cm Subsonic Wind Tunnel

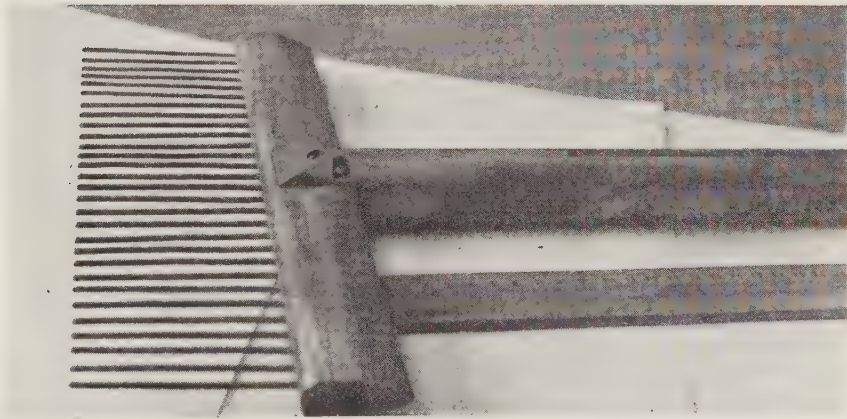


Figure 8b  
Total Pressure Rake for the  $60 \times 90$  cm Subsonic Wind Tunnel

The short running times in the blowdown supersonic tunnels and the recording of transient pressures is obtained by the use of strain gauges pressure transducers. A number of Statham unbonded strain gauge transducers for pressure ranges between 0.5 to 500 psi are available. The transducer output is recorded on a pen recorder or an oscillograph. Output can be also displayed on an oscilloscope when required.

Temperatures are obtained by various thermocouple combinations Cu-Constantan or Iron constantan and output is recorded on a self balanced potentiometer or an oscillograph.

### B. *Force and moments measurements*

The restriction of the model sizes for the various facilities require small force balances. Development of side balances and sting balances was undertaken. A three component side balance using strain gauge instrumented flextures is used in the  $60 \times 90$  cm subsonic wind tunnel. This balance can also be adapted to the supersonic wind tunnel. The balance is shown in Figure 9.

The internal sting balances have bakelite strain gauges which are bonded to the balance structure and respond to all components except drag. The drag element is measured by the deformation of a flexture arrangement which is sensed by an unbounded strain gauge. These balances are described in Ref. 4 and are shown in Figure 10a and 10b.

The strain gauge balance output is recorded on a pen recorder, an oscillograph or an oscilloscope.

The sting balances are calibrated on a special test stand (Figure 11). All six force and moment components can be loaded simultaneously in order to evaluate all interactions.

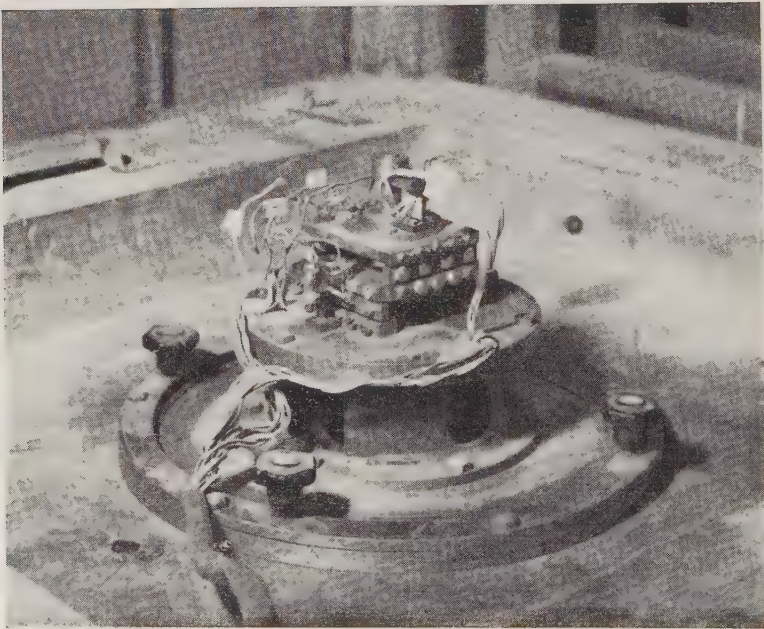


Figure 9  
Three Component Side Balance

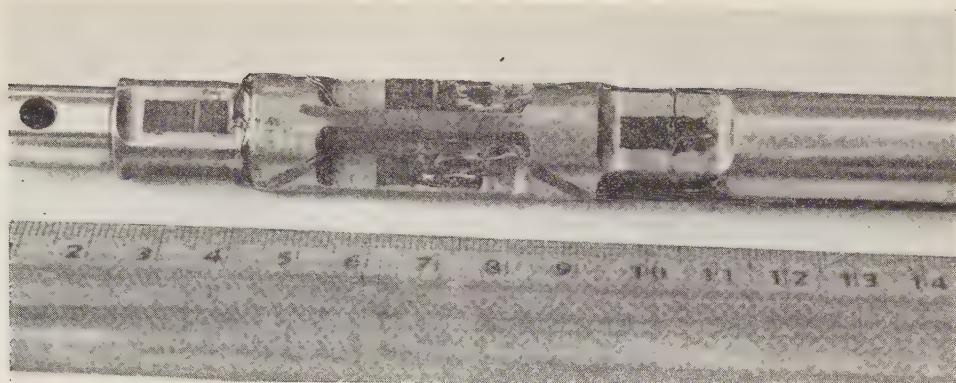


Figure 10a. Five Component Roll Balance

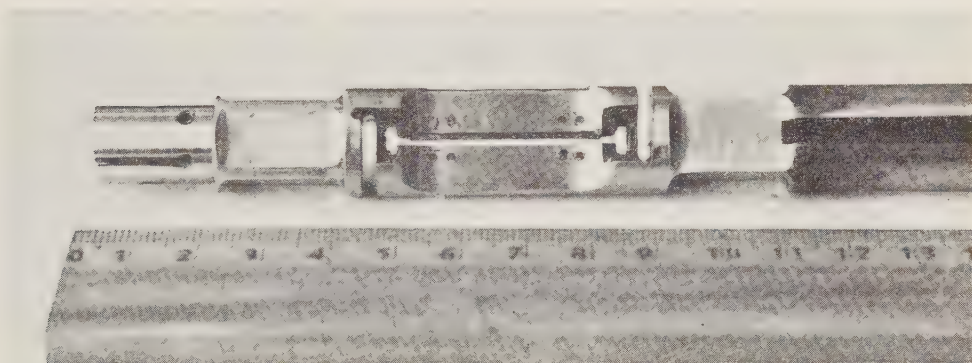
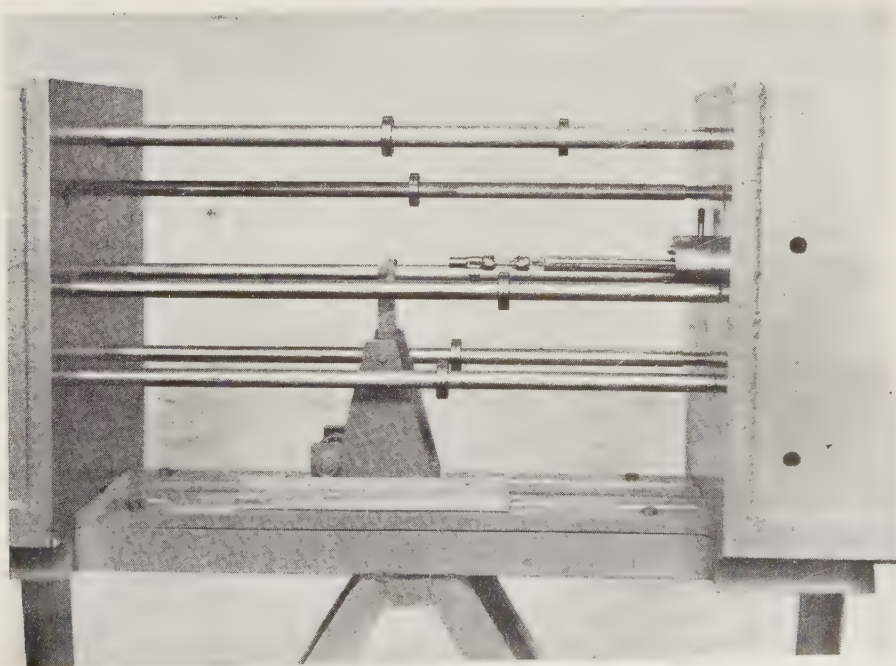


Figure 10b. Five Component Drag Balance





## REFERENCES

1. POPE, A., 1954, *Wind Tunnel Testing*, J. Wiley & Co., New York, 2nd ed.
2. KOGAN, A. AND VICTOR, M., 1961, The performance of an annular ejector—Third Annual Conference on Aviation and Astronautics, *Bull. Res. Council of Israel*, **9C**, 79.
3. RABINOWICZ, J., 1957, Aerodynamic Studies in a Shock Tube — GALCIT Hyperson Memorandum 38, June 1957.
4. KOGAN, A., SAGINER, A. AND SCHWARTZ, Y., A Supersonic Wind Tunnel Balance, to be published.



# AN APPROXIMATE METHOD OF SOLID PROPELLANT INTERNAL STAR GRAIN CALCULATION

A. YARON AND R. CORETT

*Scientific Department, Ministry of Defense*

## ABSTRACT

The usual internal burning grain configurations are calculated with the sole consideration of the burning perimeter variation. The proposed method concerns itself mainly with the overall dimensions of a grain and permits the general outlay of an internal star as well as the main proportions of the charge. The method of calculation takes into consideration the total mass of the charge, the ballistic properties of the propellant and permits calculation of the approximate shape of the internal star, which may then be modified by the usual methods according to required variations of the burning perimeter. The proposed method provides an easy means of charge calculation giving a possibility of quick appreciation of the motor proportions.

## ON EXTRAGALACTIC COSMIC RAYS

H. KASHA

*Department of Physics, Technion-Israel Institute of Technology, Haifa*

### ABSTRACT

It has been established by experiments <sup>1,2</sup> on the extensive air showers of cosmic radiation that there is no evident change in the character of the energy spectrum of primary cosmic rays in the energy range  $E > 10^{16}$  ev, and that particles of at least  $10^{19}$  ev are present in the primary cosmic-ray flux <sup>1,3</sup>. These facts impose stringent conditions on the theories of origin of cosmic rays, which in general assume that the particles are stored and mixed (or even accelerated) by the galactic magnetic clouds. The efficiency of this process is impaired at  $\sim 10^{17}$  ev, which should lead to a deficiency and a pronounced anisotropy of the high-energy tail of the radiation. The absence of such phenomena is difficult to reconcile with a purely galactic theory of origin of cosmic rays. In his "supernova" theory, Ginzburg<sup>4</sup> completely neglects any extragalactic contribution. This may be inconsistent with this very successful theory itself; many galaxies, in addition to our own, possess cosmic-ray sources (supernovae) and some special extragalactic objects like the spherical galaxy M87 are sources of bremsstrahlung radiation (and thus presumably cosmic rays) on an incomparably larger scale than the galactic supernovae<sup>5,6</sup>. The contribution of extragalactic cosmic-ray sources depends greatly on the "transmission coefficient" of the galactic boundary<sup>7</sup>. The value of this coefficient can be, at present, only guessed at; however, the experimental facts on air showers at very high energies seem to contradict clearly some estimates, in particular that of Ginzburg, who put it at  $\sim 1\%$ . The transmission coefficient is certainly energy-dependent (increasing with increasing energy), and thus it is not very convincing to exclude the possibility of an extragalactic origin of at least a part of the cosmic-ray particles initiating the greatest extensive air showers.

### REFERENCES

1. CLARK, EARL, KRAUSHAAR, LINSLEY, ROSSI AND SHERB, 1957, *Nature*, **180**, 353, 406.
2. ALLAN, BEAMISH, BRYANT, KASHA AND WILLS, 1960, *Proc. Phys. Soc.*, **76**, 1.
3. ZATSEPIN, G. T., 1960, *Proc. Moscow Cosmic Ray Conf.*, vol. II.
4. GINZBURG, V. L., 1958, *Progress in Cosmic Ray Physics*, **4**, 337.
5. BAADÉ, W., 1956, *Astrophys. J.*, **123**, 550.
6. SHKLOVSKII, I. S., 1955, *Astron. J. Soviet Union*, **32**, 215.
7. SITTE, K., 1956, *Bull. Res. Council of Israel*, **6A**, 61.

## STRAIN GAUGE BALANCE FOR WIND TUNNELS

A. KOGAN, J. SCHWARTZ AND A. SEGNER

*Department of Aeronautical Engineering, Technion Israel Institute of Technology, Haifa*

### ABSTRACT

Two electrical resistance strain gauge balances were developed for wind tunnel model testing: one—for the measurement of lift, side force, pitching moment, yawing moment and rolling moment, and the other—for the measurement of lift, drag, side force, pitching moment and yawing moment.

An effort has been made to reduce the interactions between the different force and moment components to a minimum.

A special unit has been developed for the drag measurement. It consists of a system of unbonded strain gauges.







יוצא לאור ע"י

**מוסד ויצמן לפרסומים במדעי הטבע ובטכנולוגיה בישראל**

המועצה המדעית לישראל - משרד החינוך והתרבות - האוניברסיטה העברית בירושלים  
הטכניון — מכון טכנולוגי לישראל - מכון ויצמן למדע - מוסד ביאליק

Published by

**THE WEIZMANN SCIENCE PRESS OF ISRAEL**

Research Council of Israel, Ministry of Education and Culture

The Hebrew University of Jerusalem, Technion-Israel Institute of Technology

The Weizmann Institute of Science, Bialik Institute

Printed in Israel

**JERUSALEM ACADEMIC PRESS LTD.**

SET ON MONOTYPE